Interactions and Confinement of Particles in Liquid Crystals: Novel Particles and Defects

Anne Helen Macaskill

Submitted in accordance with the requirements for the degree of
Doctor of Philosophy

The University of Leeds
School of Physics and Astronomy

July 2019

Declaration

The candidate confirms that the work submitted is her own and that appropriate credit has been given where reference has been made to the work of others.

This copy has been supplied on the understanding that it is copyright material and that no quotation from the thesis may be published without proper acknowledgement.

©2019 The University of Leeds and Anne Helen Macaskill

Acknowledgements

UOM: University of Manchester

UOL: University of Leeds

SMP: Soft Matter Physics

LC: Liquid Crystals

The original research proposal and funding for this project were secured by J. Cliff Jones (then UOM, currently UOL) and Ingo Dierking (UOM). At this time both were members of the Soft Matter Research Group, University of Manchester. Both Jones and Dierking oversaw, supervised and oversaw many details of this project, especially early on, during chapter 3. Later chapters of the project, from chapter 4 onwards, were primarily supervised by Helen F. Gleeson (originally UOM, now UOL), with exceptions given below.

In Chapter 3, the synthetic particles were produced by Sean Butterworth of the Organic Materials Innovation Centre, School of Chemistry, UOM. Other members of the research group also gave advice on, for example, choosing a solvent for the particles (notably Steve Yeates and Joshua Moore). The group also allowed the use of their labs and equipment.

From chapter 4 onwards, the focus of the project began to move to the interaction of particles with defects and particle tracking (a suggestion originally made by Gleeson). Much advice (on practical use of equipment and data analysis) was given by David Wei, UOM. Wei also personally supervised the first experiments on particle tracking on the Leica laser tweezing system in chapter 6, which was based in the Photon Science Institute, UOM. We also credit M. Dickinson for granting access to labs and equipment. The Nikon tweezing system was based in labs of the Molecular and Nanoscale Physics group, UOL, although the equipment is half-owned by the SMP group. Some assistance on setting up the tweezing system (for

example, aligning the laser and attaching the colour camera) was given by Ben Johnson (MNP group). On the method of treating particles with DMOAP I was advised by M Nikkhou, who recently joined the SMP group, UOL.

The micrometre scale Janus particles in chapter 7 were manufactured by Andrew Leeson of the School of Chemical and Process Engineering, UOL. Discussions with Leeson and Olivier Cayre helped to inform the further work section on Janus particles.

In the further work section we mention a project conducted at the CLF, Oxfordshire. All work was conducted under Jones and Mamatha Nagaraj (also SMP group, UOL), who performed the use of the high resolution microscopes and all data analysis.

Some of the further work section (chapter 8) was inspired by discussion with Gleeson, but also Shajeth Srigengan, who also provided me with the raw data for the elastic constants of compound 1 and compound 2.

Finally, I am indebted to all the members of the research groups (originally the LC group, School of Physics and Astronomy, UOM, later the SMP group, School of Physics and Astronomy, UOL). Many standard techniques of experimental liquid crystal physics were taught to me by other members of the group . For example, cell construction was originally taught to me by James Bailey. As is the nature of a research group, many members helped my project with day-to-day discussions, and general practical advice.

Abstract

The motivating topic for this project was to work towards building a new type of electronic paper. Current electronic paper technologies are not able to perform at frame rates high enough to display video. The project was inspired by a prototype device based on the ‘Janus particle’ (particles with two halves of different properties, for example, colour), and to try to reduce the power consumption.

The starting point for the project was an investigation of 500nm Janus particles and spheres. The question of whether the addition of particles affected physical properties of the bulk liquid crystal was investigated. Above concentrations up to 1% wt/wt, aggregations formed quickly. At this weight percentage, no significant changes in order parameter, refractive indices or elastic constants of the LC could be seen.

It is known qualitatively that topological defects in liquid crystals can attract or repel particles. Importantly the strength of interaction of particles with defects has been quantified in this work. A passive method of microrheology was implemented to quantify the confinement strength. Depending on the system, confinement strengths ranged between 10 and 10,000pN/μm. Particles treated for strong surface anchoring were found to be more strongly confined than particles with weak surface anchoring. Further, particles in liquid crystals with higher elastic constants were found to have higher confinement strengths than in particles in liquid crystals with lower elastic constants. Particle size was not found to affect confinement strength significantly in the size range studied.

Finally, the topic of Janus particles was readdressed. In the size regime ~5-10μm Janus particles show evidence of hybrid alignment and rotation in an electric field.

In conclusion, the idea of using Janus particles in a device appears promising: we hope this work is continued in future.

Table of Contents

Declaration ..... **i**
Acknowledgements ..... **ii**
Abstract ..... **iv**
Table of Contents ..... **v**
List of Tables ..... **x**
List of Figures ..... **xii**
List of Abbreviations ..... **xxiii**
List of Symbols ..... **xxvi**
Chapter 1 Display Devices and Electronic Paper **1**
1.1 Introduction 1
1.2 Electronic Paper 1
1.2.1 Approaches to Reduce Power Consumption 2
1.3 Liquid Crystal Displays 3
1.3.1 LCDs adapted for low-power applications 3
1.4 Electrophoretic Displays 5
1.4.1 Janus Particle-based device: The Gyricon 6
1.4.2 Other low-powered display types 8
1.5 Summary of Low-Powered Display Devices 8
1.6 Displays based on Liquid Crystal Colloids 10
1.7 Conclusion 10
Chapter 2 Introduction to Liquid Crystals, Colloids and Liquid Crystal Colloids **17**
2.1 Introduction 17
2.2 Optics of Birefringent Materials 17
2.2.1 Refractive Index 17
2.2.2 Birefringence 18
2.2.3 Wave Plates and Wave Plate Conditions 20
2.2.4 Full Wave Plate 21
2.2.5 Half Wave Plate 21
2.2.6 Quarter Wave Plate 23
2.2.7 Crossed Polarisers and Polarising Microscopy 23

2.2.8 Polarising Microscopy with Wave Plates 28
2.3 Liquid Crystals 32
2.3.1 Nematic Liquid Crystals 33
2.3.2 The Director 33
2.3.3 Order Parameter[5] 33
2.3.4 Viscosity 34
2.3.5 Elastic Constants 35
2.3.6 Anchoring Conditions[17] 36
2.3.7 Freedericks Transition 37
2.3.8 Liquid Crystal Displays 39
2.3.9 Defects in Liquid Crystals [23,24] 40
2.4 Colloids[24, 27] 42
2.4.1 Stokes' Law 42
2.4.2 Electrophoresis 42
2.4.3 Stability and Inter-Colloid Forces 43
2.4.4 The Electrical Double Layer and the Zeta Potential 43
2.4.5 Brownian motion 46
2.5 Liquid Crystal Colloids 47
2.5.1 Defects associated with Particles 47
2.5.2 Particle motion in an Electric Field 49
2.5.3 Translational Motion: Electrophoresis 50
2.5.4 Rotational motion: Quincke Rotation 51
2.6 Summary 51
Chapter 3 Experimental Methods 57
3.1 Introduction 57
3.2 Cell manufacture and construction 57
3.2.1 Cutting and cleaning of glass substrates 59
3.2.2 Surface treatment for alignment on substrates 59
3.2.3 Cell construction 60
3.2.4 Determination of cell gap 60
3.2.5 Cell filling and sealing 61
3.3 Polarising microscopy 61
3.4 Laser Trapping 61
3.4.1 Motivation 61

3.4.2 Introduction to optical trapping 62
3.4.3 Principles of optical trapping[6, 7] 62
3.4.4 Optical traps as a potential well[11] 69
3.4.5 Other methods of measuring forces on LC colloids 70
3.4.6 Other methods of colloid manipulation 70
3.4.7 Optical tweezing setup 72
3.5 Particle Tracking 76
3.5.1 Methods of particle tracking 76
3.5.2 Software specifications 77
3.6 Conclusion and Summary 78
References 79
Chapter 4 Effect of Submicron Spheres and Janus Particles on a Nematic Liquid Crystal 81
4.1 Introduction 81
4.2 Materials 82
4.2.1 Selection of Solvent 83
4.2.2 Dynamic Light Scattering[16,17] 84
4.2.3 DLS Versus Scanning Electron Microscopy[21] 86
4.2.4 Laser Doppler Velocimetry 88
4.2.5 Characterisation of Particles by Diameter and Zeta Potential 89
4.3 Methods 91
4.3.1 Making Solutions 91
4.3.2 Transition Temperatures 91
4.3.3 Dielectric Constants and Elastic Constants 92
4.3.4 Refractive Index and Order Parameter 92
4.4 Results 93
4.4.1 Choosing a Concentration of Particles 93
4.4.2 Transition Temperatures 93
4.4.3 Dielectric Constants and Elastic Constants 95
4.4.4 Refractive Indices and Order Parameter 98
4.5 Discussion and Conclusion 100
References 102

Chapter 5 Particle Tracking and Features of Particle Trajectories of Mean Square Displacement Data 105

5.1 Introduction 105

5.2 The Mean Square Displacement of Freely Diffusing and Confined Particles 105

5.3 Methods of Fitting: Linear vs. Exponential 110

5.4 Noise at Short Time Scales 112

5.5 Drop in MSD at long time scales [2,3] 113

5.6 Drift 114

5.7 Spatial Artefacts 120

5.8 Conclusion 120

References 122

Chapter 6 Quantifying the Strength of Confinement of Particles at Defects in Nematic Liquid Crystals 123

6.1 Introduction 123

6.2 Quantifying the Confinement Strength of Defects Trapping Particles with Weak and Strong Surface Anchoring 124

6.2.1 Weak Anchoring Case 125

6.2.2 Strongly Anchored Particles 139

6.2.3 Discussion 144

6.3 Confinement Strength and Liquid Crystal Type, Cell Gap and Particle Size 148

6.3.1 Experimental Methods 149

6.3.2 Effect of Liquid Crystal on Confinement Strength 149

6.3.3 Effect of Cell Gap on Confinement Strength 151

6.3.4 Effect of Particle Diameter 154

6.3.5 Discussion 156

6.3.6 Conclusion 161

Chapter 7 Surface Alignment around Janus Particles in Nematic Liquid Crystals 165

7.1 Introduction 165

7.2 ~500 nm Janus Particles 166

7.3 ~50 µm Janus Particles 168

7.4 ~5 µm Janus Particles 169

7.4.1 Alignment at Surface of Particles 171

7.4.2 Alignment on PMMA and PS Flat Sheets 176

7.4.3 Electric Field Behaviour 178
7.5 Discussion and Conclusion 179
Chapter 8 Conclusions and Further Work 183
8.1 Introduction 183
8.2 Particles in Unusual Nematic Phases above Room Temperature 185
8.2.1 Elastic Constants near Sm-A Transition in 8CB 187
8.2.2 Bent-Core Liquid Crystals 187
8.2.3 Particles in Lyotropic and Chromonic Phases[36, 37] 192
8.3 Particle Interaction with Defects 198
8.4 Particles 199
8.4.1 Nanoparticles 199
8.4.2 Other Particle Geometries at Micron Scale 204
8.4.3 Continuation of Janus Particles Work 204
8.5 Possible Device Applications 206
8.6 Summary 207

List of Tables

Table 1.1. Comparison of properties of some types of low-powered display device. *: can be modified to operate in reflective mode, but doing so reduces contrast further. Note on the Gyricon: contrast has not been measured, but is possible if particles are made from high contrast materials..... 9

Table 2.1. Three conditions under which on observing no transmission through crossed polarisers, even if the sample is birefringent and transparent. 24

Table 2.2 Full wave plate condition for $\Gamma = 1000\ \mathrm{nm}$. Wavelengths fulfilling this condition will not be transmitted through the analyser, in this case, green light at 500 nm. 27

Table 2.3 Half wave plate condition for $\Gamma = 1000\ \mathrm{nm}$. If the optic axis is at 45° to the polariser and analyser, the polarisation direction is rotated by 90°, therefore is transmitted through the analyser, at that specific wavelength. In this case, red and violet are transmitted..... 27

Table 2.4. The same argument used to calculate the birefringence colours for $\Gamma = 1000\ \mathrm{nm}$ can be used for $\Gamma = 2000\ \mathrm{nm}$, using the wave plate conditions to predict which colours will be passed by the analyser, in this case, green. Only orders in the visible part of the spectrum are included. 29

Table 2.5. The birefringence colours associated with a birefringent sample with $\Gamma = 2000\ \mathrm{nm}$, with a lambda plate as determined by the half wave plate condition. 30

Table 3.1. Types of glass used for substrates depend on the experiment conducted. 58

Table 4.1. Comparison of some properties of DLS and SEM when measuring the diameters of particles..... 88

Table 4.2. Particle sizes (*: after dispersal in hexane, evaporation of hexane and re-dispersal in water). 90

Table 4.3. Zeta potential measurements conducted in water. 90

Table 4.4 Transition temperatures as a function of particle concentration. 95

Table 5.1 Comparison of confinement strength calculated from the same raw data, by linear fitting and exponential fitting. 112

Table 5.2. Results of fitting data from Fig. 5.9 before normalisation, including standard error from fitting. 118

Table 6.1. Refractive indices of melamine resin particles and MLC-6648. The particles were 4 μm in diameter..... 127

Table 6.2. Confinement strengths for melamine resin particle confined at defects in MLC-6648, including ±½ and ±1 defects.. 134

Table 6.3. Viscosities calculated from the fitting performed on Fig. 6.12. According to chapter 5, equations 5.4, 5.11 and 5.22 respectively for the 2D and 3D cases. 137

Table 6.4. Confinement strength for DMOAP-treated particle with HH defect at ±1 defect in MLC-6648 144

Table 6.5. Summary of some characteristics of melamine resin and borosilicate particles that may affect their motion. 144

Table 6.6. Trap stiffness in two different liquid crystals, 5CB and MLC-6648 (5μm particles with homeotropic surface anchoring) 151

Table 6.7. Confinment strength as a function of cell gap. Particles are 5 μm in diameter with homeotropic surface anchoring. 154

Table 6.8. There are some suggestions of trap stiffness lowering with smaller particle size. 156

Table 6.9. Average viscosity of 5CB and MLC-6648 at 20°C. 157

Table 8.1. Ratios of elastic constants for compound 1 [32] and compound 2 [32] in the nematic range. 5CB is included for comparison [35]. 192

List of Figures

Fig. 1.1. Figurative representation of the operation of e-ink [16], one of the most commercially successful electrophoretic displays. Positively and negatively charged particles of pigment are suspended in a medium. Particles are neutrally buoyant, making the device bistable. Applying an electric field swaps the positions of the particles. Assuming this diagram is a vertical cross section, a view looking from above will see either white (left) or black (right). The pigment particles are contained in capsules which reduce the chance of particle flocculation over time, and also acts as the unit 'pixel' for the display. 5

Fig. 1.2. Simplified diagram representing the rotation of a Gyricon particle in an electric field, based on the diagram in Crowley, Sheridon and Romano [28]. In a real device, electro-rotation forces are opposed by a viscous drag force. 7

Fig. 2.1. a) A refractive index indicatrix for a 'positive' uniaxial material. b) Indicatrix used to find the vibration directions of the o-ray (Eo) and the e-ray (Ee), and the refractive indices experienced by them, no and ne' respectively, where $n0 \leq ne' \leq ne$. The o-ray always vibrates perpendicular to the optic axis. Eo and Ee are always perpendicular to each other. This diagram is based on section 6.3 of Saleh and Teich, which also includes the full derivation and a more mathematical description of how the indicatrix is used. 19

Fig. 2.2. A half-wave plate rotates the vibration direction of an incoming beam from $+\theta WP$ to $-\theta WP$, relative to the fast axis. 22

Fig. 2.3 Representation of light (dotted line) passing through a birefringent sample, with the oval representing a cross-section of the refractive index ellipsoid. Under certain conditions, only one refractive index is experienced by light passing through a birefringent material. In this case, the polarisation direction does not rotate when passing through the material, even if the material is birefringent. In case a), ne aligns with the polariser (and no aligns with the analyser), and only ne is experienced. In case b), no aligns with the polariser, ne aligns with the analyser, and only no is experienced. In case c), the optic axis is parallel to the propagation direction of the light, and only no is experienced. 25

Fig. 2.4. Figurative representation of a birefringent material (with ordinary refractive index ne, and extraordinary refractive index no. The optic axis of the material lies at an angle ϕOA to the vibration direction of the light leaving the polariser. Incident light is entering through the page, i.e. perpendicular to the optic axis of the material..... 26

Fig. 2.5. Representation of what would be seen under crossed polarisers without (a), b)) and with (c), d) and additional wave plate, with a sample containing a birefringent substance with different orientations (cross sections of refractive index ellipsoid). The birefringence colours observed with the additional wave plate can distinguish when the optic axis is at +45° or -45° to the analyser, which is not possible from a static image in polarising microscopy. 31

Fig. 2.6. A schematic of the same rod-like molecules forming crystalline, nematic liquid crystal (see section 2.3.1) and isotropic phases, with increasing temperature implied from left to right. In some materials there is more than one liquid crystalline 'mesophase' between the crystalline and isotropic phases..... 32

Fig. 2.7. Illustrations of the three Miesowicz viscosities (representing shear in different planes with respect to the director) $\eta 1$, $\eta 2$, and $\eta 3$, as well as rotational viscosity, γ. 35

Fig. 2.8. Deformations associated with Elastic constants in a liquid crystal for splay (a) twist (b) and bend (c). 36

Fig. 2.9. Diagram showing how the director n at a surface is defined with the azimuthal angle, ϕanc, and pretilt θanc. 37

Fig. 2.10. A simple, planar liquid crystal display. The arrows represent the polarising axes of the polarisers, which are at 90° to each other. The orientation of the liquid crystal molecules in the bulk of the cell changes if the voltage applied is strong enough to cause a Freedericks transition. As a note on the scale of this diagram, molecular size is typically ~4nm, a cell gap of ~5-10µm, and the glass substrates ~1mm thick. 39

Fig. 2.11. Classification of defect types by winding number (the 'line' would extend into and out of the page). Winding number is calculated by drawing a loop around the defect core, and counting the number of times the director rotates (going counter-clockwise). Only half integer or integer values of winding number are allowed. Based on a diagram from [24]..... 41

Fig. 2.12. Schematic representing a particle (grey, centre) suspended in a medium with positive and negative ions. Due to the positive surface charge on the particle, an electrical double layer is formed. The Zeta potential is the electric potential measured at the slipping plane (dotted line). 45

Fig. 2.13. Weak anchoring condition: anchoring breaks in order to make the total charge zero. At a distance, the director is not affected by the presence of the particle. 48

Fig. 2.14. Saturn ring (SR) and hyperbolic hedgehog (HH). Note that the SR has higher energy than the HH (since energy of defect is proportional to unit length (Eqn. 2.13)) so SR are unstable. 48

Fig. 2.15. Boojums occur at the poles of a particle with homogeneous alignment. 49

Fig. 3.1. Diagram showing cross-section of typical sample, and cell gap d. Note that ITO and alignment layers were not used in all samples. 58

Fig. 3.2. Schematic representation of a particle displaced axially in a Gaussian beam, after the focus of the trap. Note that the beam, therefore the pressure, is highest at the centre of the beam (ray b). 64

Fig. 3.3. Representation of change in momentum of rays a and c from Fig. 3.2. The change in momentum of the photons (Δpa, Δpc) is equal to the difference between momentum of the photons entering the particle (kin) and the momentum of photons leaving the particle ($kout$). The 'missing' momentum is transferred to the particle. 65

Fig. 3.4. Force acting on particle due to change in direction of photons in ray a and ray c (Fa and Fc respectively). The resultant force is Fax. In this case, for a positive axial displacement relative to the centre of the trap, Fax acts to move the particle back towards the centre of the trap. Due to symmetry, there is no force perpendicular to the propagation direction of the beam. 65

Fig. 3.5. Schematic diagram representing a particle displaced in a direction perpendicular to the propagation direction of a Gaussian beam. 66

Fig. 3.6. The change in momentum of ray a and ray c for a transverse displacement (Fig. 3.5) causes forces on the particle Fa and Fc respectively, with resultant force $Ftra$. Fc is larger than Fa, as Fc originates from a ray from the centre of the beam, where the beam is more intense and therefore the number of photons and momentum transfer is greater. This means that Fc has more effect than Fa, so $Ftra$ acts in a direction to restore the particle towards the centre of the trap. 67

Fig. 3.7. Schematic diagram illustrating the principles of optical trapping along the z-axis [7] in a single Gaussian TEM_{00} beam. The beam's profile is perpendicular to the page and its propagation direction is parallel to the z axis. In this example we are considering the z component only and assuming that the particle is fixed on the z axis at x = y = 0. The total momentum transferred to the particle $ktot$ is equal to the momentum entering the particle kin minus the momentum transferred out of the particle $kout$. The change is caused by scattering and gradient forces. The resultant force either pushes the particle in the direction of the beam's propagation (a, b) or in the reverse direction of the beam's propagation (c), depending on whether $kin > kout$. Where $kin = kout$, stable trapping will occur. It should be noted that the position where stable trapping occurs is between (b) and (c), not at the 'geometrical focus', but further along the direction of the beam's propagation. A graph of resultant forces corresponding to this diagram is shown in Fig. 3.8 below. 68

Fig. 3.8. Illustrative plot of resultant forces along z axis for particles trapped in the Gaussian beam illustrated in Fig. 3.7 above, including positions marked in Fig. 3.7 a), b) and c). At position a), a positive force acts along the z-axis. At b), the point of highest intensity in the beam, the force is still positive. At point c), the resultant force is negative and the particle moves towards the origin of the beam. The 'centre' of the trap is the point where $F_z = 0$, which is after the point of highest intensity of the beam. 69

Fig. 3.9. Schematic diagram illustrating the optical setup for the Nikon laser tweezing system. The AOM is an acousto-optic modulator which modifies the path of the laser beam. For more details of components, see below. 73

Fig. 3.10. Representation of Bragg diffraction in an acousto-optic modulator. The light and dark strips represent a sound wave, where the refractive index changes according to the amplitude at that point in the medium [7]. 75

Fig. 4.1. Chemical structures of a) glycerol dimethacrylate (GDMA) and b) *N*-hydroxyethyl acrylamide (HEAm)..... 83

Fig. 4.2 Schematic representing the physical shape and structure of a) spherical particles, SRB 288 and b) Doublets (left) and triplets (b) in SRB-383. The physical shape was verified by tunnelling electron microscopy[11]. Spherical particles consist of GDMA only, and the doublets/triplets consist of GDMA and HEAm. 83

Fig. 4.3. Dielectric constants as a function of temperature..... 96

Fig. 4.4 Splay elastic constants as a function of temperature 97

Fig. 4.5. Bend elastic constants as a function of temperature..... 97

Fig. 4.6. Ordinary refractive index as a function of temperature. Note that the outlier was not used in the fitting for calculating the order parameter. 98

Fig. 4.7 Extraordinary refractive index as a function of temperature ... 99

Fig. 4.8. Order parameter as a function of temperature 100

Fig. 5.1. The mean square displacement of a particle undergoing Brownian motion is linear. 107

Fig. 5.2. The MSD of a highly confined particle should be constant. . 107

Fig. 5.3. MSD of a particle that diffuses freely at short timescales, and is confined at longer timescales (note: scales are log scales). 108

Fig. 5.4. Exponential fitting of MSD for x-component (1D case) of particle trapped at defect from chapter 6. 111

Fig. 5.5. At small timescales, under ~50 ms, few data points are present. (result is a component of particle confined at a line defect). This result is from a one-dimensional component of displacement only. 113

Fig. 5.6. A drop in MSD was sometimes observed at timescales typically above 100 s. At shorter timescales, the MSD appears to behave as expected for a freely diffusing/partially confined particle. 114

Fig. 5.7. Schematic diagram representing cross-section of a sample, with some possible causes of drift. In box with dotted line is motion that allows physical properties of particle and medium to be investigated. 115

Fig. 5.8. The mean square displacement of a particle stuck to the inner surface of a sample before and after drift correction. Note that drift only becomes apparent after ~1 s timescales or larger.116

Fig. 5.9. Histogram of particle displacement, showing two peaks. The plot suggests a shift in position has occurred at some time over the measurement period. 117

Fig. 5.10. a) profile of histogram of raw data before normalisation from Fig. 5.9. The heights of the centres of the bins were fitted to produce b). double Gaussian fit of profile of a). 119

Fig. 5.11. Pattern observed in particle position. 120

Fig. 6.1. Leica microscope laser tweezing setup. The layout is almost identical to the Nikon setup in chapter 4. 125

Fig. 6.2. Image of particle trapped at a line defect in MLC-6648, taken by polarising microscopy. The laser trap could be used to pull the particle off the defect if needed. 128

Fig. 6.3. MSD for 4 μm particle trapped in ±1 defect. The form is approximately as predicted in Eqn. 6.2. 129

Fig. 6.4. Graph of exponential fitting of same data in Fig. 6.3 above.. 130

Fig. 6.5. Histogram of particle positions for particle trapped in a ±1 defect. Probability is given as a %. 131

Fig. 6.6. The MSD for a particle trapped at line defect in MLC-6648 was of the same form as a particle trapped at a point defect. 132

Fig. 6.7. MSD of particle adhered to substrate in MLC-6648. In timescales in the 10s of seconds, the MSD increases exponentially, as would occur if linear drift were occurring. 133

Fig. 6.8. After drift correction, the MSD is approximately constant. ... 133

Fig. 6.9. Histogram of particle confined on surface of glass after drift correction. The histogram has a similar form to that of a particle confined at a defect. In this case, the distribution is very nearly Gaussian. 134

Fig. 6.10. Scatter plot of position for particle in MLC-6648, away from defects (measured over a timescale of approximately 100 s). 135

Fig. 6.11. The mean square displacement of particle dispersed in MLC-6648 away from defects was linear, except at timescales of above ~100 s. For comments on the drop at longer timescales, see chapter 5. 136

Fig. 6.12 Mean square displacement of particle in Fig. 6.11 with linear fit, at short timescales. 137

Fig. 6.13. Histogram of positions for a particle away from a defect. The distribution is definitely not Gaussian. 138

Fig. 6.14. Chemical structure of DMOAP bound to a glass surface, based on diagram from D'Elia and Barna et al [9]. Note that the first part of the alkyl chain runs parallel to the substrate, whereas the second alkyl chain is oriented perpendicular to the substrate 139

Fig. 6.15. Images of 5 μm DMOAP-treated borosilicate particles in 5CB, with satellite defects: a) Saturn ring defect b) Hyperbolic hedgehog defect. Image b) had its contrast and brightness enhanced digitally. 141

Fig. 6.16. Image of 5 μm DMOAP treated particle in MLC-6648. Note that the hyperbolic hedgehog satellite defect is attached to the line defect. 141

6.17. MSD for particle with HH defect at ±1 defect in MLC-6648. 142

Fig. 6.18. Histogram/scatter plot for particle with HH defect at ±1 defect in MLC-6648 143

Fig. 6.19. Scatter plot showing the location of DMOAP-treated particle with HH defect at ±1 defect in MLC-6648 143

Fig. 6.20. Symmetries of director around particle with weak anchoring vs particle with hyperbolic hedgehog satellite defect.145

Fig. 6.21. The confinement strengths of particles confined in MLC-6648, for melamine and DMOAP-treated borosilicate particles. . 146

Fig. 6.22. Image of particle with hyperbolic hedgehog defect in 5CB. The edges of the particle as determined by the software are shown in black, and the centre of the particle as determined by the software is shown in red. The calculated centre of the particle has been shifted towards the hyperbolic hedgehog defect compared to the physical centre. 147

Fig. 6.23. If the particle and defect maintain the same position relative to each other, it should not affect the confinement strength, but if the defect and particle move relative to each other, it may affect results..... 147

Fig. 6.24. MSD for 5 µm borosilicate particle with HH defect at ±1 defect in 5CB. 150

Fig. 6.25. MSD for particle with HH defect at ±1 defect in MLC-6648. . 150

Fig. 6.26 Scatter plot of location of 5 µm particle in 10 µm cell, before drift correction. 152

Fig. 6.27. Scatter plot of location of 5 µm particle in 10 µm cell, at ±1 defect, after drift correction. 152

Fig. 6.28. MSD for particle in 10 µm cell, before drift correction. 153

Fig. 6.29. MSD for particle 5 µm particle in 10 µm cell, at ±1 defect after drift correction. 153

Fig. 6.30. MSD for 2 µm particle confined at ±1 defect in 5CB..... 155

Fig. 6.31. MSD for 2 µm particle confined at ±1 defect in 5CB..... 155

Fig. 6.32. Confinement strength for 5 µm borosilicate particles with DMOAP, in ±1 defects in 5CB vs. MLC-6648. 156

Fig. 6.33 . Splay and bend elastic constants of 5CB and MLC-6648. The elastic constant for MLC-6648 was recorded at 'room temperature', assumed to be ~20°C, and the values for 5CB are given at 20°C..... 157

Fig. 6.34. Confinement strength as a function of cell gap for 5 µm particles confined in ±1 defects in 5CB..... 158

Fig. 6.35. Trajectory of y-component of particle in 19 µm cell. There is an appearance of drift that is not linear. 159

Fig. 6.36. Histogram of particle position in 19 µm cell. While the profile appears almost Gaussian, there is a large amount of noise. 159

Fig. 6.37. Strength of confinement for 2 μm particles and 5 μm particles, measured at ±1 defects in 5CB. If there is an effect on confinement strength due to particle size, it is not large in the case of these two particles. 161

Fig. 7.1. Chemical structures of a) glycerol dimethacrylate (GDMA) and b) *N*-hydroxyethyl acrylamide (HEAm)..... 167

Fig. 7.2. Composition of ~500 nm doublet- and triplet-shaped Janus particles. Shape was confirmed by scanning electron microscopy (SEM) by Butterworth et al [26]. 167

Fig. 7.3. Approximate shape of 50 μm Commercial Janus Particle, with photograph (from Cospheric LLC). Composition is not known, but is based on polyethylene with some additives. 168

Fig. 7.4. Chemical structures of a) PMMA and b) PS. The structure of the particles is intermediate between spherical and doublet-shaped. Particles were approximately ~5 μm in diameter, but were quite polydisperse, with some of the smaller particles half the diameter of the largest. 170

Fig. 7.5. Approximate shape and composition of ~5 μm Janus Particles. 170

Fig. 7.6. Janus particles suspended in water. Note that the particles are very polydisperse, and variations in Janus particle morphology can be seen. 171

Fig. 7.7. Reproduced from chapter 3. In conventional polarising microscopy, the orientation of the optic axis in the x-y plane cannot be determined. If a lambda waveplate (vibration direction γ) can be inserted at 45° to the crossed polarisers, one can determine whether the optic axis is lying parallel or perpendicular to the vibration direction of the wave plate. The birefringence colours are either additive (e.g. blue) or subtractive (e.g. yellow). 172

Fig. 7.8. Janus particle without DMOAP treatment under a) optical microscope, b) polarising microscope (rubbing direction shown with yellow arrows) c) polarising microscope with lambda plate, vibration direction shown with γ. From the subtractive and additive birefringence colours (represented by blue (+) and yellow (-)) we estimated the orientation of the director shown in d). In this case, the alignment appears to be approximately planar. 173

Fig. 7.9. Janus particle with DMOAP treatment under a) optical microscope, b) polarising microscope (rubbing direction shown with yellow arrows) c) polarising microscope with lambda plate, vibration direction shown with γ. From the subtractive and additive birefringence colours (represented by blue (+) and yellow (-)) we estimated the orientation of the director shown in d). The alignment appears to be homeotropic on one side, and planar or weakly anchored on the other side. 174

Fig. 7.10. Janus particle with DMOAP treatment under a) optical microscope, b) polarising microscope (rubbing direction shown with yellow arrows) c) polarising microscope with lambda plate, vibration direction shown with γ. From the subtractive and additive birefringence colours (represented by blue (+) and yellow (-)) we estimated the orientation of the director shown in d). The alignment appears to be approximately planar on one side, and approximately homeotropic on the other side. 175

Fig. 7.11. Janus particle with DMOAP treatment under a) optical microscope, b) polarising microscope (rubbing direction shown with yellow arrows) c) polarising microscope with lambda plate, vibration direction shown with γ. From the subtractive and additive birefringence colours (represented by blue (+) and yellow (-)) we estimated the orientation of the director shown in d). The alignment was assumed to be weak on one side, and homeotropic on the other side. 175

Fig. 7.12. Alignment of 5CB on PMMA flats, where b) is rotated 45 ° relative to a). Edge of liquid crystal is shown running horizontally in a), with the liquid crystal at the top. 177

Fig. 7.13. Alignment of 5CB on PS flats, where b) is rotated 45 ° relative to a). Edge of liquid crystal is shown running horizontally in a), with liquid crystal at the top. 177

Fig. 7.14. Some Janus particles appeared to undergo some movement when the electric field is applied. Movement is reversible for at least 3 on-off cycles. The displacement is a similar magnitude to the particle diameter. 178

Fig. 8.1. Structure for two bent-core compounds, 'compound 1' and 'compound 2' [32]. The phase behaviour is also described, where Iso is the isotropic phase, N is the nematic phase, SmX is an unknown smectic phase, Cr is Crystalline, and DC is the 'dark conglomerate' phase. The dark conglomerate phases [33] consist of 'sponge-like' structures of smectic layers, and are optically isotropic. 188

Fig. 8.2. The elastic constants of 'Compound 1'. Reproduced from data published in [32], with permission. At low temperatures, the nematic phase approaches an unknown smectic phase. 190

Fig. 8.3. The elastic constants of 'Compound 2'. Reproduced from data published in [34], with permission. At low temperatures, the nematic phase approaches the dark conglomerate phase. .. 190

Fig. 8.4. Chemical structure of SDS ($CH_3(CH_2)_{11}SO_4Na$). The nonpolar hydrocarbon chain is not soluble in water (hydrophobic). The sodium ion is polar, and highly soluble in water (hydrophilic). In addition to its usefulness as a detergent, SDS also forms liquid crystalline phases at certain concentrations in water. 193

Fig. 8.5. A variety of phases and structures associated with lyotropic liquid crystals. Amphiphilic molecules may form lamellar (a) and hexagonal (c) phases at high concentrations, and micelles (b) and vesicles (d) at lower concentrations. The structure adopted will depend on the type of solvent and solute molecule, and the concentration. Temperature is also a factor. Note that not all of these structures represent examples of liquid crystals. For example, a suspension of micelles (b) and/or vesicles (d) does not exhibit any type of long-range order, which would be required for a liquid crystal. 194

Fig. 8.6. Chemical diagram of sunset yellow. 196

Fig. 8.7. Representation of a nematic (N) phase formed by stacks of molecules in a chromonic liquid crystal such as SSY. [49, 50] .. 197

Fig. 8.8. Illustration of SIM, adapted from [73]. Moiré fringes are generated from overlapping structures, such as these two periodic gratings in a): the moiré fringes are the 'vertical stripes' seen at the overlap between the two gratings. In reciprocal (or Fourier transform) space, further from the centre represents higher spatial frequencies. The highest special frequencies resolvable by conventional microscopy are shown in b). The Fourier transform of a sinusoidal pattern can entirely be encoded in three points in c). Superimposing the illumination onto a sample increases, as seen in d). Using other orientations of the illumination pattern can increase the amount of reciprocal space (and therefore spatial frequencies) still further, up to ~2x. 201

Fig. 8.9. Illustration of STORM, adapted from [72]. Fluorophores are put into a non-fluorescing 'dark' state when illuminated by a laser pulse (e.g. red). When illuminated by a second laser pulse (e.g. green), some proportion of the fluorophores will fluoresce. With repeated cycles of illumination, an image of the fluorophores can be built up. Fluorophores may be much closer together than the resolution limit, even at separations as small as ~20 nm. 202

Fig. 8.10. Construction of ZBD. The 'defect state' D-state (left) and 'continuous state' C-state (right). 203

Fig. 8.11.Cross-section of ZBD grating in D-State and C-State. In the D-state negative -1/2 defects (-) are formed at the concave surface at the top of the grating, and positive +1/2 defects are formed at the concave surface at the bottom. Note that the commercial ZBD has a grating with 0.8 μm pitch and 1.0 μm amplitude [75]. 203

List of Abbreviations

5CB	4-Cyano-4'-pentylbiphenyl
8CB	4-n-octyl-4′-cyanobiphenyl
AOM	Acousto-optic modulator
BECD	Bistable electrophoretically controlled nematic display
BTBP	N,N′-Bis(2,5-di-tert-butylphenyl)-3,4,9,10-perylenedicarboximide
CCD	Charge coupled device
CMOS	Complementary metal-oxide-semiconductor
Cr	Crystalline phase
CRT	Cathode ray tube
C-State	Continuous state
DC	Dark conglomorate
DI	De-ionised
DLS	Dynamic light scattering
DMOAP	N-dimethyl-n-octadecyl-3-aminopropyltrimethoxysilychloride
D-State	Defect state
EPD	Electrophoretic display
GDMA	glycerol dimethacrylate
HEAm	*N*-hydroxyethyl acrylamide

HG	Homogeneous
HH	Hyperbolic hedgehog
HT	Homeotropic
InP	Indium phosphide
IPA	Isopropyl alcohol
IPS	In-Plane switching
Iso	Isotropic phase
LC	Liquid crystal
LCD	Liquid crystal display (or liquid crystal device)
LDV	Laser Doppler velocimetry
MF	Melamine formaldehyde
MFPD	Mobile fine particle display
MSD	Mean square displacement
N	Nematic phase
OLED	Organic light-emitting diode
PALS	Phased
PMMA	Poly(methyl methacrylate)
PS	Polystyrene
PVA	Polyvinyl alcohol
SDS	Sodium dodecyl sulphate
SEM	Scanning electron microscopy

SIM	Structured illumination microscopy
SmX	Unknown smectic phase
SLS	Sodium lauryl sulphate
SNAP	Specifications for Newsprint Advertising Production
SR	Saturn ring
SSY	Sunset yellow
STORM	Stochastic temporal optically resolved microscopy
TN	Twisted nematic
UV	Ultraviolet
ZBD	Zenithal bistable display

List of Symbols

Greek Letters

α	Molecular polarizability
$\Delta\alpha$	Anisotropy of molecular polarizability
γ	Rotational viscosity
γ_{vuks}	Dimensionless constant in Vuks relation
Γ	Relative optical path difference (or retardance)
δ	Optical path difference
ϵ, ε	Dielectric constant (or relative permittivity)
$\varepsilon_{\parallel}$	Dielectric constant parallel to director
$\varepsilon_{\perp}$	Dielectric constant perpendicular to director
ϵ_0	Permittivity of free space
ε_{lc}	Dielectric constant of liquid crystal
ε_m	Dielectric constant of medium
ε_s	Dielectric constant of sphere
ζ	Zeta potential
η	Viscosity
η_1, η_2, η_3	Miesowicz viscosities
η_i^{diff}	Combination of Miesowicz viscosities in i direction

θ	Angles of molecules in nematic LC relative to director
θ^{anc}	Polar angle (or ‘pretilt’) for anchoring at surface
θ_0^{anc}	Polar angle at lowest energy
θ^{ave}	Angle between the average director and the normal to the substrate
θ_{Bragg}	Bragg angle
θ_{DLS}	Scattering angle (dynamic light scattering)
θ_{WP}	Angle of vibration direction relative to fast axis (light in a wave plate)
κ	Trap stiffness
λ	Wavelength of laser trap
Λ	Wavelength of sound waves (in AOM)
λ_0	Wavelength of first maximum of interference fringes
λ_{inc}	Wavelength of incident light
λ_{DLS}	Wavelength of laser in dynamic light scattering
λ_N	Wavelength of last maximum of interference fringes
λ_{ph}	Wavelength of photon
λ_{vac}	Wavelength of light in a vacuum
λ_{LDV}	Wavelength of reference beam, laser Doppler velocimetry
μ	Relative permeability
μ_0	Permeability of free space

ξ	Drag coefficient
ξ_i	Drag coefficient in direction i
ρ	Probability density
σ	Standard deviation
$\boldsymbol{\tau}$	Torque
$\tau_{\boldsymbol{DLS}}$	Time delay (dynamic light scattering)
$\Delta\varphi$	Phase difference
ϕ^{anc}	Azimuthal angle for anchoring at surface
ϕ_0^{anc}	Azimuthal angle at lowest energy
ϕ^{ave}	Average angle between the average director and the normal to the substrate
ϕ^{OA}	Angle of optic axis relative to polariser
ψ	Potential of electrical double layer

Roman Letters

a	Radius of particle
A	Constant in Gaussian distribution
A_1	Fitting parameter in exponential fitting
A_2	Fitting parameter in Gaussian fitting

B	Constant in Gaussian distribution
c	Speed of light in a vacuum
c_{ion}	Molar concentration of ions
C	Capacitance (filled cell)
C_0	Capacitance (empty cell)
d	Cell gap
d_{med}	Distance travelled through medium
D	Diffusion coefficient
D_i	Diameter of ith particle in DLS
D_{sphere}	Diffusion coefficient for a sphere
D_Z	Z-average diameter of particles measured in DLS
e	Charge on the electron
E	Electric field strength
$\boldsymbol{E}$	Electric field
$\boldsymbol{E_e}$	Electric field of extraordinary ray
$\boldsymbol{E}_{eph}$	Electric field applied to particle
E_{LD}	Energy of line defect
$\boldsymbol{E_o}$	Electric field of ordinary ray
E_r	Threshold electric field strength for Quincke rotation
$\boldsymbol{E}_{total}$	Total electric field

F	Force
f	Function
$f_{doppler}$	Doppler shift
F_E	Free energy per unit volume due to orientation of dipoles in electric field
F_d	Free energy per unit volume due to elastic distortion in liquid crystal
$\boldsymbol{F}_a$, $\boldsymbol{F}_c$	Force on particle due to rays a and c, respectively
$\boldsymbol{F}_{ax}$	Axial force on particle in optical trap
$\boldsymbol{F}_{gradient}$	Gradient force on particle in optical trap
$\boldsymbol{F}_{particle}$	Resultant force on particle
$\boldsymbol{F}_{scat}$	Scattering force on particle in optical trap
$\boldsymbol{F}_{tra}$	Transverse force on particle in optical trap
g	Autocorrelation function (dynamic light scattering)
h	Planck's constant
i	Integer
I_0	Intensity of incident light
I_{ion}	Ionic strength
I_s	Intensity of speckle pattern (dynamic light scattering)
I_t	Intensity of transmitted light
k_B	Boltzmann's constant

$\boldsymbol{k_{in}}$	Momentum transferred to particle
$\boldsymbol{k_{out}}$	Momentum transferred away from particle
$\boldsymbol{k_{tot}}$	Total momentum transferred to particle
K	Approximation of elastic constants
K_{11}	Splay elastic constant
K_{22}	Twist elastic constant
K_{24}	Saddle-splay elastic constant
K_{33}	Bend elastic constant
L	Length of line defect
m	Positive integer (1, 2, 3…)
m_p	Mass of particle
n	Refractive index
$\boldsymbol{n}$	Director
N	Nematic phase
n_1	Refractive index of medium
n_2	Refractive index of particle
n_e	Refractive index of extraordinary ray travelling perpendicular to the optic axis
$n_e{}'$	Refractive index of extraordinary ray
n_o	Refractive index of ordinary ray
n_{rel}	Relative refractive index of particle to medium

Δn	Birefringence
N_A	Avogadro's number ($\simeq 6.022 \times 10^{23}$)
NA	Numerical aperture
$\boldsymbol{p}$	Momentum
P	Laser power
$\Delta \boldsymbol{p_a}$, $\Delta \boldsymbol{p_c}$	Change of momentum of photon
p_{ph}	Momentum of photon
q	Electric charge
q_{DLS}	Scattering wavevector (dynamic light scattering)
Q	Topological charge
Q_{OT}	Efficiency of optical trap
r	Displacement
r_{mean}	Mean displacement
r_{limit}	Resolution limit
$\boldsymbol{R}$	Displacement vector
R_i	Displacement in direction i
s	Winding number
S	Orientational order parameter
S_A	Smectic A phase
t	Time

t_1	Fitting parameter for exponential fitting
T	Temperature
T_{NI}	Temperature of nematic-isotropic transition
U	Potential energy
U_E	Electrophoretic mobility
v	Speed of light (in a dielectric), phase velocity
$\boldsymbol{v}_{drift}$	Drift velocity
V_{thr}	Threshold voltage
w	Fitting parameter in Gaussian fitting
W	Anchoring energy
W_0	Constant term in anchoring energy
W_ϕ, W_θ	Coefficient terms in anchoring energy
x	Any real number (used for exponential and Gaussian function)
x_c	Fitting parameter for Gaussian fitting
y	Dependent variable of exponential or Gaussian fitting
y_0	Fitting parameter for exponential fitting
y_1	Fitting parameter for Gaussian fitting
z_{ion}	Charge number for an ion

Chapter 1 Display Devices and Electronic Paper

1.1 Introduction

There is no doubt that electronic display devices have become an inescapable part of life. Perhaps you were woken by a digital alarm or mobile phone early this morning. It is not unlikely that, instead of paper, you are reading this dissertation on an electronic display screen. Even the coffee keeping you awake may have been heated up by a coffee maker with a digital display. Such ubiquity has become even more widespread since the bulkier, heavier cathode ray tube (CRT) display was displaced by the liquid crystal display (LCD) and its rivals.

It may seem like there are few challenges left for the displays industry, given the huge progress in the past decades [1]. However, in this chapter, we shall see that no display is without its limitations. Challenges for today's display researchers to solve include developing true three-dimensional displays [2 – 5], flexible displays [6 – 8], and continuing to reduce power consumption. Here, we will discuss the current limitations on electronic paper, and how they might be overcome in the future.

1.2 Electronic Paper

One class of displays, known as 'electronic paper', was reviewed in 2011 by Heikenfeld et al [9] and in 2014 by Bai et al [10]. There is no strict definition, but electronic paper usually emulates conventional paper by having low reflectivity, high contrast and as low a power consumption as possible.

In terms of contrast, as an example, the recommendations of SNAP (Specifications for Newsprint Advertising Production) [11], which sets a standard for contrast in printed advertisements in the USA, convert to a

contrast ratio of at least ~10:1 [9]. This target is met by most electronic paper type devices [9], unlike some other display types.

Power consumption is especially a concern for portable devices: for example, many mobile phones currently require mains charging at least once per day. Lowering the power consumption of mobile devices significantly could eliminate mains charging altogether, since methods such as wireless charging [12] would become more feasible. Although other components consume power, displays remain one of the largest consumers of power in mobile phones and laptops [13, 14].

As will be discussed below, most electronic paper types achieve their low power and optical properties at the expense of speed. Response times can be a critical issue. The response time of the elements of the display must be shorter than refresh rate. While refresh rates of ~1 s are acceptable for static images (for example, if reading an electronic book, this is comparable to turning a physical page), video images require faster switching times. In the UK, the standard (PAL) frame rate for video is 25 Hz [15], requiring a response time at the very maximum of 40 ms. Electronic paper technologies do not currently reach this standard. A typical example, the commercially successful electronic paper E-Ink [16] has an update time of at least 240ms. To this day, the challenge is to develop electronic paper that is capable of showing video [9, 10]. It should be mentioned here that speed can also be critical, not just to video, but also if greyscale or colour is required. A number of textbooks discuss this topic, for example the Handbook of Liquid Crystals Volume 8 [17].

1.2.1 Approaches to Reduce Power Consumption

There are a number of strategies which can lower power consumption, which apply across many device types. For example, most displays require power to be supplied to maintain a pixel in a bright or dark state. If power is only needed to switch between states, and not to maintain states, a display is known as ‘bistable’, or ‘multistable’ if more than two states are available. Instead of addressing the power used to switch the display, some types of

display save power by not relying on a backlight. If high quality images can be created purely from ambient light, the display is ‘reflective’. In a study by Mahesri and Vardhan [14] breaking down the power consumption of a laptop, the backlight was found to be responsible for the most power consumption within the display, consuming between 0.5 and 3.5 W, whereas the difference between a black and white background was less than 0.1 W. Most electronic paper types are both bi/multi-stable and can operate in reflective mode.

1.3 Liquid Crystal Displays

The largest number of displays found today are based on liquid crystals. Historically, the most commonly used is the twisted nematic (TN) device [18, 19] although other configurations such as in-plane switching (IPS) are now more popular for some devices requiring high resolution, such as mobile phones [20]. The speed of liquid crystal displays in general is very fast (~ 10 ms or lower), and requires ~ 1 V or more for switching, and ~ 10 V for the backlight (see section 1.2.1). Furthermore, conventional nematic display types all require polarisers, which reduces light intensity by an additional 50%, which again reduces efficiency. There are other nematic based displays (such as guest-host displays) that do not require polarisers, but such devices typically have with other drawbacks. For example, guest-host displays typically have relatively low contrast (~ 10:1), making it unsuitable for electronic paper applications.

1.3.1 LCDs adapted for low-power applications

Many of the LCD types designed to operate with especially low power consumption are based on an existing liquid crystal display type, adapted to reduce the power. For example, bistable LCDs have a largely conventional device construction but usually take advantage of anchoring conditions at the ‘inner surface’ of the device. A detailed chapter on bistable devices based on the nematic phase can be found in Volume 8, Chapter 4 of the Handbook of Liquid Crystals [21], as well as Jones 2012 [22].

The simplest example of a bistable nematic device is the pi-cell which is also noted for its very high speed (< ms [23]). Another device, the so-called zenithal bistable display (ZBD), is described briefly in chapter 8. The ZBD uses a 3D sinusoidal grating on the micron scale as one of its inner surface with two possible anchoring states, very close in energy, that can be latched via the flexoelectric effect.

1.4 Electrophoretic Displays

Another very successful approach to displays, especially so-called e-paper, is based on particles of reflecting or absorbing pigment. There are some variations in device design, but in general such devices depend on charged particles moving in an electric field (electrophoresis) and being obscured by each other and/or the medium. The first paper demonstrating a device based on electrophoresis was published in 1973 by Ota, Ohnishi and Yoshiyama [24], but this class of displays has been improved over the years, with suppliers such as E-Ink [16] becoming commercially successful. The operation of E-Ink is shown in Fig. 1.1 below.

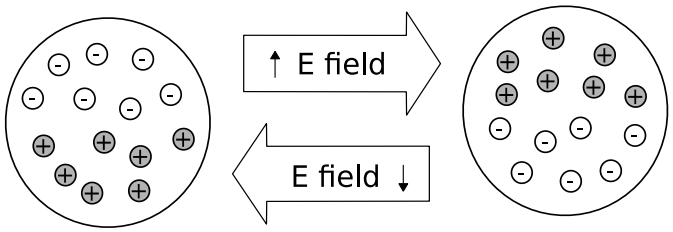

Fig. 1.1. Figurative representation of the operation of e-ink [16], one of the most commercially successful electrophoretic displays. Positively and negatively charged particles of pigment are suspended in a medium. Particles are neutrally buoyant, making the device bistable. Applying an electric field swaps the positions of the particles. Assuming this diagram is a vertical cross section, a view looking from above will see either white (left) or black (right). The pigment particles are contained in capsules which reduce the chance of particle flocculation over time, and also acts as the unit 'pixel' for the display.

Most electrophoretic displays (EPDs) are both bistable and operate well in reflective mode. Possibly the largest downside of EPDs is the relatively slow response time [25] (typically ~ 200 ms), which is sufficient for electronic books, but not fast enough to display video.

1.4.1 Janus Particle-based device: The Gyricon

One possible way to increase the speed of electrophoretic type displays is to use particles that rotate under an electric field (electro-rotation) instead of translating through the medium (electrophoresis). Instead of having two types of pigment particles, one of which is reflective, and the other absorptive, the two particle types can be combined in a single particle with two hemispheres, each made of a different material. Particles of this general type (consisting of two halves which have different properties) are known as 'Janus particles', a term coined by PG De Gennes [26]. This idea was developed at Xerox [27] to build a device called a 'Gyricon', patented in 1978 [27].

A simplified explanation of the Gyricon's operation will follow. If an electric field is applied to a Gyricon particle, the particle experiences torque, τ, given by:

$$\tau = \boldsymbol{p} \times \boldsymbol{E} \qquad \text{Eqn. 1.1}$$

where $\boldsymbol{p}$ is the particle's dipole moment, and $\boldsymbol{E}$ is the applied electric field, as shown in Fig. 1.2 below.

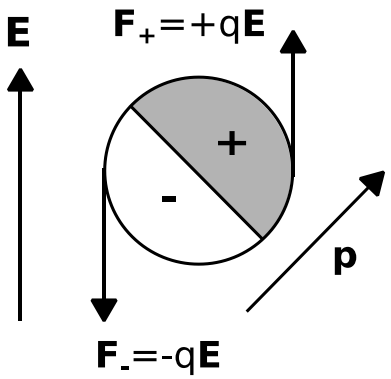

Fig. 1.2. Simplified diagram representing the rotation of a Gyricon particle in an electric field, based on the diagram in Crowley, Sheridon and Romano [28]. In a real device, electro-rotation forces are opposed by a viscous drag force.

Driving the electro-rotation requires the two materials in the particle to have different charges. While a Gyricon is faster than a conventional EPD (80-100 ms for the main prototype, but lower for some experimental models with smaller spheres [29]), the voltage required to operate it is so high (50 V - 150 V) that it is impractical for a portable device.

1.4.2 Other low-powered display types

For completeness, it is important to mention that there are some alternative technologies being researched [9,10], not least the electrofluidic displays reviewed by Yang et al [30]: electrofluidic displays are very promising in terms of delivering high quality images and even video speed [31], but problems in manufacturing are still being overcome [32, 33]. It is also worth mentioning the organic light emitting diode (OLED) display, which is now becoming a rival to the LCD, and has response times typically a thousand times faster than conventional nematic displays [34], and relatively low power consumption, but are more demanding to computer processors and more expensive to manufacture, especially for larger displays [25]. However, so far these newer types of low-powered displays have not all become commercially successful, and like the other display types discussed earlier in the chapter, all have some drawbacks either in power consumption, speed or image quality.

1.5 Summary of Low-Powered Display Devices

For reasons that will become clear, not every variation on device has been covered here. Table 1.1 compares some types in terms of the characteristics of electronic paper.

	TN	ZBD	Conventional EPD	Gyricon
Video speed (response times <40ms)	Yes	No	No	No
Bistability	No	Yes	Yes	Yes
Reflective mode	No*	No*	Yes	Yes
Low voltage (<10 V)	Yes	No	Yes	No
High Contrast Ratio (>10:1)	Yes [35]	Yes [36]	Yes	Not measured

Table 1.1. Comparison of properties of some types of low-powered display device. *: can be modified to operate in reflective mode, but doing so reduces contrast further. Note on the Gyricon: contrast has not been measured, but is possible if particles are made from high contrast materials

Clearly, each display type has its benefits and drawbacks. The key question that motivated the research in this thesis is whether it is possible to combine some of the positives of distinct display types, thereby producing a new display mode that is useful in electronic paper applications. Specifically, is it possible to combine the positive features of LCDs with the positives of displays that explicitly use particles?

Of course, there is a considerable body of work examining particles in liquid crystal systems; some background will be described in chapter 2. However, whether the positive sides of each system can be combined in a display is an open question. This thesis will go some way towards answering that question, as well as outlining some new effects found for particles in liquid crystals.

1.6 Displays based on Liquid Crystal Colloids

The idea of combining particles and liquid crystals in a display device has been approached, but not fully explored in the literature. A review article on the subject was published by Klein in 2013 [37], which describes prototype devices such as the 'filled nematic' [38 –40], the bistable electrophoretically controlled nematic display (BECD) [41 – 44], and mobile fine particle display (MFPD) [45 – 50]. While the BECD and MPFD are in many ways promising, there are significant hurdles to overcome in order to turn bring the LC (liquid crystal) colloid based devices described above up to a standard where they could be used commercially.

These technical challenges, which will be discussed in the following chapters, are not trivial. The physical behaviour of particles suspended in liquid crystals is a deeply complex topic. Indeed, 'liquid crystal colloids' is an area of significant interest within liquid crystals. Despite the large amount of literature available, there is much yet to be learned about LC colloids, both from a theoretical and experimental standpoint. Some of the less well understood aspects of LC colloids will be discussed in the upcoming chapter 2. It is clear that more understanding is needed if a commercial liquid crystal colloid based device is to become a reality.

1.7 Conclusion

In this chapter, a brief introduction has been given to the many different types of displays suitable for electronic paper applications. The advantages and drawbacks of different approaches were summarised, demonstrating none of the existing solutions has all the characteristics of the 'ideal' electronic paper including: video speed, low power consumption, and high contrast.

While we have touched on some of the methods that seek to address the challenges of achieving video-speed electronic paper, we have chosen the approach of combining some technology from particle-based displays such

as electrophoretic devices (known for their good optical properties), and liquid crystal type displays (known for their high speed).

Approaching this topic requires an understanding of the physical properties of liquid crystals, colloidal systems (i.e. small particles suspended in a medium), and their combined properties (liquid crystal colloids). This thesis will consider particles in liquid crystals in terms of their potential application to e-paper applications. In the next chapter (chapter 2), we shall outline some important properties of these systems, detailing the key physical principles that control the dispersion of particles in liquid crystals and their response to fields. The following chapter will introduce the methods of measuring some of these quantities. In the rest of the thesis, we will go on to describe the results of these experiments. The early chapters describe some preliminary work into how the bulk properties of a liquid crystal are affected by the addition of particles. After this, the research begins on understanding how particles physically interact with defects, and how the strength of the interactions can be quantified. The experimental sections will conclude with an initial investigation into Janus particles in nematic liquid crystals, taking the early steps towards building a hybrid liquid crystal/Gyricon based device. The final chapter contains a summary of the main conclusions drawn from the research, answering the question whether progress can be made towards a LC colloid based display device. Some suggestions for experiments for others aiming to continue this line of research, along with some very early experiments, will be found at the end of the thesis.

References

1. C. Hilsum, Philosophical Transactions. Series A, Mathematical, Physical, and Engineering Sciences **368**, 1027 (2010).

2. N. S. Holliman, N. A. Dodgson, G. E. Favalora, and L. Pockett, IEEE Transactions on Broadcasting **57**, 362 (2011).

3. G. Westheimer, Proceedings of the Royal Society of London B: Biological Sciences (2011).

4. L. Yang, H. Dong, A. Alelaiwi, and A. El Saddik, Multimedia Tools and Applications **75**, 17121 (2016).

5. M. S. Banks, D. M. Hoffman, J. Kim, and G. Wetzstein, Annual Review of Vision Science **2**, 397 (2016).

6. K. J. Allen, Proceedings of the IEEE **93**, 1394 (2005).

7. L. Collins, IEE Review **49**, 42 (2003).

8. S. M. Lee, J. H. Kwon, S. Kwon, and K. C. Choi, IEEE Transactions on Electron Devices **64**, 1922 (2017).

9. J. Heikenfeld, P. Drzaic, J.-S. Yeo, and T. Koch, Journal of the Society for Information Display **19**, 129 (2011).

10. P. F. Bai, R. A. Hayes, M. L. Jin, L. L. Shui, Z. Chuan Yi, L. Wang, X. Zhang, and G. F. Zhou, Progress in Electromagnetics Research **147**, 95 (2014).

11. (2017).

12. S. Y. R. Hui, Z. Wenxing, and C. K. Lee, IEEE Transactions on Power Electronics **29**, 4500 (2014).

13. H. J. S. Kothuru, in *Proceedings of the 6th Annual GRASP Symposium* (2010), pp. 133–134.

14. A. Mahesri and V. Vardhan, Lecture Notes in Computer Science **3471 LNCS**, 165 (2005).

15. C. Poynton, in *Digital Video and HDTV* (Elsevier, 2003), pp. 529–534.

16. J. M. Jacobson, US6120588 A (2000).

17. *Handbook of Liquid Crystals, Volume 8: Applications of Liquid Crystals*, 2nd ed. (Wiley, 2014).

18. R. H. Chen, in *Liquid Crystal Displays: Fundamental Physics and Technology* (Wiley, 2011).

19. P. Raynes, in *Handbook of Liquid Crystals, Volume 8: Applications of Liquid Crystals* (Wiley, 2014), pp. 1–20.

20. H. Hong, in *Handbook of Liquid Crystals, Volume 8: Applications of Liquid Crystals*, edited by Wiley (2014), pp. 21–40.

21. J. C. Jones, in *Handbook of Liquid Crystals, Volume 8: Applications of Liquid Crystals* (Wiley, 2014), pp. 87–145.

22. J. C. Jones, *Bistable Liquid Crystal Displays* (2012).

23. R. Guan, Y. Sun, and G. Fu, Liquid Crystals **35**, 841 (2008).

24. I. Ota, J. Ohnishi, and M. Yoshiyama, Proceedings of the IEEE **61**, 832 (1973).

25. R. H. Chen, in *Liquid Crystal Displays: Fundamental Physics and Technology* (Wiley, 2011), pp. 449–476.

26. P.-G. De Gennes, Reviews of Modern Physics **64**, 645 (1992).

27. N. K. Sheridon, US4126854 A (1978).

28. J. M. Crowley, N. K. Sheridon, and L. Romano, Journal of Electrostatics **55**, 247 (2002).

29. N. K. Sheridon, E. A. Richley, J. C. Mikkelsen, D. Tsuda, J. M. Crowley, K. A. Oraham, M. E. Howard, M. A. Rodin, R. Swidler, and R. Sprague, Journal of the SID **7**, 141 (1999).

30. S. Yang, J. Heikenfeld, E. Kreit, M. Hagedon, K. Dean, K. Zhou, S. Smith, and J. Rudolph, Journal of the Society for Information Display **19**, 608 (2011).

31. K. A. Dean, K. Zhou, S. Smith, B. Brollier, H. Atkuri, J. Rudolph, S. Yang,

S. Chevalliot, E. Kreit, and J. Heikenfeld, SID Symposium Digest of Technical Papers **42**, (2011).

32. S. Xu, B. Liu, C. Pan, L. Ren, B. Tang, Q. Hu, and L. Jiang, Journal of Materials Processing Technology **247**, 204 (2017).

33. H. Wu, B. Tang, R. A. Hayes, Y. Dou, Y. Guo, H. Jiang, and G. Zhou, Materials **9**, (2016).

34. B. Geffroy, P. le Roy, and C. Prat, Polymer International **55**, 572 (2006).

35. H.-K. Kim, D.-Y. Lee, and J.-K. Song, Liquid Crystals **38**, 1239 (2011).

36. J. C. Jones, Proceedings of SPIE **3955**, 84 (2000).

37. S. Klein, Liquid Crystals Reviews **1**, 52 (2013).

38. R. Eidenschink and W. H. De Jeu, Electronics Letters **27**, 1195 (1991).

39. M. Kreuzer, T. Tschudi, and R. Eidenschink, Molecular Crystals and Liquid Crystals **223**, 219 (1992).

40. S. Lee and C. Park, Molecular Crystals and Liquid Crystals **333**, 123 (1999).

41. D. Sikharulidze, Applied Physics Letters **86**, 1 (2005).

42. D. Sikharulidze, GB2424716B (2010).

43. D. Sikharulidze, US7791706B2 (2007).

44. D. Sikharulidze, US6970211B2 (2005).

45. M. Ogawa, T. Takahashi, S. Saito, Y. Toko, Y. Iwakura, K. Kobayashi, and T. Akahane, SID Symposium Digest of Technical Papers **34**, 584 (2003).

46. T. Takahashi, S. Saito, and Y. Toko, Japanese Journal of Applied Physics Part 1-Regular Papers Short Notes & Review Papers **43**, 7181 (2004).

47. D. Sikharulidze, GB2445375 (2011).

48. D. Sikharulidze, US7796199B2 (2010).

49. D. Sikharulidze, US7633581B2 (2009).

50. D. Sikharulidze, GB2425611B (2010).

Chapter 2 Introduction to Liquid Crystals, Colloids and Liquid Crystal Colloids

2.1 Introduction

The hypothesis outlined in chapter 1, building an electronic paper-like device from liquid crystal colloids, is still a challenge from the point of view of the underlying physics. A clear understanding of particle behaviour in liquid crystals must be achieved in order to build such a device.

This chapter will provide a theoretical background to the hypothesis, including some fundamental optics, the physics of liquid crystals, and an introduction to colloids. These sections will be vital to understanding the experimental methods described later in the thesis. Finally, the topic of liquid crystal colloids will be introduced. In particular, we will discuss what forces a particle will be subject to when suspended in a liquid crystal, with and without an applied electric field. In subsequent chapters, the knowledge outlined here will be used in the context of methods and analysis.

2.2 Optics of Birefringent Materials

Understanding many of the analysis techniques used in this project requires some familiarity with birefringence. As the theory behind birefringence can be quite in-depth, no derivations will be provided here, though details can be found in the general references provided. While most of the material in this section is based on chapter 8 of Hecht [1], it can be found in many other optics textbooks, as well as some liquid crystals books (such as chapter 4 of Chen [2]).

2.2.1 Refractive Index

Light travelling through a vacuum always travels at c, which is exactly $2.99792458 \times 10^8\ \mathrm{ms}^{-1}$, or $1/\sqrt{\epsilon_0\mu_0}$, where ϵ_0 is the permittivity of free

space and μ_0 is the permeability of free space. However, light travels at a different speed, v, when it passes through a dielectric material. The ratio of the speed v, to vacuum speed c is called the 'absolute refractive index', or just the 'refractive index', n:

$$n \equiv \frac{c}{v} = \sqrt{\frac{\epsilon\mu}{\epsilon_0\mu_0}} \qquad \text{Eqn. 2.1}$$

where ϵ is the material's dielectric constant (or relative permittivity) and μ is the material's relative permeability, both evaluated at the relevant optical frequency. Note that v refers to phase velocity as opposed to group velocity.

2.2.2 Birefringence

In some materials, the refractive index varies depending on the path light takes through the material. These materials are called 'birefringent'. A wave passing through a birefringent material can be decomposed into two plane waves, each of which travels at a different speed. These two waves are called the 'ordinary ray' (o-ray) and the 'extraordinary ray' (e-ray).

We will be discussing a special case of birefringence, 'uniaxial' materials, only. A 'uniaxial' material has a single axis of symmetry, the 'optic axis' and two refractive indices. The lower symmetry 'biaxial' materials are also birefringent, but have three refractive indices instead of two.

There are a number of ways to visualise and calculate the relationships between the e-ray and o-ray, but one of the most succinct is to refer to the 'refractive index ellipsoid' or 'refractive index indicatrix'. Given the wave normal of light passing through the material, an indicatrix can be used to calculate refractive indices experienced by the o-ray and the e-ray, as well as to find the vibration directions of both rays. Below in Fig. 2.1 is an example of a refractive index indicatrix for a uniaxial material, assuming the electric field of the wave propagating through the material $\boldsymbol{E}_{total}(t)$ is the sum of the electric fields of the o-ray and the e-ray.

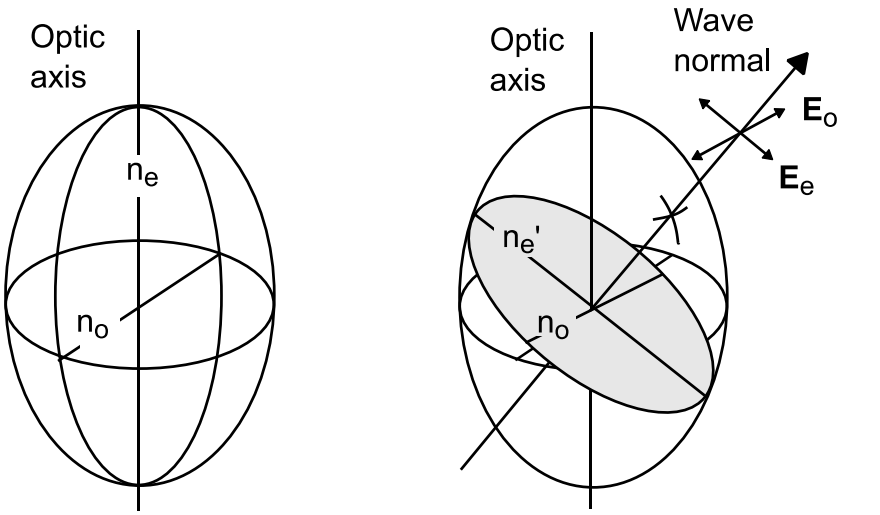

Fig. 2.1. a) A refractive index indicatrix for a 'positive' uniaxial material. b) Indicatrix used to find the vibration directions of the o-ray ($\boldsymbol{E_o}$) and the e-ray ($\boldsymbol{E_e}$), and the refractive indices experienced by them, $\boldsymbol{n_o}$ and $\boldsymbol{n_e'}$ respectively, where $\boldsymbol{n_0 \leq n_e' \leq n_e}$. The o-ray always vibrates perpendicular to the optic axis. $\boldsymbol{E_o}$ and $\boldsymbol{E_e}$ are always perpendicular to each other. This diagram is based on section 6.3 of Saleh and Teich, which also includes the full derivation and a more mathematical description of how the indicatrix is used.

From Fig. 2.1, n_o is experienced by any wave travelling along the optic axis. The refractive index n_e can only be experienced by an e-ray travelling perpendicular to the optic axis. In a 'positive' uniaxial material, $n_e > n_o$. For

this reason, the optic axis is sometimes referred to as the 'fast axis', with the 'slow axis' perpendicular to it. The difference between the largest refractive index, n_e, and the smallest, n_o:

$$\Delta n = (n_e - n_o) \qquad \text{Eqn. 2.2}$$

is known as the 'birefringence'.

2.2.3 Wave Plates and Wave Plate Conditions

Since ordinary and extraordinary rays travel at different rates, they pick up a relative optical path difference Γ, upon travelling distance d_{med} through the medium:

$$\Gamma = d_{med}(|n_o - n_e|). \qquad \text{Eqn. 2.3}$$

This translates to a phase difference $\Delta\varphi$ between the o-ray and e-ray:

$$\Delta\varphi = \frac{2\pi}{\lambda_{vac}}\Gamma. \qquad \text{Eqn. 2.4}$$

where λ_{vac} is the vacuum wavelength. There are a few special cases when the phase difference is equal to certain values: these are known as the 'wave plate' conditions.

2.2.4 Full Wave Plate

The full wave plate condition occurs where $\Delta\varphi = 2\pi$, (or a multiple thereof). Since waves with these values of phase difference are identical to a wave with no phase difference, a full wave plate has no effect on the polarisation state of a wave before and after passing through it. The condition occurs when the optical path difference is equal to a whole number of wavelengths:

$$\Gamma = m\lambda_{vac} \qquad \text{Eqn. 2.5}$$

where m is a positive integer. The value of m is sometimes referred to as the 'order'.

2.2.5 Half Wave Plate

Another wave plate condition is the half wave plate, which occurs where $\Delta\varphi = \pi,\ 3\pi,\ 5\pi$ ..., or:

$$\Gamma = (2m + 1)\lambda_{vac}/2, \qquad \text{Eqn. 2.6}$$

where m is a positive integer or zero. This corresponds to an incoming wave with vibration axis at θ_{WP} from the fast axis, being rotated by $2\theta_{WP}$ when it emerges, as illustrated in Fig. 2.2 below. In other words, the ordinary and extraordinary waves are retarded by half a wavelength with respect to each other, with the effect that the plane of polarisation is rotated by twice the angle θ_{WP}.

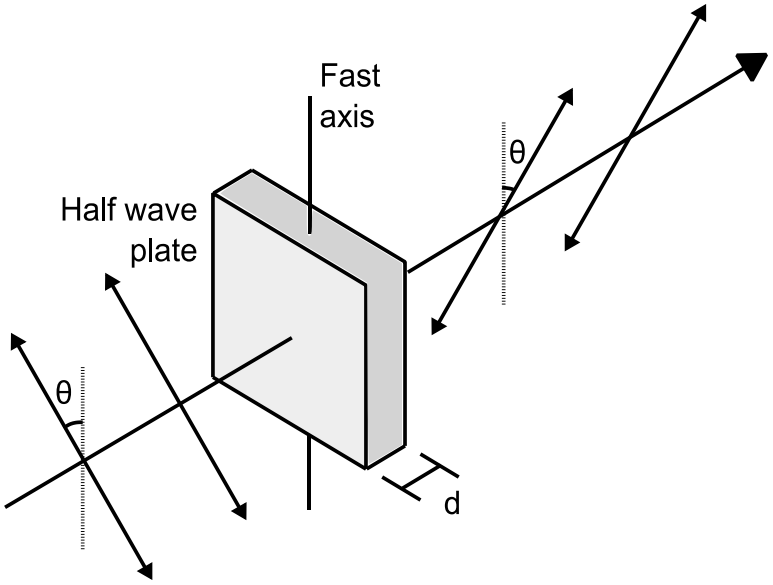

Fig. 2.2. A half-wave plate rotates the vibration direction of an incoming beam from $+\theta_{WP}$ to $-\theta_{WP}$, relative to the fast axis.

For example, if θ_{WP} is 45°, the direction of polarisation is rotated by 90°.

2.2.6 Quarter Wave Plate

While no quarter wave plates were used specifically during the project, for completeness, the quarter wave plate condition applies when $\Delta\varphi = \frac{\pi}{2}, \frac{3\pi}{2}, \frac{5\pi}{2}$.... Quarter wave plates can convert linearly polarised light to circularly polarised light and vice versa, depending on the initial polarisation direction with respect to the optic axis of the quarter wave plate.

2.2.7 Crossed Polarisers and Polarising Microscopy

As the wave plate conditions show, birefringent materials have an effect on the final direction or state of polarisation of light passing through a plate. One standard way to study birefringent liquid crystal materials is to place the sample in between two polarisers, with the transmission axes of the polarisers at 90° to each other. By convention, when a wave passes through crossed polarisers, the first one it passes through is the 'polariser' and the second is the 'analyser'. Studying samples in this way at high magnification (usually between ~10x and ~100x) is known as 'polarising microscopy'.

Polarising microscopy can be used to infer information about the orientation of the optic axis, the thickness of a sample, and/or the birefringence of the sample. To illustrate how such information is extracted from polarising microscopy, we will consider some special cases of birefringent materials under crossed polarisers.

For example, let's consider a birefringent, transparent sample between crossed polariser. There a are three reasons that light might not pass the analyser, described in Table 2.1 below, and illustrated by a diagram in Fig. 2.3, also below.

a) Either $\boldsymbol{n_e}$ or $\boldsymbol{n_o}$aligns with the polariser or analyser. Only one refractive index is experienced (either $\boldsymbol{n_e}$ or $\boldsymbol{n_o}$) respectively (see Fig. 2.3 a) and b) below). Therefore, no phase difference occurs between the ordinary and extraordinary rays, the polarisation direction is not changed, and no light passes the analyser.

b) The optic axis ($\boldsymbol{n_o}$) is in a plane perpendicular to the polariser and analyser, i.e. parallel to the incident light. Since only $\boldsymbol{n_o}$ is experienced, no phase difference occurs, the polarisation direction does not rotate, so no light passes the analyser. Shown in Fig. 2.3 c).

c) The full wave plate condition ($\Delta\varphi = 2\pi$). Although the polarisation direction does rotate while passing through the sample, after leaving the birefringent material, the direction of polarisation will have rotated a multiple of 180°. Again, no light passes the analyser. It should be noted that the full wave plate condition will only apply to certain wavelengths (Eqn. 2.4).

Table 2.1. Three conditions under which on observing no transmission through crossed polarisers, even if the sample is birefringent and transparent.

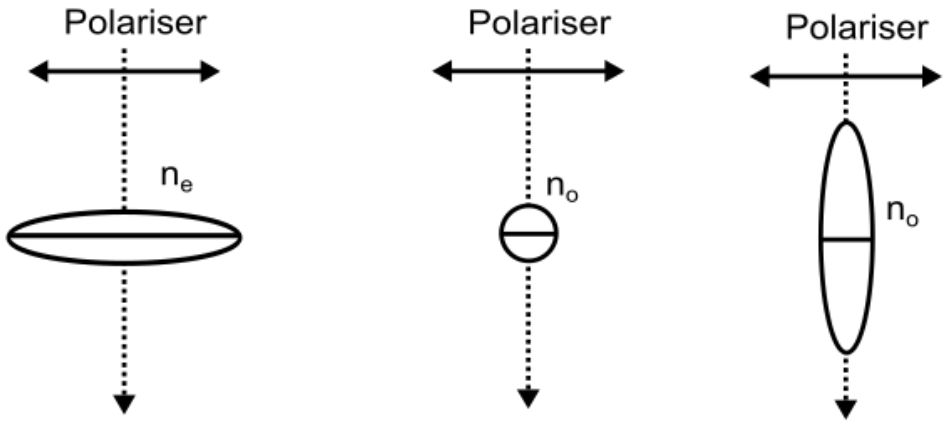

a) b) c)

Fig. 2.3 Representation of light (dotted line) passing through a birefringent sample, with the oval representing a cross-section of the refractive index ellipsoid. Under certain conditions, only one refractive index is experienced by light passing through a birefringent material. In this case, the polarisation direction does not rotate when passing through the material, even if the material is birefringent. In case a), n_e aligns with the polariser (and n_o aligns with the analyser), and only n_e is experienced. In case b), n_o aligns with the polariser, n_e aligns with the analyser, and only n_o is experienced. In case c), the optic axis is parallel to the propagation direction of the light, and only n_o is experienced.

To understand how birefringence colours are produced, we can consider case 3 in more detail. Say we have a 5 µm thick sample of a birefringent material between crossed polarisers, as shown in Fig. 2.4 below. The birefringent material has a refractive index of $\Delta n = 0.2$, typical for nematic liquid crystals. We can calculate from Eqn. 2.3 that polarised light passing through the sample experiences an optical path difference $\Gamma = 1000\ \mathrm{nm}$ between the ordinary and extraordinary rays.

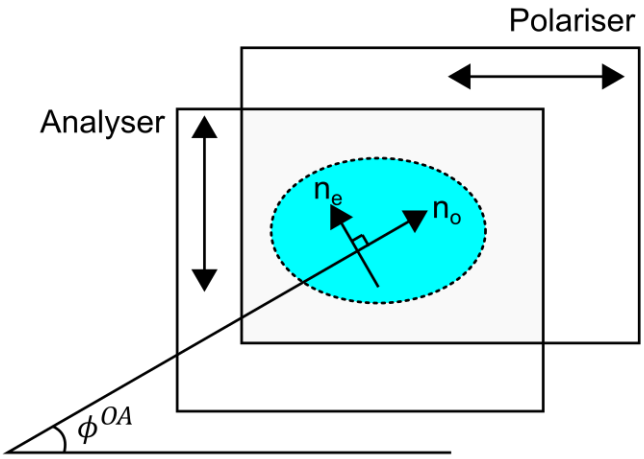

Fig. 2.4. Figurative representation of a birefringent material (with ordinary refractive index n_e, and extraordinary refractive index n_o. The optic axis of the material lies at an angle ϕ_{OA} to the vibration direction of the light leaving the polariser. Incident light is entering through the page, i.e. perpendicular to the optic axis of the material.

If the light incident on the sample is broadband illumination, we can use Eqn. 2.5 to find which wavelengths are subject to the full wave plate condition. These wavelengths are as shown in Table 2.2 below.

Order (m)	Wavelength	Part of Spectrum
1	1000 nm	Near infrared
2	500 nm	Green
3	333 nm	Ultraviolet

Table 2.2 Full wave plate condition for $\Gamma = 1000\ \mathrm{nm}$. Wavelengths fulfilling this condition will not be transmitted through the analyser, in this case, green light at 500 nm.

Any of these wavelengths will be subjected to the full wave plate condition will not be able to pass the analyser. In this case, green light at 500 nm is removed from the spectrum.

We can also consider the half wave plate condition (Eqn. 2.6).

Order (m)	Wavelength	Part of Spectrum
0	2000 nm	Infrared
1	666 nm	Red
3	400 nm	Violet
4	222 nm	Ultraviolet

Table 2.3 Half wave plate condition for $\Gamma = 1000\ \mathrm{nm}$. If the optic axis is at 45° to the polariser and analyser, the polarisation direction is rotated by 90°, therefore is transmitted through the analyser, at that specific wavelength. In this case, red and violet are transmitted.

For this example, the half wave plate condition will transmit red and violet light. Between those two conditions, one would expect a ‘pink’ colour to be visible through the analyser.

Strictly speaking, the full- and half-wave plate conditions only apply to an infinitely thin slice of the spectrum. Other wavelengths experience an intermediate amount of transmission through crossed polarisers. When performing polarising microscopy, birefringence colours can be matched with a ‘Michel-Levy chart’, a visual map where the birefringence colours have been calculated for.

2.2.8 Polarising Microscopy with Wave Plates

To extract more information about a birefringent sample, an additional full wave plate can be inserted between the crossed polarisers, either in front of or behind the sample. If the optical path length of the additional wave plate is known, more information about the orientation of the director can be attained.

For an example use a wave plate with $\Gamma = 530\ \mathrm{nm}$. Only the first order ($m = 1$) of the full wave plate condition is in the visible range, so this type of wave plate is called a ‘first order’ wave plate.

on a sample with $d_{med} = 10\ \mu m$ and $\Delta n = 0.2$ ($\Gamma = 2000\ \mathrm{nm}$). With no wave plate, the sample should appear green under crossed polarisers, if illuminated by white light. In Table 2.4, the same argument used in section 2.2.7 is used to determine the birefringence colour associate with the sample under crossed polarisers, with no additional wave plate.

	Full Wave Plate	Half Wave Plate
Orders in Visible	3, 4, 5	3, 4
Wavelengths (nm)	667, 500, 400	571, 444
Colours	Red, Green, Violet	Yellow, Violet
At Analyser	Not Transmitted	Fully Transmitted
Resulting Colour	Green	Green

Table 2.4. The same argument used to calculate the birefringence colours for $\Gamma = 1000\ \mathrm{nm}$ can be used for $\Gamma = 2000\ \mathrm{nm}$, using the wave plate conditions to predict which colours will be passed by the analyser, in this case, green. Only orders in the visible part of the spectrum are included.

Again, we can consider several possibilities. We will only consider the full wave plate condition for now, but the same argument holds for the half wave plate and intermediate conditions.

The first possibility is there is no sample between crossed polarisers, only the wave plate. The associated birefringence colour is pink, since from the full wave plate condition, 530 nm (green) is subtracted from the spectrum. The observed birefringence colour would also be pink is any of the cases a), b) and c) seen in Table 2.1 apply for the sample, e.g. the optic axis of the sample material is parallel to the polariser or the analyser.

A second possibility is that the optic axis (or 'fast axis') of the 530 nm wave plate (usually denoted by γ) is parallel to the optic axis of the birefringent material. The optical path differences add together to make $\Gamma = 2530\ \mathrm{nm}$. A third possibility is the optic axis of the 530 nm wave plate is perpendicular to the optic axis of the material, in which case, the optical path differences are

subtracted: $\Gamma = 1470\ \mathrm{nm}$. The resulting birefringence colours for those two cases are calculated in Table 2.5 below. Only the half wave plate condition has been used to calculate these values, but a similar argument can also be made for the full wave plate condition.

Optic axis of Lambda plate	Parallel to optic axis of material	Perpendicular to optic axis of material
	Additive	Subtractive
Optical Path Length	$\Gamma = 2530\ \mathrm{nm}$	$\Gamma = 1470\ \mathrm{nm}$
Orders in visible	3, 4	2, 3
Wavelengths (nm)	723, 562, 460	588, 420
Colours	Deep Red, Yellow, Blue	Yellow, Violet
Resulting Colour	Yellow	Blue

Table 2.5. The birefringence colours associated with a birefringent sample with $\Gamma = 2000\ \mathrm{nm}$, with a lambda plate as determined by the half wave plate condition.

The resulting birefringence colours are yellow when the optic axis of the waveplate is parallel to the optic axis of the sample material, and blue when the optic axis of the waveplate is parallel to the optic axis of the sample material. In conventional polarising microscopy, due to symmetry, it is not possible to. As illustrated in Fig. 2.5, the technique of using an additional wave plate can distinguish different orientations of the optic axis in the

sample, that would appear identical under conventional polarising microscopy.

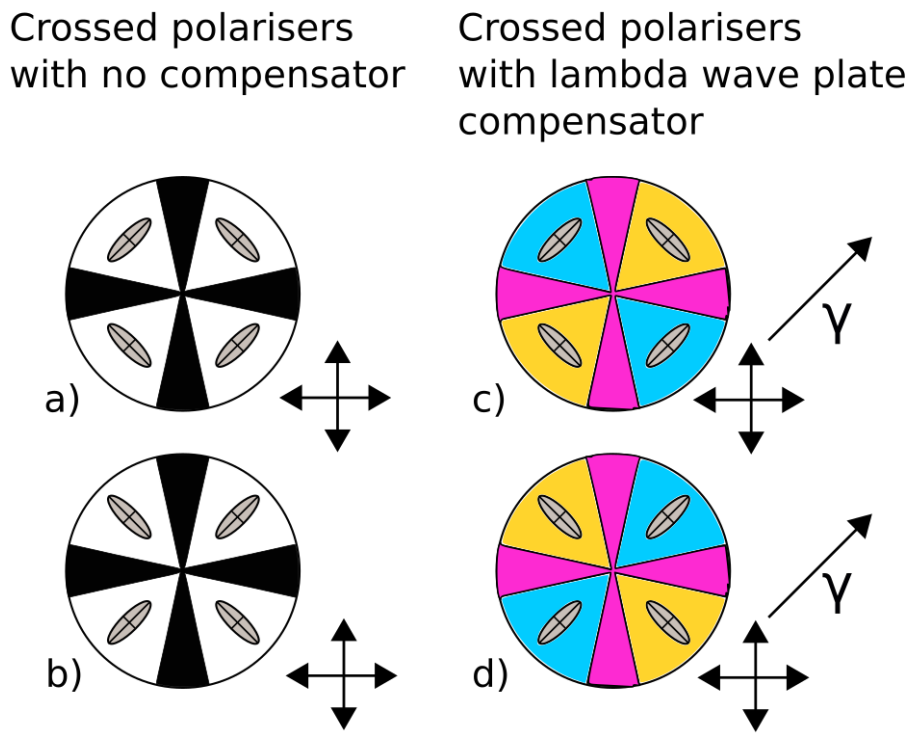

Fig. 2.5. Representation of what would be seen under crossed polarisers without (a), b)) and with (c), d) and additional wave plate, with a sample containing a birefringent substance with different orientations (cross sections of refractive index ellipsoid). The birefringence colours observed with the additional wave plate can distinguish when the optic axis is at +45° or -45° to the analyser, which is not possible from a static image in polarising microscopy.

Using additional wave plates is a powerful tool in understanding the orientation of the optic axis of a material, which will be used later on in this thesis.

2.3 Liquid Crystals

Early in people's education, many are taught the 'three states of matter', solids, liquids and gases. In fact, that is a simplified picture: depending on classification, there are many hundreds of distinctive states. Many states of matter exist only at extremely low or high temperatures, or only in combinations of different materials, or only occur with molecules that have a particular shape or symmetry. One family of phases is known as the 'liquid crystals'. With a long history dating back as far as the late 19th century [3], liquid crystal phases are considered intermediate between highly ordered crystalline phases, and disordered liquid (or 'isotropic') phases. A diagram comparing these phases can be seen in Fig. 2.6 below.

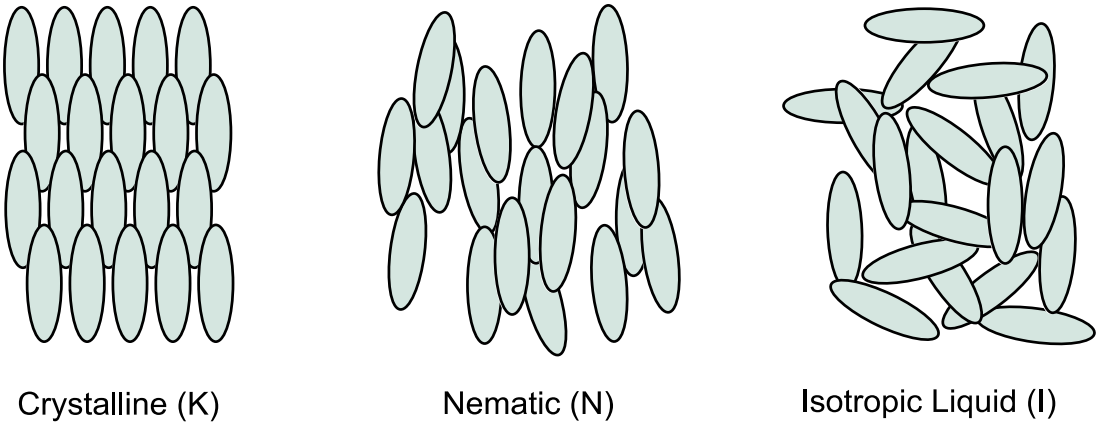

Fig. 2.6. A schematic of the same rod-like molecules forming crystalline, nematic liquid crystal (see section 2.3.1) and isotropic phases, with increasing temperature implied from left to right. In some materials there is more than one liquid crystalline 'mesophase' between the crystalline and isotropic phases.

Liquid crystals can be divided into two categories, the 'thermotropic' liquid crystals, which have phase behaviour that depends on temperature, and the 'lyotropic' liquid crystals, where the phase depends on the concentration of a solvent. All the experiments in this project study thermotropic phases.

2.3.1 Nematic Liquid Crystals

Within the thermotropic phases, the 'nematic' liquid crystal mesophase has the highest symmetry, and is the best understood. Many textbooks give a lot of detail on the manufacture, theory, and physical properties of nematic LCs [4–6], but this section aims only to summarise some of the most important physical properties of nematic liquid crystals in the context of devices and liquid crystal colloids. Some types of molecules that form nematic phases appear to have cylindrical symmetry due to the molecules' rapid rotations around the long axis. For this reason, such molecules are often represented as rod-shaped, or in the liquid crystal terminology, 'calamitic'. Other symmetries of molecule sometimes form nematic phases, for example, bent-core [7,8] and discotic liquid crystals [9,10]. Nematic materials have orientational order, as the molecules' axis of symmetry is not randomly distributed, but nematics do not have positional order, as the molecules' centres of mass are randomly distributed (as in an isotropic liquid).

2.3.2 The Director

The 'director' is a unit vector that defines the average direction of the molecules' axes of symmetry, and by convention is represented by $\boldsymbol{n}$. In nematic liquid crystals, the condition of a non-polar fluid means that the direction is degenerate so that $\boldsymbol{n} = -\boldsymbol{n}$**.** In diagrams, the director is represented either by an arrow, or continuous lines similar to field lines.

2.3.3 Order Parameter[5]

One important measure in liquid crystals is the orientational order parameter, S. A liquid crystal's physical properties are highly dependent on this parameter. This parameter is usually defined as:

$$S = \frac{1}{2}\langle 3\cos^2\theta - 1\rangle, \qquad \text{Eqn. 2.7}$$

where θ is the angle of each molecule with respect to the director. The angular brackets represent a statistical average. The order parameter is

zero for complete disorder (e.g. in an isotropic liquid), and 1 for complete order, which is the case in a crystal [5].

2.3.4 Viscosity

In liquid crystals, viscosity is not the same in all directions. In the most formal description (Eriksen-Leslie theory) viscosity is quantified by four independent 'Leslie coefficients' [11,12] (or Leslie viscosities). Often in practice, systems are characterised by the three 'Miesowicz viscosities' [13,14], as well as rotational viscosity.

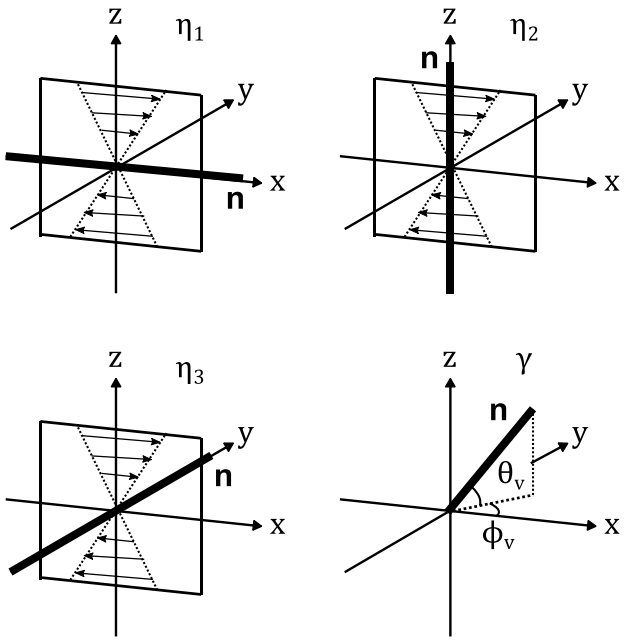

Fig. 2.7. Illustrations of the three Miesowicz viscosities (representing shear in different planes with respect to the director) η_1, η_2, and η_3, as well as rotational viscosity, γ.

2.3.5 Elastic Constants

One of the characteristics that depends on order parameter are the 'elastic constants'. These are known as the Frank or Frank-Oseen elastic constants, as they were first defined by Oseen [15] but expanded upon by Frank [16]. They represent the energy cost by deforming the director along a given axis. In uniaxial nematic liquid crystals, the elastic constants are splay (K_{11}), twist (K_{22}) and bend (K_{33}). There is also a saddle-splay term (K_{24}), but this only applies in certain geometries such as near surfaces or under certain symmetries. Representations of these deformations can be seen in Fig. 2.8 below.

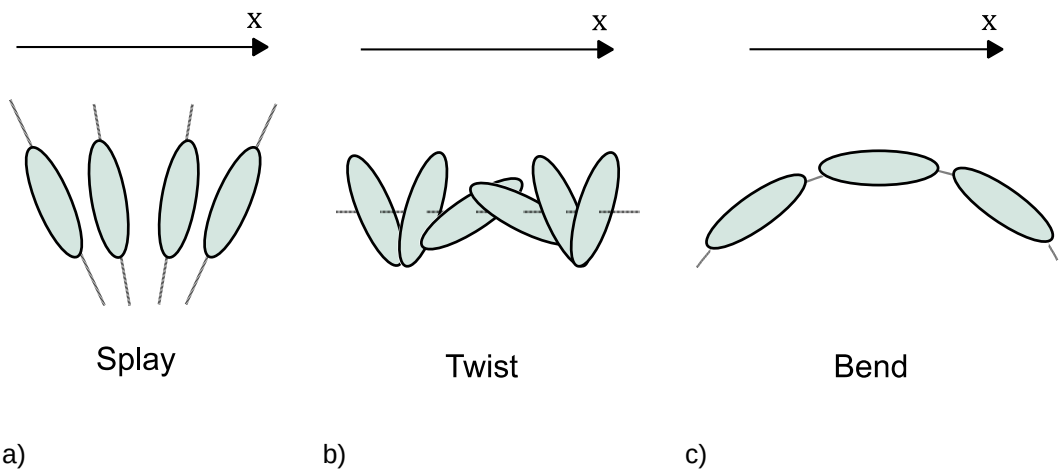

a) b) c)

Fig. 2.8. Deformations associated with Elastic constants in a liquid crystal for splay (a) twist (b) and bend (c).

The total free energy per unit volume, F_d is given by:

$$F_d = \frac{1}{2}K_{11}(\nabla \cdot \mathbf{n})^2 + \frac{1}{2}K_{22}(\mathbf{n} \cdot \nabla \times \mathbf{n})^2 + \frac{1}{2}K_{33}((\mathbf{n} \cdot \nabla) \cdot \mathbf{n})^2. \quad \text{Eqn. 2.8}$$

2.3.6 Anchoring Conditions[17]

At the interface between a LC and the surface of another material, the director can be in a number of different orientations depending on the interaction between the liquid crystal and the surface. If the director is lying in a plane parallel to the boundary, it is known as 'planar' or 'homogeneous' (HG) anchoring. If the director is perpendicular to the boundary, it is known as 'homeotropic' (HT) anchoring.

More generally, the anchoring can be defined as the angle between the director and the plane of the substrate (the polar angle θ^{anc}, sometimes known as 'pretilt') and the azimuthal angle, parallel to the plane of the substrate ϕ^{anc}. The angles θ^{anc} and ϕ^{anc} are visualised in Fig. 2.9.

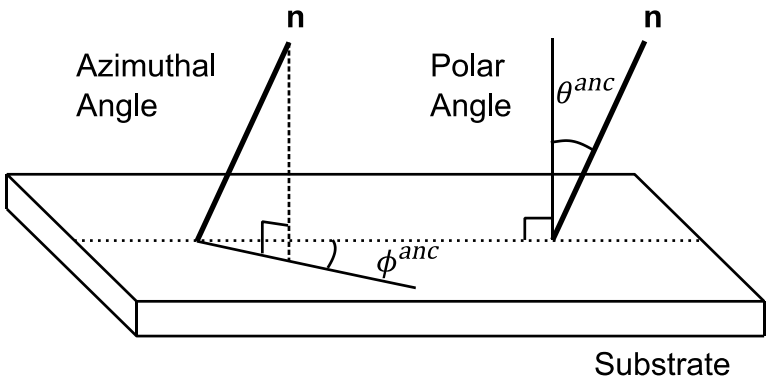

Fig. 2.9. Diagram showing how the director n at a surface is defined with the azimuthal angle, ϕ^{anc}, and pretilt θ^{anc}.

Typically, alignment with $\theta^{anc} < 7°$ is considered planar, and $\theta^{anc} > 85°$ is considered homeotropic. The 'anchoring energy' W, or energy cost associated with deforming a nematic director away from its 'ideal' anchoring at θ_0^{anc} and ϕ_0^{anc} is often described by:

$$W = W_0 + W_\theta \sin^2(\theta^{anc} - \theta_0^{anc}) + W_\phi \theta \sin^2(\phi^{anc} - \phi_0^{anc}) \quad \text{Eqn. 2.9}$$

first suggested by Rapini and Papoular [18].

2.3.7 Freedericks Transition

Many nematic materials have large dipole moments associated with their molecules and further dipoles are induced in the presence of an electric field. There is a free energy cost associated with the molecules' orientation with respect to the electric field:

$$F_E = -\frac{1}{2}\varepsilon_0 . \Delta\varepsilon(\mathbf{n} \cdot \mathbf{E})^2 \quad \text{Eqn. 2.10}$$

Therefore, the molecules may re-orient in order to reduce the free energy under an electric field. Taking into consideration the energy cost associated with elastic deformation (Eqn. 2.8), the director will only be distorted if the voltage exceeds the threshold voltage, V_{thr}:

$$V_{thr} = \pi \sqrt{\frac{K}{\varepsilon_0 \Delta\varepsilon}}, \qquad \text{Eqn. 2.11}$$

where K corresponds to the elastic constants in a particular geometry. in the case of a planar device, $K = K_{11}$. The change in state is known as the Freedericks transition [19].

2.3.8 Liquid Crystal Displays

LCDs are based on a sandwich-like construction, known as a 'cell'. A cell consists of two planes of glass separated by a spacer, usually monodisperse glass beads. The inner surfaces of the glass are treated with a conductive layer, and a layer to promote alignment. The cell gap is filled with liquid crystal, and any exposed edges are sealed with glue.

While there are many possible geometries used in liquid crystal displays commercially [20], liquid crystals research often begins with a very simple geometry, the planar cell, as shown in Fig. 2.10 below. With no electric field, the alignment of the liquid crystal is uniformly planar throughout the cell. Applying a voltage of sufficient strength (see section 2.3.7) re-orients molecules in the bulk of the liquid crystal.

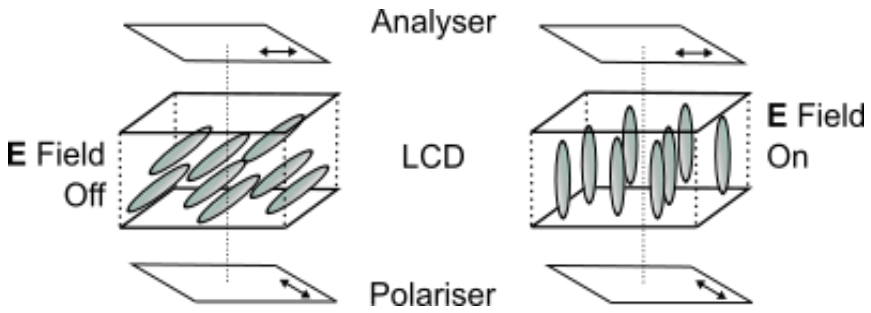

Fig. 2.10. A simple, planar liquid crystal display. The arrows represent the polarising axes of the polarisers, which are at 90° to each other. The orientation of the liquid crystal molecules in the bulk of the cell changes if the voltage applied is strong enough to cause a Freedericks transition. As a note on the scale of this diagram, molecular size is typically ~4nm, a cell gap of ~5-10µm, and the glass substrates ~1mm thick.

By changing the orientation of the liquid crystals, the birefringence of the cell (and therefore phase difference of light passing through it) can be changed. In general, the variation of birefringence with electric field is known as

'electrically controlled birefringence', discussed with some very early liquid crystal devices in 1972 and 1973 [21,22]. When placed between crossed polarisers, devices can be designed where the E field on appear dark to an observer, and E field off states appear bright. For a planar display similar to that in Fig. 2.10, the transmitted intensity due to the crossed polarisers I_t is given by:

$$I_t = I_0 \sin^2(2\theta^{ave}) \sin^2(\delta/2), \qquad \text{Eqn. 2.12}$$

where I_0 is the intensity of incident light, θ^{ave} is the angle between the average director and the normal to the substrate, and $\delta = 2\pi\Gamma = 2\pi\Delta nd$.

2.3.9 Defects in Liquid Crystals [23,24]

The concept of 'defects' in a material may be recognised by those familiar with solid state physics. Defects appear in crystalline materials as point defects, line defects, and plane defects (page 58-64 [25]), representing breaks or 'discontinuities' in the order and uniformity of a system.

Since liquid crystals are ordered, they can also support defects. In nematic LCs, the two possible types are 'point defects' (one dimensional) and 'line defects' (two dimensional). These types were identified and classified very early on in the history of liquid crystals [15,26].

The conventional way of classifying line defects is by 'winding number' s, as shown in Fig. 2.11 below.

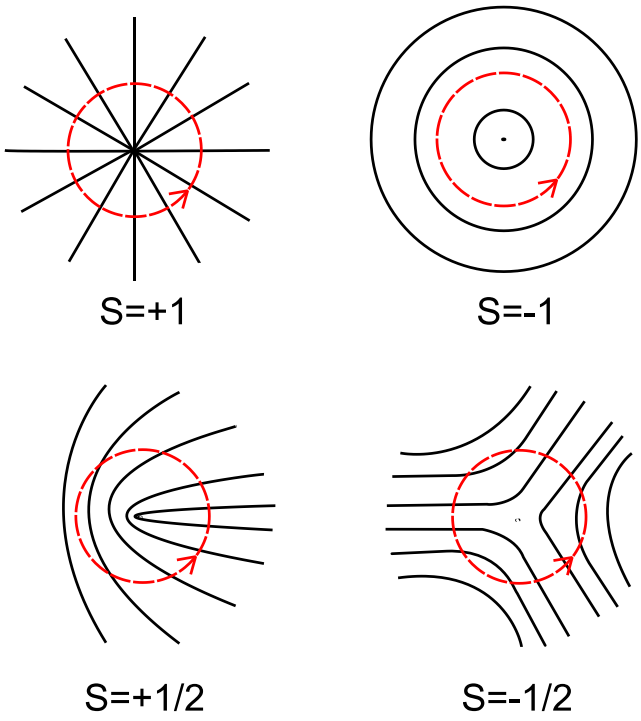

Fig. 2.11. Classification of defect types by winding number (the 'line' would extend into and out of the page). Winding number is calculated by drawing a loop around the defect core, and counting the number of times the director rotates (going counter-clockwise). Only half integer or integer values of winding number are allowed. Based on a diagram from [24].

For point defects, one can define 'topological charge' Q. Similar to charge in electromagnetism, Q measures how many times the director wraps around a unit sphere (page 402, [23]). Due to the symmetry of the director in nematics, $Q = 1$ and $Q = -1$ are always equivalent: by convention, the positive value is used.

The energy E_{LD} of a disclination or point defect is not simple to calculate. A common approximation is to assume the elastic constants to be equal ($K_{11} = K_{22} = K_{33} = K$) and the line disclination has length L:

$$\frac{E_{LD}}{L} = \pi K s^2 l \qquad \text{Eqn. 2.13}$$

and l depends on a number of qualities such as elastic constants, but increases only logarithmically [24].

Defects may appear in liquid crystals when there is a mismatch between anchoring conditions, as will be seen in section 2.5.1.

2.4 Colloids[24, 27]

A colloid is defined as a substance consisting of solid particles dispersed in a liquid medium. The particles are usually ~10 μm in diameter or smaller. Some aspects of colloids that have been considered in the work in this thesis are the associated fluid dynamics, behaviour in an electric field, stability, and Brownian motion.

2.4.1 Stokes' Law

For particles on a colloidal scale (~10 μm or smaller), one can assume a low Reynolds number regime (i.e. viscosity dominates over inertial effects). Stokes' law states that in this regime, a spherical particle with radius a moving at velocity v experiences force F equal to:

$$F = 6\pi\eta a v \qquad \text{Eqn. 2.14}$$

where η is the viscosity of the liquid.

2.4.2 Electrophoresis

It has been observed widely in the literature, that charged particles can be transported under a uniform electric field. By definition, any charged particle experiences a force under an electric field. In a viscous medium, colloidal particles typically reach a drift velocity $\boldsymbol{v}_{drift}$ at equilibrium, which depends on the electric field strength. The electrostatic force must be balanced against any viscous effects of the medium, as governed by (Eqn. 2.19). Electrophoresis is often characterised by the electrophoretic mobility, U_E:

$$\boldsymbol{v}_{drift} = U_E \boldsymbol{E}_{eph}. \qquad \text{Eqn. 2.15}$$

2.4.3 Stability and Inter-Colloid Forces

An important aspect of colloidal systems is stability. In other words, do all the attractive and repulsive forces in the system result in particles that have a high enough energy barrier to be 'thermally stable', or do the particles aggregate? Depending on the materials, significant forces may include Van Der Waals, steric forces, and more Coulomb-like electromagnetic interactions.

2.4.4 The Electrical Double Layer and the Zeta Potential

To understand electrostatic interactions in a colloidal system, not only the charge of the material of the particle must be considered, but also the distribution of any ions in the surrounding medium. Counterions attracted to the surface of the particle form a distribution known as the 'electrical double layer'. Assuming that the counterions balance the charge on the particle exactly, and the potential is small (the Debye-Hückel approximation), the potential at ψ distance r from the surface of the particle can be approximated as:

$$\psi(r) = \psi_0 \exp(-\kappa_{DL} r), \qquad \text{Eqn. 2.16}$$

where ψ_0 is the potential at the particle surface ($r = 0$). The constant κ_{DL} is related to a characteristic length scale, the 'Debye screening length' (κ_{DL}^{-1}), which is given by:

$$\kappa_{DL} = \left(\frac{2\times10^3 N_A e^2 I_{ion}}{\varepsilon\varepsilon_0 k_B T}\right)^{\frac{1}{2}}, \quad \text{Eqn. 2.17}$$

where N_A is Avogadro's number, and I_{ion} is the 'molar ionic strength'. Molar ionic strength is given by:

$$I_{ion} = \sum_{ion=1}^{all\ ions} c_{ion} z_{ion}^2 \quad \text{Eqn. 2.18}$$

where c_{ion} is the molar concentration of each individual type of ion (mol/L), and z_{ion} is the charge number of each type of ion.

When measuring the charge of a particle on a macroscopic scale, the surface charge is often measured at the slipping plane (or shear surface) of the particle. The slipping plane is defined as the envelope where shear appears in the fluid adjacent to a rigid body when the fluid and solid are in relative motion. The potential at the slipping plane is known as the 'zeta potential' (Fig. 2.12).

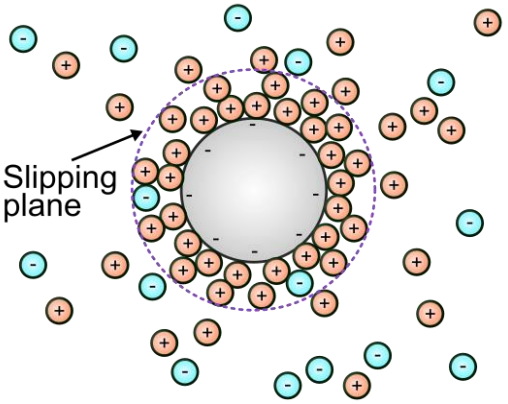

Fig. 2.12. Schematic representing a particle (grey, centre) suspended in a medium with positive and negative ions. Due to the positive surface charge on the particle, an electrical double layer is formed. The Zeta potential is the electric potential measured at the slipping plane (dotted line).

If the particle size is sufficiently large compared to the thickness of electrical double layer, the Smoluchowski approximation applies. In this case, the electrophoretic mobility (Eqn. 2.15) is given by:

$$U_E = \frac{2\varepsilon_m \zeta}{} \qquad \text{Eqn. 2.19}$$

where ε_m is the dielectric constant of the medium.

As a larger zeta potential represents a larger barrier between particles, larger zeta potentials represent higher stability [28,29]. Zeta potentials alone cannot completely predict a system's stability; for example, the zeta potential does not account for attractive Van der Waals forces between particles [30]. Nevertheless, the zeta potential is often a useful measure of stability. Stability is sometimes related approximately to the zeta potential by the following boundaries: ± 10 mV, ± 10 – 20 mV, ± 20 – 30 mV and > ± 30 mV (very unstable, moderately unstable, moderately stable, and highly stable respectively).

2.4.5 Brownian motion

A particle going on a 'random walk' has an equal chance of moving the same distance in any direction in a unit time. Whereas the mean of the displacement vector $\boldsymbol{R}$ must be zero, the mean of the square of the displacement vector (i.e. the 'mean square displacement' (MSD) $\langle \boldsymbol{R}^2 \rangle$) is linearly proportional to time:

$$\langle (\boldsymbol{R}(t))^2 \rangle \propto t. \qquad \textbf{Eqn. 2.20}$$

The equation of motion of the particle can be written as:

$$m_p \frac{d^2\boldsymbol{R}}{dt^2} + \xi \frac{d\boldsymbol{R}}{dt} = F_{random} \qquad \text{Eqn. 2.21}$$

where m_p is the mass of the particle, ξ is the drag coefficient. From Eqn. 2.14, the drag coefficient is equal to:

$$\xi = 6\pi\eta a. \qquad \text{Eqn. 2.22}$$

It can be shown (e.g. page 51-52 of Jones [24]) that in thermal equilibrium, the solution to Eqn. 2.21 is:

$$\langle (\boldsymbol{R}(t))^2 \rangle = \frac{6k_B T}{\xi} t. \qquad \text{Eqn. 2.23}$$

Alternatively, Eqn. 2.22 can be written as:

$$\langle (\boldsymbol{R}(t))^2 \rangle = 6Dt \qquad \text{Eqn. 2.24}$$

where the constant D is the 'diffusion coefficient'. By substituting Eqn. 2.22, we find that for a spherical particle:

$$D_{sphere} = \frac{k_B T}{6\pi\eta a}. \qquad \text{Eqn. 2.25}$$

This is known as the 'Stokes-Einstein' equation.

A particle undergoing this type of movement is said to be undergoing 'Brownian motion', named after Brown who first observed Brownian motion of pollen grains in 1827 [31].

2.5 Liquid Crystal Colloids

Liquid crystal colloids are unusual among colloidal systems since the medium is anisotropic. The anisotropy and strong elastic forces have some perhaps unexpected properties, such as the topological defects associated with the particles. There is much theoretical interest in liquid crystal colloids: for instance, some of the only known physical manifestations of mathematical topology [32]. For wider information on this topic, see for example, Stark [23] or Alexander et al [33]. Here we shall focus on some fundamental concepts: satellite defects, and forces occurring with liquid crystal colloids.

2.5.1 Defects associated with Particles

Consider a spherical particle with homeotropic anchoring conditions. The particle acts, effectively, as the centre of a radial defect. This presents a problem if the particle is placed in a liquid crystal that is uniformly aligned. It seems impossible for both conditions to occur at the same time: due to the uniform alignment conditions at infinity, the total charge must be zero. But the radial defect has a charge $Q = \pm 1$.

If the anchoring is weak enough, the anchoring on the particle will break. This is known as the ‘weak anchoring’ condition, shown in Fig. 2.13 below. In the weak anchoring condition, the total charge is equal to zero. By analogy with Gauss’ law in electrostatics, at a long distance from the particle, the ‘divergence’ of the director would be equal to zero, as if no particle were present.

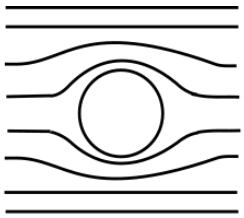

Weak Anchoring

Fig. 2.13. Weak anchoring condition: anchoring breaks in order to make the total charge zero. At a distance, the director is not affected by the presence of the particle.

The other option is to create a second defect which also has a charge of $Q = \pm 1$. This can either be a satellite 'hyperbolic hedgehog' defect, or an encircling 'Saturn ring' defect, as shown in Fig. 2.14 below. The Saturn ring is a ±½ line defect which can be shown to also be equivalent to $Q = \pm 1$.

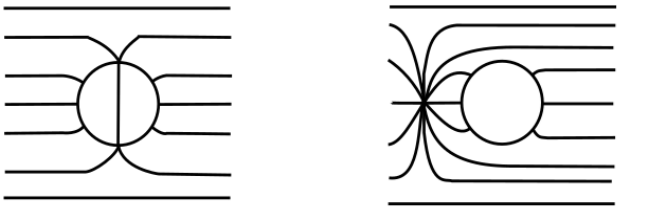

Saturn Ring Hyperbolic Hedgehog

Fig. 2.14. Saturn ring (SR) and hyperbolic hedgehog (HH). Note that the SR has higher energy than the HH (since energy of defect is proportional to unit length (Eqn. 2.13)) so SR are unstable.

Another 'mismatch' occurs with particles that have homogeneous anchoring conditions. The situation is resolved by creating two defects on the surface of the particle by two ±1 defects (since the director is symmetrical, this 'adds' to zero).

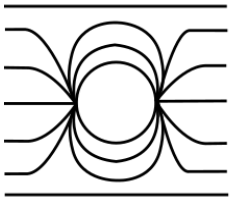

Boojums

Fig. 2.15. Boojums occur at the poles of a particle with homogeneous alignment.

The Boojum case is a physical manifestation of the mathematical theorem also known as ‘hairy ball theorem’ [34].

For non-spherical particles, the position, and even number of defects associated with the particles depends strongly on the shape of the particle. Designing and manufacturing particles specifically for liquid crystal colloid research is a common topic of research. A non-exhaustive list of particle shapes investigated includes: rings [35], spirals [36], knots [37], and particles that can only be described as ‘Tetris-like’ [38].

Despite the breadth of possible designs, some themes do seem to be common. It is found that defects often form at sharp edges of a particle. Using a cube-shaped particle an example, the formation of defects at edges is discussed from a simulation perspective by Hung and Bale [39]. The topic was expanded upon by Beller et al [40] who show the placement of defects for particles intermediate between spheres and cubes, as well as rod-shaped and ellipsoidal particles.

While most research in this thesis is focused on the best-understood system of spherical particles, the topic of non-spherical particles in liquid crystals will be returned to in chapters 7 and 8.

2.5.2 Particle motion in an Electric Field

Understanding the behaviour of an LC colloid in an electric field is a complex problem. As well as electrical properties common to colloidal systems [41], the complexity of the physics is increased. For example, there is also the

Freedericks transition to consider, and in some cases, defects associated with the particles. Depending on the system, particles can move both parallel to and perpendicular to the applied electric field. While a summary of this is given for the purposes of this thesis, the topic is reviewed in detail by Lavrentovich [42], and studied in depth by Oh [43], both 2014.

2.5.3 Translational Motion: Electrophoresis

In an anisotropic medium such as a liquid crystal, electrophoretic motion can differ in several ways from electrophoresis in an isotropic medium.

Lavrentovich, Lazo and Pishnyak in 2010 [44] found a quadratic dependence of velocity on electric field strength for metal and dielectric spheres suspended in a liquid crystal:

$$v_{drift} = c_1 E_{eph} + c_2 E_{eph}^2. \qquad \text{Eqn. 2.26}$$

where c_1 and c_2 are constants, corresponding to electrophoretic mobility in different orders. The quadratic dependence was found to arise due to the asymmetry of the liquid crystal surrounding the particle due to satellite defects. As well as second order, third order ($\propto E_{eph}^3$) electric field dependence has been observed in liquid crystal colloids [45].

Other unusual electrophoretic behaviour in liquid crystal includes migration of particles in a direction perpendicular to the electric field [46], as opposed to parallel to the electric field.

2.5.4 Rotational motion: Quincke Rotation

Quincke rotation [47,48] (a rotation of a particle due to an unstable accumulation of charge on the surface anti-parallel to the electric field) was first observed in liquid crystals by Liao et al in 2005 [49]. As well as simple spherical particles, cylindrically symmetric particles can also undergo Quincke rotation. Based on theory by Feng 2002 [50], rotation rate ω depends on electric field strength E:

$$\omega(E) = \frac{1}{\eta}\frac{E_r^2 \varepsilon_s \varepsilon_0}{(1 + \varepsilon_s/\varepsilon_{lc})}\sqrt{\frac{E^2}{E_r^2} - 1} \qquad \text{Eqn. 2.27}$$

Where η is bulk viscosity (an approximation of the viscosities in section 2.3.4) of the LC, ε_s is the dielectric constant for the sphere, ε_{lc} is the dielectric constant for the LC. E_r is the threshold electric field and also depends on η, ε_s and ε_{lc}, but also the conductivities of the sphere and the liquid crystal.

2.6 Summary

This chapter has introduced some important characteristics of the systems involved in liquid crystal colloids. We considered the optics of birefringent media; as liquid crystals are often highly birefringent, many techniques to determine liquid crystals' characteristics depend on birefringence: chiefly, polarising microscopy, which will be used widely in this thesis. Some elementary physics of liquid crystals, especially nematic liquid crystals, were introduced: the order parameter, elastic constants and anchoring conditions, all of which will be important parameters in this thesis. Introducing the topic of colloids discussed Brownian motion, which will form the principle behind the measurement techniques in chapters 5 to 6. Finally, the combined system, liquid crystal colloids was introduced. It was seen that defects can be associated with particles when suspended in a liquid crystal, and that the types of defect depend on particle shape, size, and anchoring conditions.

Everything that has been introduced in this chapter will be vital to our understanding of the liquid crystal colloid systems studied in the results chapters, chapters 4-7. Understanding the bulk properties of liquid crystals will inform how these are measured in chapter 4. Understanding Brownian motion will be important in the particle tracking experiments in chapters 5-6. Considering the optics of liquid crystals under crossed polarisers will form the basis for our method of studying the alignment of liquid crystals in chapter 7. Finally, knowing which parameters are important in liquid crystal colloids has given us a framework to study a system building towards the devices discussed in chapter 1.

References

1. E. Hecht, *Optics*, 4th Ed. (Addison Wesley, 2002).

2. R. H. Chen, *Liquid Crystal Displays: Fundamental Physics and Technology* (Wiley, 2011).

3. S. T. Lagerwall, Liquid Crystals **40**, 1698 (2013).

4. J. W. Goodby, P. J. Collings, T. Kato, C. Tschierske, H. F. Gleeson, and P. Raynes, editors , *Handbook of Liquid Crystals, Volume 3: Nematic and Chiral Nematic Liquid Crystals* (Wiley, 2014).

5. P.-G. De Gennes, *The Physics of Liquid Crystals* (Oxford University Press, 1974).

6. S. Singh, in *Liquid Crystals: Fundamentals* (World Scientific Publishing, 2002).

7. D. J. Photinos, in *Handbook of Liquid Crystals, Volume 3: Nematic and Chiral Nematic Liquid Crystals*, 2nd ed. (Wiley, 2014).

8. F. Yang and J. R. Sambles, in *Handbook of Liquid Crystals, Volume 3: Nematic and Chiral Nematic Liquid Crystals*, 2nd ed. (Wiley, 2014).

9. A. N. Cammidge and H. Gopee, in *Handbook of Liquid Crystals, Volume 3: Nematic and Chiral Nematic Liquid Crystals*, edited by J. W. Goodby, P. J. Collings, T. Kato, C. Tschierske, H. F. Gleeson, and P. Raynes, 2nd ed. (Wiley, 2014).

10. R. J. Bushby and N. Boden, in *Handbook of Liquid Crystals, Volume 3: Nematic and Chiral Nematic Liquid Crystals*, 2nd ed. (Wiley, 2014).

11. F. M. Leslie, The Quarterly Journal of Mechanics and Applied Mathematics **19**, 357 (1966).

12. Parodi, O., J. Phys. France **31**, 581 (1970).

13. M. Miesowicz, Nature **158**, 27 (1946).

14. M. Miesowicz, Molecular Crystals and Liquid Crystals **97**, 1 (1983).

15. C. W. Oseen, Transactions of the Faraday Society **29**, 883 (1933).

16. F. C. Frank, Discussions of the Faraday Society **25**, 19 (1958).

17. B. Broughton, in *Handbook of Liquid Crystals, Volume 2: Physical Properties and Phase Behaviour of Liquid Crystals*, 2nd Ed. (Wiley, 2013).

18. A. Rapini and M. Papoular, J. Phys. (Paris), Colloq. **30**, C4 (1969).

19. V. Fréedericksz and A. Repiewa, Zeitschrift Für Physik **42**, 532 (1927).

20. *Handbook of Liquid Crystals, Volume 8: Applications of Liquid Crystals*, 2nd ed. (Wiley, 2014).

21. R. A. Soref and M. J. Rafuse, Journal of Applied Physics **43**, 2029 (1972).

22. G. Labrunie and J. Robert, Journal of Applied Physics **44**, 4869 (1973).

23. H. Stark, Physics Reports **351**, 387 (2001).

24. R. A. L. Jones, *Soft Condensed Matter* (Oxford University Press, 2002).

25. M. N. Rudden and J. Wilson, *Elements of Solid State Physics*, 2nd Ed. (Wiley, 1993).

26. Friedel, G., Ann. Phys. **9**, 273 (1922).

27. I. D. Morrison and S. Ross, *Colloidal Dispersions* (Wiley, 2002).

28. H. Eilers and J. Korff, Transactions of the Faraday Society **35**, 707 (1939).

29. B. Derjaguin, Transactions of the Faraday Society **35**, 203 (1939).

30. S. Bhattacharjee, Journal of Controlled Release **235**, 337 (2016).

31. R. Brown, The Philosophical Magazine **4**, 161 (1828).

32. B. I. Senyuk, Q. Liu, S. He, R. D. Kamien, R. B. Kusner, T. C. Lubensky, and I. I. Smalyukh, Nature **493**, 200 (2013).

33. G. P. Alexander, B. G. Chen, E. A. Matsumoto, and R. D. Kamien, Reviews of Modern Physics **84**, 497 (2012).

34. J. Milnor, The American Mathematical Monthly **85**, 521 (1978).

35. B. I. Senyuk, Q. Liu, Y. Yuan, and I. I. Smalyukh, Physical Review E **93**, 062704 (2016).

36. B. I. Senyuk, M. B. Pandey, Q. Liu, M. Tasinkevych, and I. I. Smalyukh, Soft Matter 34 (2015).

37. A. Martinez, M. Ravnik, B. Lucero, R. Visvanathan, S. Žumer, and I. I. Smalyukh, Nature Materials **13**, 258 (2014).

38. A. Martinez, T. Lee, T. Asavei, H. Rubinsztein-Dunlop, and I. I. Smalyukh, Soft Matter **8**, 2432 (2012).

39. F. R. Hung and S. Bale, Molecular Simulation **35**, 822 (2009).

40. D. A. Beller, M. A. Gharbi, and I. B. Liu, Soft Matter **11**, 10 (2014).

41. T. B. Jones, IEE Engineering in Medicine and Biology Magazine 33 (2003).

42. O. D. Lavrentovich, Soft Matter **10**, 1264 (2014).

43. J. Oh, Unusual Particle Motions in the Liquid Crystal Phases, University of Manchester, 2014.

44. O. D. Lavrentovich, I. Lazo, and O. P. Pishnyak, Nature **467**, 947 (2010).

45. 1. A. V. Ryzhkova, F. V. Podgornov, and W. Haase, Applied Physics Letters **96**, 151901 (2010).

46. 1. I. Dierking, G. Biddulph, and K. Matthews, Physical Review E **73**, 011702 (2006).

47. G. Quincke, Annalen Der Physik **295**, 417 (1896).

48. T. B. Jones, IEEE Transactions on Industry Applications **IA**-**20**, 845 (1984).

49. G. Liao, I. I. Smalyukh, J. R. Kelly, O. D. Lavrentovich, and A. Jákli, Physical Review E **72**, 1 (2005).

50. J. Q. Feng, Journal of Colloid and Interface Science **246**, 112 (2002).

Chapter 3 Experimental Methods

3.1 Introduction

To investigate liquid crystal colloids, several experimental techniques were selected. Information on these techniques, including any details of the setup as used during the project, can be found in this chapter. Methods specific to only a single chapter will be discussed in those chapters only. The first part of the chapter describes the methods for manufacturing a typical sample, and briefly describes the polarising microscope. A large part of this chapter is devoted to the laser tweezing apparatus and particle tracking systems. The layout and operation of the microscope, the laser, and any optical components between the laser, sample, and cameras are recorded here. As well as the equipment specification, the theory and applications of optical trapping systems will be outlined, especially with regards to dielectric particles with diameters much larger than the wavelength of the trapping laser. Limitations of the tracking system must be taken into account when considering results in later chapters.

Using the methods in this chapter, in chapters 5 and 6 we will perform an extensive investigation into the confinement of particles at defects in a liquid crystals for the first time using passive methods. Methods of manufacturing samples will also be used in chapters 4 and 7.

3.2 Cell manufacture and construction

Standard samples were constructed as a liquid crystal ‘cell’ consisting of two substrates separated by a spacer, and the liquid crystal and particle mixture in between (see Fig. 3.1). Any created otherwise, or with variations on these methods, will be discussed separately.

A typical sample was made to the specifications below:

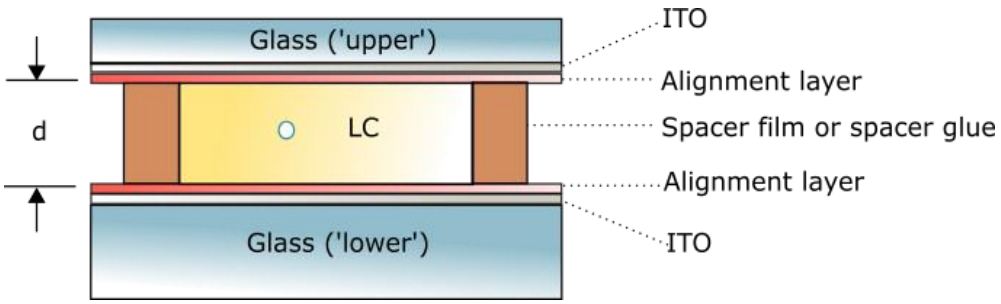

Fig. 3.1. Diagram showing cross-section of typical sample, and cell gap d. Note that ITO and alignment layers were not used in all samples.

The type of substrate used depended on the type of tweezing technique, as shown in Table 3.1 below.

Techniques Applied to Sample	'Upper' substrate	'Lower' substrate
Local melting method	#1 cover slip, standard	ITO glass
Active tweezing method	#1 cover slip, standard	Non-ITO glass
No E field applied	#1 cover slip, standard	Non-ITO glass
E field applied	#1 cover slip, ITO treated	ITO glass

Table 3.1. Types of glass used for substrates depend on the experiment conducted.

In some cases the glass substrates were treated with an alignment layer, as discussed in section 3.2.2 below.

3.2.1 Cutting and cleaning of glass substrates

All glass was pre-prepared and cleaned before use in samples. To separate glass into the appropriate sized pieces, glass was scored with a carbide glass scorer, and then cracked along the line. In the case of the thin cover slips, the original cover slips were split in half. As well as reducing the volume of LC needed, this helped to reduce the effect of 'bowing' in the centre of the sample. All glass was treated with a succession of solvents to remove contamination, in the following order: de-ionised (DI) water + detergent (decon90, Decon Laboratories), DI water, methanol, and isopropyl alcohol (IPA. Methanol and IPA both Fisher Scientific). The glass pieces were sonicated for 20 minutes per cleaning stage, in a USC-TH ultrasonic bath sonicator. After the DI water stage and after the IPA stage, the glass pieces were individually dried with compressed air to prevent 'drying marks'.

3.2.2 Surface treatment for alignment on substrates

Substrates for Schlieren cells did not have any alignment layer. After filling, all Schlieren cells were heated into the isotropic phase and then cooled back into the nematic. Planar cells were constructed with a mixture of 0.5% poly vinyl alcohol (PVA, Arcos Organics, molecular weight = 86,000) in DI water (wt/wt, measured by Mettler Toledo microbalance). To dissolve the PVA in the water, the mixture was heated to 80°C for 1 hour (on an Arex Digital Pro hot plate), with a magnetic stirrer at 300 rpm. A small volume of the solution was applied to the sample with a pipette, immediately before spin-coating the sample at 70 ± 1 rps for 60 seconds (spin-coater: KLM). Finally, the substrates were baked in an oven (Cook Works toast oven KWS1009) at 110 °C ± 10 °C for 20 min. The substrates were rubbed with a felt cloth three times to promote the direction of planar alignment. During assembly, the rubbing directions were antiparallel.

3.2.3 Cell construction

The majority of samples were constructed with polyester spacer film (Melinex). Dust and large contamination were removed from the film with compressed air. Small quantities of UV (ultraviolet) curing glue (UVS 91, Norland) were used to secure the film between the two substrates. For cells with a gap size of ~10 μm or thinner, a mixture of spacer beads (Duke Standard, Thermo Scientific) and glue was used to create the cell gap. Dried beads were mixed with UV glue Norland Optical Adhesive 68. After gluing, the cells were placed under a UV light source (UV lamp J0202, 36W) for 30 minutes.

3.2.4 Determination of cell gap

The standard method to measure cell gap d is based on the principle of thin film interference. It can be shown that for two materials separated by an air gap (assumed that the refractive index of air is equal to one), the reflection spectrum shows a set of equally spaced fringes. Using interference fringes to measure the thickness of a transparent layer is described in detail in Goodman, 1978 [1]. If two maxima are selected with the first at wavelength λ_0 and the last λ_N, and N_{max} is the number of maxima, the cell gap is given by:

$$d = \frac{N_{max}\lambda_0\lambda_N}{2(\lambda_N - \lambda_0)} \qquad \text{Eqn. 3.1}$$

Wherever possible this method was used, five measurements of cell gap taken at different areas in the cell. The spectrometer used was an Ocean Optics HR 4000, in an Olympus BH2 microscope with Olympus IC 10x objective lens and a broadband light source. However, in the case of cell gaps above ~20 μm, the interference fringes were not clearly visible. In these cases only an estimate of the cell gap could be given.

3.2.5 Cell filling and sealing

Except where otherwise specified, the cells were filled with the capillary method (i.e. introducing a quantity of LC to the edge of the cell with a pipette, after which surface tension draws the LC into the rest of the cell). After filling, UV glue UVS 91 (Norland) was used to seal any exposed edges, to prevent leaking and exposure to objective immersion oil. The cells were the placed under a UV light source for 30 minutes. Finally, to fit into the inverted hot stage, sealed cells were secured to standard glass slides with a transparent quick-drying glue.

3.3 Polarising microscopy

Some analysis of samples was performed using a standard polarising microscopy setup, for experiments that did not require use of optical tweezers. For example, determining alignment of the samples, determining alignment on particles, and measuring the transition temperatures of liquid crystals. The microscope was a Leica DM 2700P, with objective lenses Leica 5 x, 10 x and 20 x. For the highest resolution images, an ultra long working distance 50 x objective was used (Leica N Plan 50 x, NA = 0.50). The microscope was adjusted for Köhler illumination. When heating or cooling of the cell was required, a hot stage (Linkam Peltier LTSE 120) was used in conjunction with its controller (T95 PE) and water cooling system. images were recorded on a Nikon D7100 (CMOS (complementary metal-oxide-semiconductor) camera).

3.4 Laser Trapping

3.4.1 Motivation

In the following chapters we will be investigating the trapping of particles trapped at defects in liquid crystals, and how the trapping strength varies under certain physical conditions. We required a method to control the

position of the particles relative to the defects, and also (see chapter 6) to determine whether particles are adhered to the upper or lower substrate of the cell (Fig. 3.1). For this purpose, we required a tool with the ability to manipulate objects on a micron scale, while suspended in a liquid or liquid crystal medium up to ~100 μm thick. There is a tool which is fulfils this purpose, optical tweezers.

3.4.2 Introduction to optical trapping

Optical traps (in their application, sometimes known as optical tweezers or laser tweezers) have practical uses across many different fields, such as bio-technology and bio-sensing [2], colloid science and rheology [3], and even fundamental physics [4]. There are two major uses for this type of instrument. The first has the most in common with its namesake, 'tweezers', as a tool to manipulate objects on a small scale. A review of these applications can be found in Grier, 2002 [5]. Optical traps can also be used as an analytical instrument. Since the behaviour of an object in an optical trap can be predicted (see section 3.4.3 below), the motion of the object can be used to infer the physical properties of the medium surrounding it.

3.4.3 Principles of optical trapping[6, 7]

All optical trapping systems operate under the same principle. Photons carry momentum p_{ph} equal to:

$$p_{ph} = \frac{h}{\lambda_{ph}}, \qquad \text{Eqn. 3.2}$$

where λ_{ph} is the photon's wavelength and h is Planck's constant. For example, if $\lambda_{ph} = 1070\ \mathrm{nm}$ (the laser described in section 3.4.7), $p_{ph} \approx 6.2 \times 10^{-28}\ \mathrm{Ns}$. If the power was 0.5 W, that is equivalent to 2.7×10^{18} photons. If every photon was completely absorbed by an object such as a particle, 1.7 nN of force would be exerted on the object. In physical systems, pressure efficiency will be less than 100%, usually less than 10%.

Dielectric particles do not absorb the photons, instead scattering them. Unlike a perfectly absorbing particle, momentum from the beam is not transferred to the particle with 100% efficiency. The efficiency of a laser trap Q_{OT} is given by [6]:

$$F_{particle} = \frac{Q_{OT} P n_1}{c} \qquad \text{Eqn. 3.3}$$

where P is the laser power, c is the speed of light, n_1 is the refractive index of the medium. Q_{OT} is a dimensionless quantity that depends on a number of factors. Factors include the geometry of the trap, and the relative refractive indices of the particle and the medium $n_{rel} = n_2/n_1$, where n_2 is the refractive index of the particle. It should be noted that trapping only occurs when $n_{rel} > 1$. A typical Q_{OT} for practical laser tweezing experiments is 0.035, for a glass sphere (radius $a = \lambda_{ph}/4$) in water ($n_1 = 1.33$) [6], which corresponds to a maximum force on the particle of $F_{particle} = 35$ pN. Values of Q_{OT} can be higher for experiments conducted in laser tweezing systems; Sanders recorded Q factors of approximately ~0.2 for 6 µm polystyrene particles in MLC-6648 [8], a liquid crystal which is used in chapter 6 of this thesis, and a similar particle size (between 1 and 10 µm).

In a laser beam, the intensity will vary both along and perpendicular to the optic axis of the beam. For example, in a single Gaussian beam (in TEM_{00} mode), the intensity is highest at the 'beam waist', which is the area where the beam is at its narrowest. High gradients in intensity produce 'gradient forces' $\boldsymbol{F_{gradient}}$, which cause particles to be pulled into the beam's geometric focus. This is in contrast to the scattering forces, $\boldsymbol{F_{scat}}$, which push the particles in the direction of the light propagation. The total force on a particle is $\boldsymbol{F_{particle} = F_{gradient} + F_{scat}}$. The relative influence of the two forces depends on the scale of the particles. For Rayleigh scatterers, $\boldsymbol{F_{gradient}}$ dominates [9]. Conversely, for larger Mie scatterers, $\boldsymbol{F_{scat}}$ dominates.

The forces involved for a particle trapped in a single Gaussian beam in TEM_{00} mode in the Mie regime were first calculated theoretically by Ashkin et al [10]. The particle size, material type, and beam type most closely match the conditions of the laser tweezing experiments performed in chapter 6 of this thesis: in other words, the conditions apply to a Gaussian beam with a dielectric particle in the ~μm size range.

To undestand how momentum is transferred between photons in the beam and a particle, let us consider a particle that has been displaced in the positive direction along the direction of propagation of the beam (axial displacement), after the focus of the trap. A diagram (Fig. 3.2) is shown below.

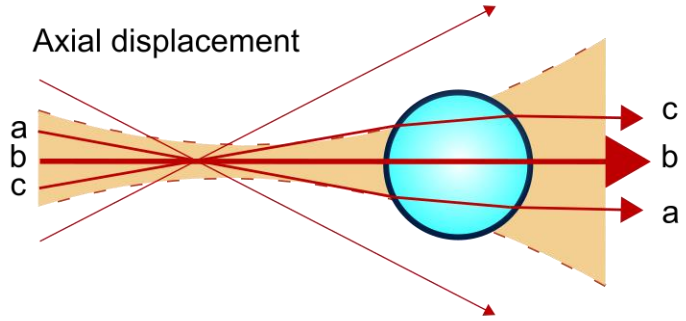

Fig. 3.2. Schematic representation of a particle displaced axially in a Gaussian beam, after the focus of the trap. Note that the beam, therefore the pressure, is highest at the centre of the beam (ray b).

From Fig. 3.2, we see a representation of how the photons' motion is changed after passing through the particle, due to being refracted (Snell's law). The change in direction of the photons corresponds to a change in momentum (Fig. 3.3).

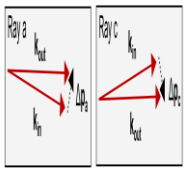

Fig. 3.3. Representation of change in momentum of rays a and c from Fig. 3.2. The change in momentum of the photons (Δp_a, Δp_c) is equal to the difference between momentum of the photons entering the particle (k_{in}) and the momentum of photons leaving the particle (k_{out}). The 'missing' momentum is transferred to the particle.

The momentum change in the photons corresponds to a momentum transfer to the particle, or, a force applied to the particle. The forces transferred to a particle due to ray a and ray c are shown below (Fig. 3.4).

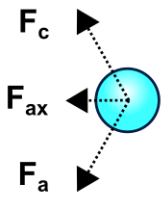

Fig. 3.4. Force acting on particle due to change in direction of photons in ray a and ray c (F_a and F_c respectively). The resultant force is F_{ax}. In this case, for a positive axial displacement relative to the centre of the trap, F_{ax} acts to move the particle back towards the centre of the trap. Due to symmetry, there is no force perpendicular to the propagation direction of the beam.

The diagrams above considers only some of the rays passing through the particle, but a similar argument can be made for any other rays. An axial force in a laser trap will restore a particle towards the centre of the trap along the direction of propagation of the beam in the positive or negative direction. We can also consider a displacement perpendicular to the propagation direction of the beam (transverse displacement (Fig. 3.5)).

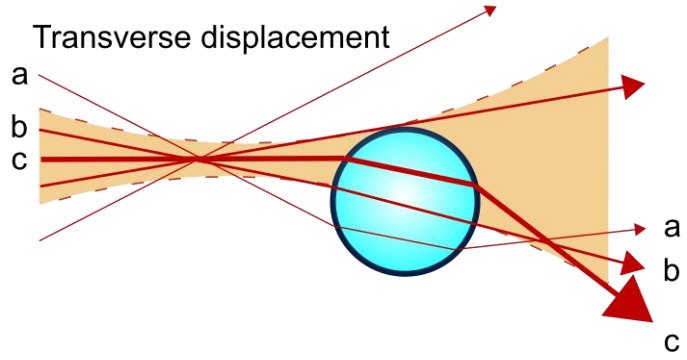

Fig. 3.5. Schematic diagram representing a particle displaced in a direction perpendicular to the propagation direction of a Gaussian beam.

As for the transverse case, displacing the particle results in a restoring force directing the particle towards the centre of the trap (Fig. 3.6).

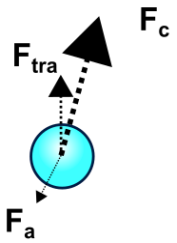

Fig. 3.6. The change in momentum of ray a and ray c for a transverse displacement (Fig. 3.5) causes forces on the particle F_a and F_c respectively, with resultant force F_{tra}. F_c is larger than F_a, as F_c originates from a ray from the centre of the beam, where the beam is more intense and therefore the number of photons and momentum transfer is greater. This means that F_c has more effect than F_a, so F_{tra} acts in a direction to restore the particle towards the centre of the trap.

Another way to think about particle trapping is to consider the particle at different positions in the trap along the same axis. In Fig. 3.7 below we see a cross-section of a Gaussian beam along the z-axis. At positions away from stable trapping, restoring forces act to bring the particle towards the 'centre' of the trap. A graph of the forces involved in Fig. 3.7 is shown in Fig. 3.8 below.

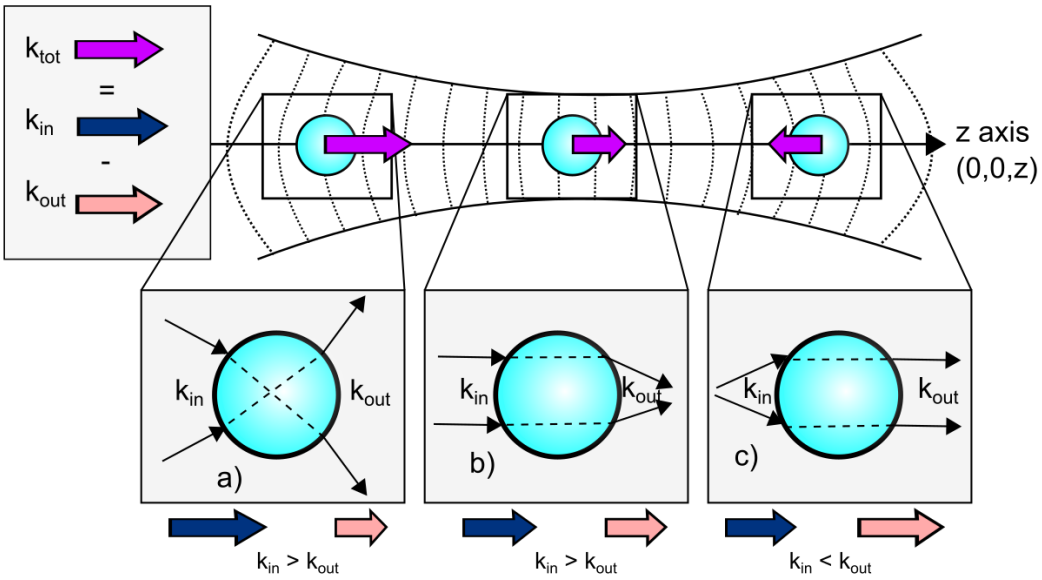

Fig. 3.7. Schematic diagram illustrating the principles of optical trapping along the z-axis [7] in a single Gaussian TEM_{00} beam. The beam's profile is perpendicular to the page and its propagation direction is parallel to the z axis. In this example we are considering the z component only and assuming that the particle is fixed on the z axis at x = y = 0. The total momentum transferred to the particle k_{tot} is equal to the momentum entering the particle k_{in} minus the momentum transferred out of the particle k_{out}. The change is caused by scattering and gradient forces. The resultant force either pushes the particle in the direction of the beam's propagation (a, b) or in the reverse direction of the beam's propagation (c), depending on whether $k_{in} > k_{out}$. Where $k_{in} = k_{out}$, stable trapping will occur. It should be noted that the position where stable trapping occurs is between (b) and (c), not at the 'geometrical focus', but further along the direction of the beam's propagation. A graph of resultant forces corresponding to this diagram is shown in Fig. 3.8 below.

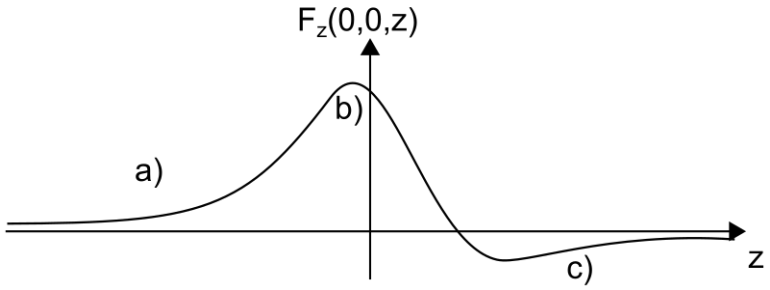

Fig. 3.8. Illustrative plot of resultant forces along z axis for particles trapped in the Gaussian beam illustrated in Fig. 3.7 above, including positions marked in Fig. 3.7 a), b) and c). At position a), a positive force acts along the z-axis. At b), the point of highest intensity in the beam, the force is still positive. At point c), the resultant force is negative and the particle moves towards the origin of the beam. The 'centre' of the trap is the point where $F_z = 0$, which is after the point of highest intensity of the beam.

To use an optical trap as a set of 'laser tweezers', either the sample can be moved relative to the beam (on an x-y stage), or the path of the laser beam itself is diverted with an optical element such as an acousto-optic modulator (AOM). Both of these methods were used in this project.

3.4.4 Optical traps as a potential well[11]

It has been shown that particles in an optical trap experience a 'restoring force' towards the centre of the trap. For sufficiently small displacements, one could consider the trap as a potential well with potential energy U:

$$U = \frac{1}{2}\kappa\langle \boldsymbol{R}^2 \rangle_{eq} \qquad \text{Eqn. 3.4}$$

where κ is the 'trap stiffness', analogous to e.g. the stiffness of a spring undergoing simple harmonic motion. Meanwhile, $\langle \boldsymbol{R}^2 \rangle_{eq}$ is the variance of the displacement $\boldsymbol{r}$ of the particle from the centre of the trap, and is

independent of time. The force on the particle in the trap is the gradient of the potential energy:

$$\boldsymbol{F}_{particle} = -\nabla U = -\kappa \boldsymbol{R} \qquad \text{Eqn. 3.5}$$

Finally, one can apply the equipartition theorem, associating one $k_B T$ of energy with each degree of freedom. It can be shown that for each component j:

$$k_B T = \kappa_j \langle R_j^2 \rangle_{eq} \qquad \text{Eqn. 3.6}$$

where k_B is Boltzmann's constant, and T is temperature. From Eqn. 3.6, it can be seen that if $\langle \boldsymbol{R}^2 \rangle_{eq}$ is found by tracking a particle for a sufficiently long time, the trap stiffness can be calculated. As it is noted in chapter 9 of Microrheology with Optical Tweezers, 2016 [11], there are a great variety of ways to investigate forces on a particle in a trap. However, using the equipartition theorem as described above is the only method which is independent of the viscoelastic properties of the medium.

3.4.5 Other methods of measuring forces on LC colloids

The traditional method given above is commonly used. However, as is discussed in more detail in Sanders, 2012 [8], there are several ways to use optical tweezers to investigate forces on a particle. Methods can be classified as 'active' (where forces on a particle are measured while the particle is in the laser trap), or 'passive' (where the particle is not in the trap during force measurements). Methods will be discussed in more detail in chapters 5 and 6.

3.4.6 Other methods of colloid manipulation

There are some limitations to the conventional optical trapping, particularly when dealing with LC colloids. Most liquid crystals tend to have quite large refractive indices, larger than most dielectric materials commonly used to

make particles e.g. glass. Following the criterion $n_2 > n_1$ is possible by selecting particular low refractive index liquid crystals and high refractive index particles (see chapter 6), but it does limit the materials that can be used in an experiment.

There are alternative mechanisms available when it comes to laser tweezers' use as a manipulation tool. Firstly, the power of the laser can be increased to the extent that the electric field associated with it induces a Freedericks transition within the liquid crystal [12]. The resulting distortion which can then be used to transport particles regardless of refractive index [13]. There can also be a mechanism at play even below the Freedericks threshold, the director field is distorted due to an interaction with the electric field [14]. The strength of trapping by the Freedericks transition method depends on geometry and as it often occurs in conjunction with heating. Another method is to completely melt the liquid crystal into the isotropic phase, as discussed in the following section.

3.4.6.1 Local melting of liquid crystal

If a sample of nematic liquid crystal containing some colloids is heated into the isotropic phase, it is possible to see the confining influence of the boundary between the two phases (the particles remain in the isotopic region). In West et al 2002 [15], various mechanisms are discussed including surface tension, and elastic distortion of the director at the interface. In Škarabot et al 2013 [16], this effect was reproduced by the use of laser tweezers. By using a layer of ITO glass to absorb the laser light, the heating was significant enough to heat the liquid crystal into the isotropic phase. As this method has a high versatility to be applied particles of arbitrary refractive index and size, it was selected for most of the experiments in this project as a method of adjusting particle position.

3.4.7 Optical tweezing setup

Two different optical tweezing systems were used during these experiments, although both were built along similar specifications. A Leica microscope was used as the base in some preliminary work (described in chapter 6). All other work was performed on a Nikon microscope, which will be discussed below.

The inverted microscope, Nikon Eclipse Ti-U was used as the base for the complete laser tweezing setup. A simplified diagram of the setup can be seen in Fig. 3.9 below.

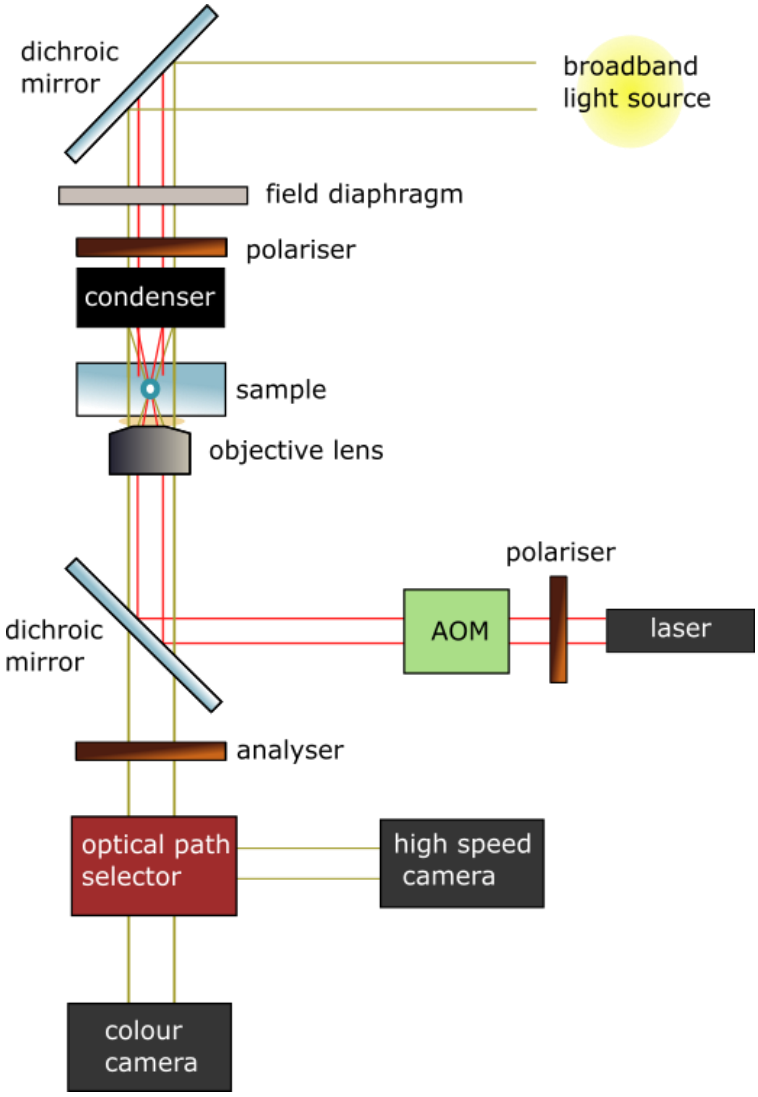

Fig. 3.9. Schematic diagram illustrating the optical setup for the Nikon laser tweezing system. The AOM is an acousto-optic modulator which modifies the path of the laser beam. For more details of components, see below.

There are two light paths to consider in the setup shown in Fig. 3.9. The first concerns the laser beam, used for trapping. Near-infrared light of wavelength 1070 nm is output from the laser, passes through a polariser and an acousto-optic modulator, after which it is directed into a high numerical aperture objective lens (100 x magnification, 1.3 NA) and focused into the sample. The visible light is used for imaging, including polarisers that can be

crossed when necessary. The components specific to laser tweezing were supplied by Elliot Scientific as part of the E3500 system.

The laser was an ytterbium fibre laser (model YLR-5-LP-Y12, IPG Laser). Emission wavelength was $\lambda = 1070\ \mathrm{nm}$, with linewidth $\Delta\lambda = 1\ \mathrm{nm}$. The laser power was variable up to 5W, and could be operated both in continuous and pulsed modes, however, only the continuous mode was used for these experiments. The laser output was linearly polarised. The polariser seen in Fig. 3.9 in front of the laser was used to further adjust intensity when required, but was set parallel to the laser polarisation where not otherwise specified, for maximum transmitted intensity of the beam.

The laser beam was modified during its pass through an acousto-optic modulator (AOM). In brief, an acoustic wave can create a change in refractive index at intervals in the medium (considered as a standing wave because timescale is much smaller for light than for sound). A simple example can be seen by considering the AOM as an optical Bragg diffractor, as illustrated in Fig. 3.10 below.

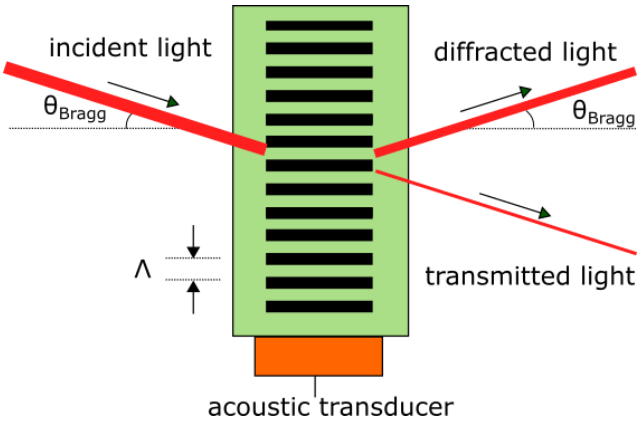

Fig. 3.10. Representation of Bragg diffraction in an acousto-optic modulator. The light and dark strips represent a sound wave, where the refractive index changes according to the amplitude at that point in the medium [7].

Constructive interference will occur at the angle θ_{Bragg}, according to the Bragg condition:

$$\sin\theta_{Bragg} = \frac{\lambda_{inc}}{2\Lambda} \qquad \text{Eqn. 3.7}$$

where λ_{inc} is the wavelength of the incident light, and Λ is the wavelength of the sound (which in turn depends on the material properties of AOM medium, and the sound frequency). In a device, the beam can be deflected by a desired angle by selecting the appropriate frequency (or superpositions of several). In this setup, the desired position of the laser spot in the field of view was input into the software, and all the appropriate calculations to instruct the AOM were performed within the software. Using the AOM allowed the position of the laser spot relative to the sample to be adjusted quickly and precisely during the process of an experiment, without the need to move the sample relative to the camera.

As a final note, while not included in Fig. 3.10, there are also a number of steering mirrors in the beam path between the laser and dichroic mirror,

used to centre and otherwise adjust the main beam. There is also a filter between the laser and cameras, to prevent damage to the camera when the laser is in operation.

The components related to particle tracking were also supplied by Elliot Scientific, as part of the E4500 particle tracking option. The high speed camera was a Basler AG piA640-210gm (frame rate up to 210 fps), based on a KAI-0340 CCD (charge coupled device). The pixel size was calibrated using a stage micrometer (7.5 ± 0.1 μm), and can be used to calculate the pixel size at arbitrary magnification.

The objective lens used for measurements was a Nikon CFI Plan Fluor 100 x with oil immersion (numerical aperture = 1.30). It had a working distance of 0.16 mm and was infinity corrected for use with standard cover slips (0.17 mm). It was used with immersion oil Nikon NF2 (refractive index of 1.515 at 23 °C). The broadband light source was a metal halide lamp.

As well as the high speed camera used for all physical measurements in this paper, a colour camera (Nikon D7100, CMOS sensor) was used for general imaging purposes. The samples were mounted on a manual x-y stage with z adjustment. There was also a Peltier hot stage available, the Linkam PE 100-NI. With the addition of Kapton tape insulation, the temperature range was tested from room temperature up to 55 °C, with accuracy of approximately ± 2 °C (based on calibration with a Kane-May KM330 thermocouple).

3.5 Particle Tracking

3.5.1 Methods of particle tracking

There are two chief methods of tracking the position of a particle over time, each of which has its own advantages and disadvantages. The first is the use of a quadrant detector, which has potentially higher accuracy in measurement of particle position. The second is to use a camera in

conjunction with software to calculate the centre of mass of the particle. Computer-based tracking methods are relatively easy to install, and is potentially quite versatile as the software can be modified to e.g. calculate the orientation of a particle. Finally, the computer-based method can explicitly measure the position of a particle relative to the defects. For this reason, the second method was chosen.

For example, the brightness threshold chosen to calculate the centre of the particle had an effect on the recorded location of the particle. Repeated measurements were performed for the same particle at the same defect, but with different brightness thresholds at which the tracking software determines the edges of the particle. Choosing several thresholds results in a standard error of 20-30%. Choosing a threshold that was unsuitable (e.g. included the surrounding medium) has a much larger effect, but was easy to identify within the software, and thus exclude from measurements.

3.5.2 Software specifications

The software used for particle tracking was a proprietary Labview program published by Elliot Scientific.

The raw data output from the particle tracking software gave the time, x and y co-ordinates of the particle centre. The error on time is ±5 ms. The error on the x and y co-ordinates varies with particle size, shape, contrast and other factors, but is always at least as large as the size of a single pixel (± 0.08 μm at 100 x).

To process the data, code was written in Spyder [18] (based on Python 3.5.1 [19]) to calculate particle trajectory and mean square displacement. In general, the software and setup were found to be most effective for tracking particles of 5 μm and larger, for timescales of ~1 minute.

3.6 Conclusion and Summary

In this chapter, the materials and procedure used to construct samples were outlined. The second part of the chapter introduced the setup and principles behind the laser tweezing system. This includes the principles of laser trapping, both by the conventional method, and the local melting method. Particle tracking techniques were discussed. This chapter should provide a reference for techniques used in later chapters. Using the methods in this chapter, in chapters 5 and 6 we will perform an extensive investigation into the confinement of particles at defects in a liquid crystals for the first time using passive methods. Methods of manufacturing samples will also be used in chapters 4 and 7.

The next chapter is the first of the results chapters, on the effect of ~100 nm scale particles on the bulk properties of liquid crystals.

References

1. Goodman AM (1978) Optical interference method for the approximate determination of refractive index and thickness of a transparent layer. Applied Optics 17:2779–2787. doi: 10.1364/AO.17.002779
2. Wang MM, Tu E, Raymond DE, et al (2005) Microfluidic sorting of mammalian cells by optical force switching. Nature Biotechnology 23:83–87. doi: 10.1038/nbt1050
3. Meyer A, Marshall A, Bush BG, Furst EM (2016) Laser tweezer microrheology of a colloidal suspension. Journal of Rheology 50:77–92. doi: 10.1122/1.2139098
4. Li T (2013) Fundamental Tests of Physics with Optically Trapped Microspheres. In: Springer Science+Business Media New York. pp 9–21
5. Grier DG (2003) A revolution in optical manipulation. Nature 424:810–816. doi: 10.1038/nature01935
6. A. Rohrbach, J. Huisken, and E. H. K. Stelzer, in *Optical Imaging and Microscopy: Techniques and Advanced Systems*, edited by P. Török and F.-J. Kao (Springer, 2003), pp. 357–388.
7. Saleh BEA, Teich MC (1991) Fundamentals of Photonics. Wiley.
8. Sanders JL (2012) A study of microviscosity in liquid crystals using laser tweezers. University of Manchester
9. Harada Y, Asakura T (1996) Radiation forces on a dielectric sphere in the Rayleigh scattering regime. Optics Communications 124:529–541. doi: 10.1016/0030-4018(95)00753-9.
10. Ashkin A (1992) Forces of a single-beam gradient laser trap on a dielectric sphere in the ray optics regime. Biophysical Journal 61:569–82. doi: 10.1016/S0006-3495(92)81860-X
11. Tassieri M (2016) Microrheology with Optical Tweezers. In: Tassieri M (ed) Microrheology with Optical Tweezers: Principles and Applications. Pan Stanford Publishing Pte., pp 219–255
12. Durbin SD, Arakelian SM, Shen YR (1981) Laser-induced diffraction rings from a nematic-liquid-crystal film. Optics letters 6:411–413. doi: 10.1364/OL.6.000411
13. Muševič I, Škarabot M, Babič D, et al (2004) Laser trapping of small colloidal particles in a nematic liquid crystal: Clouds and ghosts. Physical Review Letters 93:1–4. doi: 10.1103/PhysRevLett.93.187801
14. Škarabot M, Ravnik M, Babič D, et al (2006) Laser trapping of low refractive index colloids in a nematic liquid crystal. Physical Review E 73:1–10. doi: 10.1103/PhysRevE.73.021705

15. West JL, Glushchenko A, Liao G, et al (2002) Drag on particles in a nematic suspension by a moving nematic-isotropic interface. Physical Review E - Statistical, Nonlinear, and Soft Matter Physics 66:1–4. doi: 10.1103/PhysRevE.66.012702

16. Škarabot M, Lokar Ž, Muševič I (2013) Transport of particles by a thermally induced gradient of the order parameter in nematic liquid crystals. Physical Review E 87:1–6. doi: 10.1103/PhysRevE.87.062501

18. Spyder version 2.3.8 (2015).

19. Python version 3.5.1 (2015).

Chapter 4 Effect of Submicron Spheres and Janus Particles on a Nematic Liquid Crystal

4.1 Introduction

In chapter 2 we introduced some important physical properties of liquid crystals. These properties affect the performance of commercial liquid crystal devices. For example, the elastic constants, viscosity, and dielectric constants all have an effect on response time. Transition temperatures affect the temperature range of a device. The order parameter is a useful measure, as most other physical properties are related to it.

In the literature, there are some studies on how the bulk properties of liquid crystals are affected by the addition of particles. Changes in bulk properties have been reported for carbon nanotubes [1–4], gold nanoparticles [5–7] and graphene oxide flakes [8]. Dielectric particles are studied less often. For example, a drop in nematic-isotropic transition temperature (T_{NI}) of up to 2°C was reported with 7 nm silica particles at concentrations of 0.3 g/cm^3 by Hourri et al [9]. All the particles in the examples listed so far have been very small (<20 nm) in at least one dimension. Larger particles are less commonly studied in the bulk. One study [10] added 500 nm diameter particles to a nematic liquid crystal at high concentrations (>50%) and found an unusual soft solid was created as a network of aggregates.

In this chapter, we report investigations into the less studied regime of low concentration (~1% wt/wt), and submicron particle diameter (~500 nm). If the aim is to work towards building an electrophoretic device based on liquid crystal colloids, the particles must be able to move independently (i.e. not in aggregates) so the concentration cannot be too high. This size regime is also more similar to existing electrophoretic devices that use particles larger than the ~nm scale (typically ~50 µm). The particles studied also included doublet-shaped Janus particles. This means that the research in this chapter is the first time that Janus particles under <1 µm have been studied in a

liquid crystal, and also the first time the bulk properties of liquid crystals have been studied with the addition of Janus particles.

The transition temperatures, order parameter, dielectric constants and elastic constants were measured at a concentration of 1% wt/wt. These properties were studied as they can all be measured in the bulk and also are important to the performance of a device. No significant changes in these parameters were found once account was taken of the errors. However, this informed the direction of research in later chapters towards a larger particle size regime and lower concentrations of particles.

4.2 Materials

Two types of particles, spheres and Janus particles, were created[1] by the dynamic swelling method [11]. The dynamic swelling method is used to create polymeric Janus particles in solution, first developed by Sheu et al [12]. The spheres used in this experiment were composed of glycerol dimethacrylate (GDMA). Doublets/triplets of GDMA and *N*-hydroxyethyl acrylamide (HEAm) were also synthesised. The structures of GDMA and HEAm monomers are in Fig. 4.1, and the physical shape of particles represented in Fig. 4.2.

[1] Both particle types were synthesised by Sean Butterworth, School of Chemistry, University of Manchester.

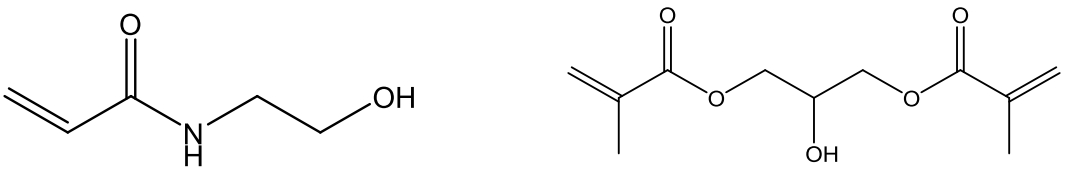

a) b)

Fig. 4.1. Chemical structures of a) glycerol dimethacrylate (GDMA) and b) *N*-hydroxyethyl acrylamide (HEAm)

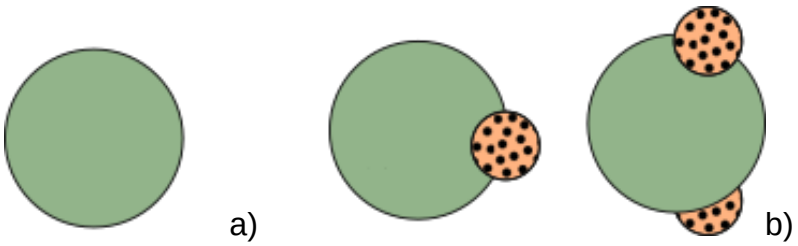

Fig. 4.2 Schematic representing the physical shape and structure of a) spherical particles, SRB 288 and b) Doublets (left) and triplets (b) in SRB-383. The physical shape was verified by tunnelling electron microscopy[11]. Spherical particles consist of GDMA only, and the doublets/triplets consist of GDMA and HEAm.

The liquid crystal was 4-Cyano-4'-pentylbiphenyl (5CB) [13], chosen because its properties are very well-documented in the literature.

4.2.1 Selection of Solvent

A solvent was chosen in which to suspend the particles in order to accurately weigh out small quantities later on. The required characteristics of the solvent were to:

a) Disperse particles without damaging them.
b) Dissolve liquid crystal (specifically 5CB).
c) Have high volatility.

To make sure criterion a) was fulfilled, a solubility study was conducted with a range of solvents (polar, h-bonding and non-polar, according to the

Hansen solubility parameters [14,15]). From the suitable area, n-hexane was chosen.

4.2.2 Dynamic Light Scattering[16,17]

Dynamic light scattering (DLS) is a technique used to measure the size distributions of particles. DLS does not measure the radius of particles directly, but instead looks at the Brownian motion of the particles (i.e. random motion of a particle due to collisions with molecules in the medium). DLS measures the diffusion coefficient D of the particles. If the viscosity of the solvent and the temperature of the system are known and the assumption is made that the particle can be treated as spherical, then the particle radius, a, can be found via the Einstein-Stokes equation:

$$D = \frac{k_B T}{6\pi\eta a}. \qquad \text{Eqn. 4.1}$$

In a DLS machine, a monochromatic laser of wavelength λ_{DLS} is passed through the sample. A detector is set at an angle θ_{DLS} from the incident laser beam, meaning that only light that has been scattered by the sample will be detected. The wavefronts from the scattered particles interfere to form a pattern called a 'speckle pattern'. As with a diffraction pattern from a regularly spaced grating, separations between maxima and minima that depend on particle separation.

To find the diffusion coefficient, changes in the speckle pattern are measured over time, including the timescale of Brownian motion (~ 10ms). The autocorrelation function g compares the intensity of the speckle pattern at time t with the intensity of the speckle pattern at a time $t + \tau_{DLS}$ (where τ_{DLS} is some arbitrary delay):

$$g^2 = \frac{\langle I_s(t) I_s(t + \tau_{DLS})\rangle}{\langle I_s(t)\rangle^2}, \qquad \text{Eqn. 4.2}$$

where I_s is the intensity of the speckle pattern. A rapidly fluctuating signal produces a smaller value of g, and a less rapidly fluctuating signal produces

larger values of g. It can be shown that for spherical particles undergoing Brownian motion, the autocorrelation function is given by:

$$g(\tau) = 1 - e^{-2Dq_{DLS}{}^2\tau_{DLS}}, \quad \text{Eqn. 4.3}$$

where q_{DLS} is the magnitude of the scattering wave vector:

$$q_{DLS} = |\boldsymbol{q_{DLS}}| = \frac{4\pi}{\lambda_{DLS}} \sin\frac{\theta_{DLS}}{2}. \quad \text{Eqn. 4.4}$$

Dynamic light scattering machines can calculate the particle diameter or radius in a number of different ways, bearing in mind that samples are not necessarily completely monodisperse, instead containing a distribution of different sizes.

The diameter obtained by fitting the autocorrelation function is actually the 'Z-average' diameter, D_z [18,19]. It is the harmonic mean of the particle distribution weighted by intensity of scattered light from individual particles, S_i:

$$D_z = \frac{\sum S_i}{\sum S_i/D_i} \quad \text{Eqn. 4.5}$$

where D_i is the diameter of an individual particle. Some DLS measurements also include a 'number average' measurement. In this case, Mie theory is used to reconstruct the full distribution of particles based on the Z-average. Mie theory is applicable when particles are spherical and in an intermediate size regime between optical ($2\pi a \gg \lambda_{DLS}$) and Rayleigh scattering ($2\pi a \ll \lambda_{DLS}$). For example, the laser of the Malvern Zetasizer has a wavelength $\lambda_{DLS} = 633$ nm, and the particles used in this chapter are approximately 500 nm in diameter ($2\pi a = 3140$ nm), which is in the Mie regime. The number average calculation is also based on other assumptions, such as the refractive index of the particles.

It should also be noted that all DLS measurements rely on some other assumptions, such as the number and volume density of the particles is

assumed to be very low (in other words, the model assumes that the scattering contributions from individual particles can be summed together), making the technique inappropriate for a material with a high density of scattering sites such as a nematic liquid crystal. Also, while the Mie regime is used for the 'number average', DLS can used to measure the properties in smaller size regimes, for example, proteins with dimensions between 1 - 10 nm [20]. In these cases, different assumptions must be used when processing the results. At larger size scales than ~1 μm, there may be difficulty in dispersing the particles in the solvent, which would also make DLS unsuitable.

4.2.3 DLS Versus Scanning Electron Microscopy[21]

Dynamic light scattering is not the only technique used to measure the diameters of particles. Another technique used to measure the scanning electron microscopy (SEM). This technique is capable of imaging at resolutions on the ~ nm scale. For this reason, SEM is typically used to size particles that are too small to be sized optically ($\lesssim$ 10 μm) but significantly larger than the SEM resolution (> 100 nm). After obtaining an image of the surface, particle radii can be measured by inspecting the particles on imaging software. Whether DLS or SEM are more appropriate to use to measure radii of particles depends on the system being studied. Some differences between SEM and DLS will be outlined below

An important difference between DLS and SEM is that the two techniques measured different diameters. SEM measures the diameter according to the physical volume occupied by the particles. Gold sputtering, if used, is typically ~10 nm thick, which could potentially affect measurements of radius. In DLS, the diameter is from the Stokes radius, or hydrodynamic radius, as shown in the Einstein-Stokes equation. The Stokes radius can include any surface charge, surfactant, or other molecules associated with the particle. The difference between the two diameters is usually small for particles above the nanoscale. For example, the Stern layer typically has a thickness of the order 0.1 nm [30]. The diffuse electrical double layer may

extend up to ~10 nm [23, 24]. Surfactants such as N-dimethyl-n-octadecyl-3-aminopropyltrimethoxysilychloride (DMOAP, used as a surfactant for particles in later chapters), have their largest dimensions on the scale of ~1 nm.

Both DLS and SEM are designed to be effective at measuring the radius of spherical particles. SEM may be able to give more information on the size of compound particles such as Janus particles.

A further advantage of DLS is it can measure the properties of a large ensemble of particles in a short space of time, whereas SEM requires the particles to be sized individually, limiting the measurement to typically ~100 particles.

Another difference between DLS and SEM is that because SEM is a surface technique, it cannot measure the properties of particles in a solvent. For example, if one needed to determine whether a particle's radius changed due to swelling in a solvent and by how much, it would not be possible to determine this by SEM. Instead, DLS could be used.

A summary of differences between DLS and SEM can be seen in Table 4.1 below.

	DLS	SEM
Technique type	Bulk (in solvent)	Surface only
Measures	Stokes radius	Excluded volume
Particle material	Dielectric	Conductive, or dielectric + sputtering conductive layer
Particle density	V. low	Low-high

Table 4.1. Comparison of some properties of DLS and SEM when measuring the diameters of particles

4.2.4 Laser Doppler Velocimetry

Similarly to the particle size distribution, the zeta potential of particles is measured by observing the motion of particles and using the known properties of the solvent to calculate it. In this case, an electric field is applied to the particles. We know from chapter 2 that the 'electrophoretic mobility' is related to the zeta potential as well as the dielectric constant and viscosity of the medium.

In laser Doppler velocimetry (LDV), the velocity of a particle is measured by measuring the Doppler shift $f_{doppler}$ of a beam that has been scattered after passing through the sample relative to a reference beam that has not passed through the sample [25]. The Doppler shift is measured by interfering the scattered beam with the reference beam. Because each beam has a slightly difference frequency, the two beams interfere to produce a 'beat pattern' with spacing T_{LDV} that is inversely proportional to Doppler shift.

$$T_{LDV} = \frac{1}{f_{doppler}} = \frac{\lambda_{zeta} c}{v_{drift}} \qquad \text{Eqn. 4.6}$$

where λ_{lDV} is the wavelength of the reference beam.

Some instruments, including the Malvern Zetasizer which is used to measure the Zeta potential of the submicron spheres and Janus particles in this chapter, use a variation on laser Doppler velocimetry called phase analysis light scattering (PALS) [26]. Instead of using frequency information, instead, phase information is used. This allows smaller electric fields to be used in the device, allowing measurements to be taken at much smaller electrophoretic mobilities than conventional LDV, measuring electrophoretic mobilities as low as $10^{-12}\ \mathrm{m}^2\ \mathrm{s}^2\ \mathrm{V}^{-1}$ with resolution between 0.5 and 5%. PALS is also appropriate for measuring the Zeta potential in non-polar solvents as well as polar solvents.

4.2.5 Characterisation of Particles by Diameter and Zeta Potential

To confirm the size of the particles as measured in [11], and also verify that the new solvent did not affect properties of the particles, the diameter of the particles was measured. The zeta potential was also measured to characterise stability. The size and zeta potential measurements were performed with a Malvern Zetasizer [27], which operates by dynamic light scattering for size measurements, and PALS for Zeta potential measurements. Both Z-average and number average were recorded, as shown in Table 4.2 below.

	SRB-288		SRB-383		
Solvent	Water	Hexane	Water	Hexane	Water*
Z-Average Diameter (nm)	500	570	570	1050	2870
Number Average Diameter (nm)	420	530	450	800	500

Table 4.2. Particle sizes (*: after dispersal in hexane, evaporation of hexane and re-dispersal in water).

Although there is a discrepancy between the Z-average and the number average, the Z-average would be expected to be larger if a peak at a much higher diameter was found (e.g. if aggregates or large contamination was found in the sample). In such a case, the number average may be more representative of the sample. The zeta potential, a measure of stability, was also measured for both particle types in water. The zeta potentials are recorded in Table 4.3 below.

	SRB-288	SRB-383
Zeta Potential (mV)	-44	-50
Standard Deviation (mV)	4	6

Table 4.3. Zeta potential measurements conducted in water.

The zeta potentials are >± 40 mV, suggesting very good stability, though the stability is not necessarily as high in solvents other than water.

4.3 Methods

4.3.1 Making Solutions

Unless otherwise specified, particles were added to the liquid crystal 5CB at a wt /wt concentration of 1 %. The solutions were made by weighing the particles on a Mettler Toledo microbalance and adding n-hexane to make 500 mg/µl solution, adding the solution to 5CB and evaporating the solvent at room temperature overnight. The dispersions were sonicated for at least 30 minutes before adding to the LC mixture. Finally, the solvent was evaporated under a fume hood at room temperature. The error in concentration was approximately 1 % (i.e. an error of ± 0.01 % for 1 % wt/wt percentage).

4.3.2 Transition Temperatures

Transition temperatures were measured by observing the isotropic-nematic transition temperatures under 10 x magnification, both on heating and cooling. The main source of error was human error in identifying transition onset, 0.1 °C or above. The samples for transition temperature measurements were made by filling planar-aligned, 5 µm spaced Linkam cells, filled by the capillary method.

4.3.3 Dielectric Constants and Elastic Constants

10 μm planar cells[2], filled by the capillary method were made. The capacitance $C(V)$ was measured at 1 kHz over a range of 0.1 V - 20 V, also over a range of temperatures (Linkam TMS 94 hot stage with precision of ± 0.1 °C). The input dielectric constants were calculated by measuring the capacitance C over the same range and dividing by the empty cell capacitance, C_0:

$$\varepsilon(V) = \frac{C}{C_0}. \qquad \text{Eqn. 4.7}$$

Both C and C_0 were measured on an Agilent E4908A Precision LCR Meter, with an error of ±1pF based on stray capacitance of the electrodes connecting the cell to the bridge.

To find the elastic constants, and the parallel and perpendicular parts of the dielectric constants, a fitting program was employed. The fitting program [28] has been used successfully in the literature to calculate elastic and dielectric constants of liquid crystals to a ± 5 % accuracy [29]. The fitting program consists of two parts. One part predicts the shape of the dielectric permittivity $\varepsilon(V)$ as a function of applied voltage. The second part fits the experimental results to the predicted model. The part that predicts the dielectric permittivity is based on minimising free energy of the liquid crystal layer, taking into account the elastic contribution (Eqn. 2.10), electric contribution (Eqn. 2.11) and director profile. Since the director changes throughout the layer, and it is not known, variational calculus is used [30].

4.3.4 Refractive Index and Order Parameter

Ordinary and extraordinary refractive indices were measured on an Abbe refractometer (Bellingham and Stanley), with a ± 0.0002 error associated with each refractive index. An alignment layer of lecithin was deposited on the surface of the prism before measurement to promote homeotropic alignment of the liquid crystal between the prisms.

[2] Manufactured by AWAT, Poland

The refractive indices were used to calculate the birefringence and the order parameter was calculated using the Vuks relation [31]:

$$S = (1 - T/T_{NI})^{\gamma_{vuks}}, \qquad \text{Eqn. 4.8}$$

where $\boldsymbol{\gamma_{vuks}}$ is a dimensionless constant, and the Haller relation:

$$S\left(\frac{\Delta\alpha}{\alpha}\right) = \frac{n_e^2 - n_o^2}{\langle \bar{n}^2 \rangle - 1}, \qquad \text{Eqn. 4.9}$$

where α is the molecular polarizability of the liquid crystal and $\Delta\alpha$ is the anisotropy of the polarizability. Creating a Haller plot [32], i.e. plotting the right hand side of Eqn. 4.8 against the right hand side of Eqn. 4.9 on a log-log scale allows S to be calculated.

4.4 Results

4.4.1 Choosing a Concentration of Particles

Three concentrations of spherical particles (SRB-288) in 5CB, 1%, 2% and 3% were made. Under magnification, <1 day after construction, the samples were observed to determine if aggregation was present. No significant aggregation could be seen at 1% concentrations and under. It should be noted that it was not known whether some aggregation was present under 1% concentration, due to the small size of the particles: in future similar experiments, using fluorescent particles could provide more certain information. Neither individual particles, nor any possible associated defects, were visible at a magnification of 80 x. Also, the fact that not only were individual particles not visible, but no defects were seen, suggests that the particles may be in the weak anchoring regime.

4.4.2 Transition Temperatures

The nematic-isotropic transition temperature T_{NI} might be expected to fall with the addition of particles, assuming the particles cause a significant drop

in the order parameter, similar to the result found by Hourri et al [9]. In the systems studied in this thesis, the transition temperatures measured appear to show a small rise in with increasing particle concentration (Table 4.4). In considering whether this small (but apparently systematic change) is significant, it is first of all important to consider the uncertainties associated with measuring transition temperatures. The microscope hot stages used have a relative accuracy of 0.1˚C, but an absolute accuracy of only 1˚C. Hence, using a different hot stage could easily account for the small differences seen. However, this can be ruled out as care was taken to use the same hot stage in all of the measurements and variation in measurements of the transition temperatures is reflected in the standard deviations quoted in table 4.4. Indeed, all of the measured values are within one standard deviation of each other, and so are in agreement. Nonetheless, because of the small, systematic increase, it is important to rule out contamination of the 5CB that could occur on adding the colloidal particles. Solvent contamination would always cause a reduction in the transition temperatures, and so can be ruled out. Clearly, the rise in transition temperature is unlikely to occur as a consequence of the additional defects contained (associated with particles); these have lower order than regions in the bulk (e.g. the centre of a defect has order parameter S = 0) and so would cause a reduction in the transition temperatures. With a wt/wt concentration of particles at 5%, Petrov and Terentjev [33] produced an unusual composite material which showed a transition similar to the nematic-isotropic transition, which was ≈1°C. Given the various possibilities, it is reasonable to conclude that the small differences in transition temperatures of the three samples are simply statistical in nature. Nonetheless, in all measurements that follow, T_{NI} was recorded for each experiment and data are presented as a function of the difference, T_{NI}-T, to calibrate against the phase transition temperature and to take account of absolute temperature differences in different sets of apparatus.

Particle concentration (wt/wt) SRB-288	T_{NI} (°C)	Standard deviation (°C)
0%	34.7	0.3
1%	35.1	0.4
3%	35.3	0.1

Table 4.4 Transition temperatures as a function of particle concentration.

4.4.3 Dielectric Constants and Elastic Constants

Dielectric constants were measured for mixtures of 1% SRB-288 in 5CB and 1% SRB-383 in 5CB, as well as pure 5CB. The dielectric constants $\varepsilon_{\parallel}$ and $\varepsilon_{\perp}$ (parallel and perpendicular to the director respectively) were plotted as a function of reduced temperature, $T_{red} = T - T_{NI}$. The T_{NI} substituted was as measured in section 4.3.2**,** assuming both mixtures with particles SRB-288 and SRB-383 had the same T_{NI}.

The measured dielectric constants followed the expected form (Fig. 4.3), approaching each other as the temperature approached T_{NI}. The measurement for 5CB agreed within 10% of literature values [34]. When the three different mixtures were compared, there appears to be a fall in $\varepsilon_{\parallel}$ for SRB-288.

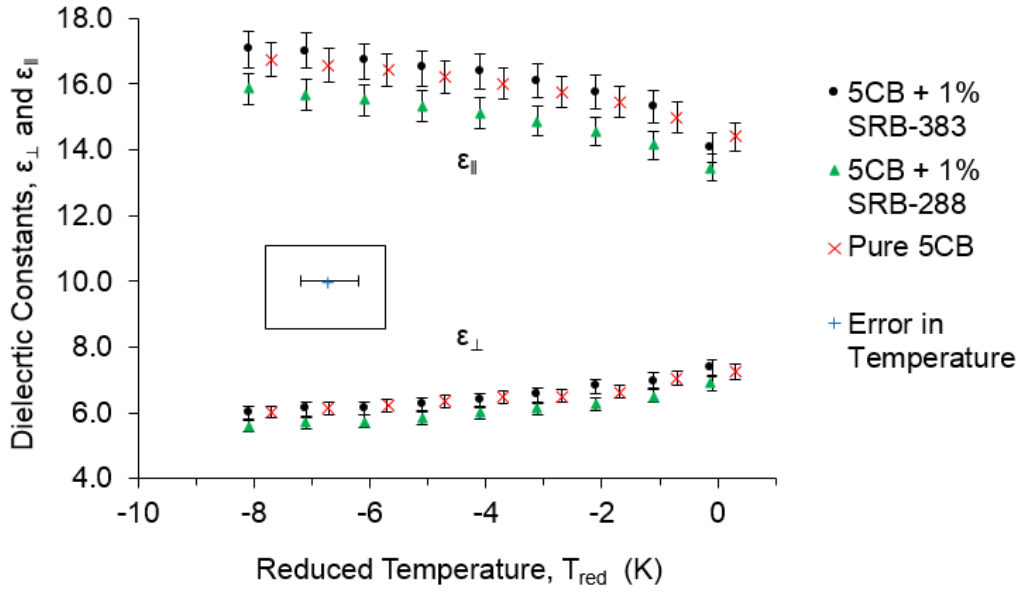

Fig. 4.3. Dielectric constants as a function of temperature

However, the vertical error bars only consider the error in measurements of the dielectric constants, arising mostly from stray capacitance in the electrodes. If the error in temperature (which depends on reduced temperature) is taken into consideration, the curves may be shifted in temperature up to ± 0.5°C. If that is the case, the results may overlap each other within the error bars. With the error taken into account, there is no good evidence of a difference in dielectric constants.

The splay (Fig. 4.4) and bend (Fig. 4.5) elastic constants, with or without taking the error in temperature into account, did not suggest any change in the elastic constants within the margin of error.

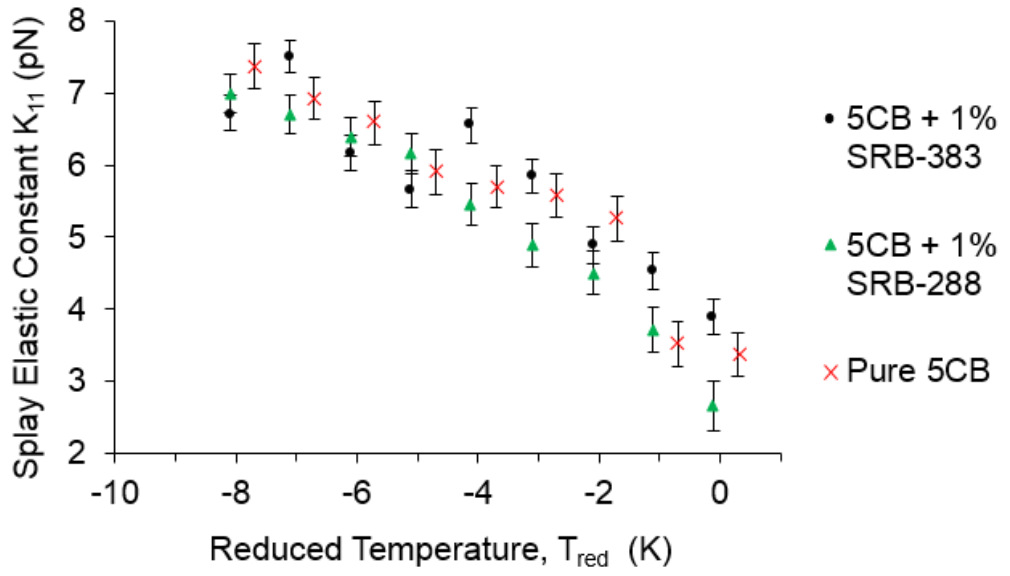

Fig. 4.4 Splay elastic constants as a function of temperature

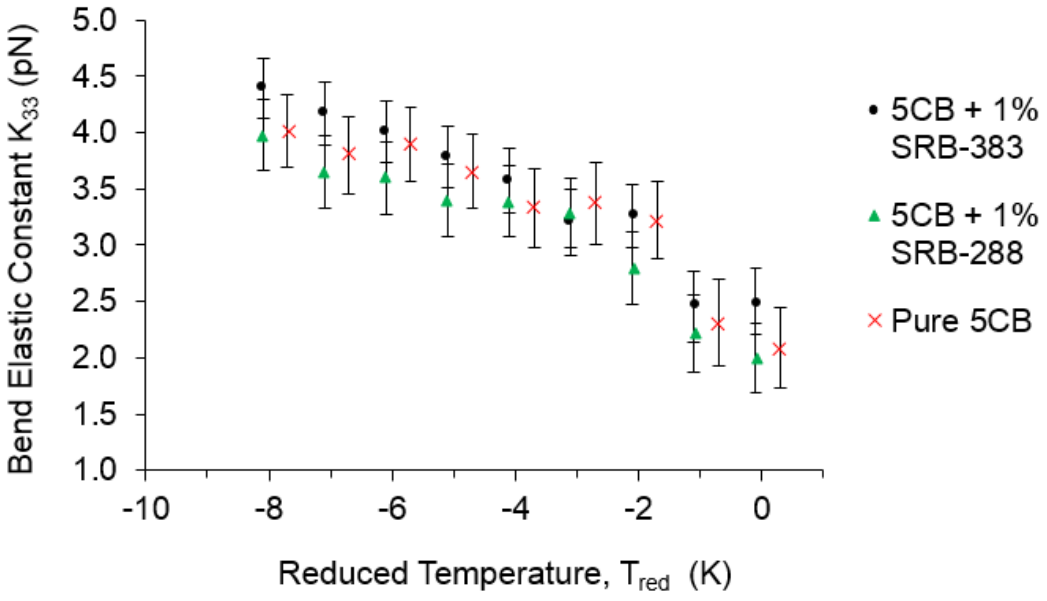

Fig. 4.5. Bend elastic constants as a function of temperature

In conclusion, if there is a change in the dielectric properties or bend and splay elastic constants at this concentration, this change is smaller than the error in the measurements. For the next set of measurements, only one particle type was studied, choosing to study properties that can be measured

to a high degree of sensitivity to determine if a smaller change in physical properties can be detected.

4.4.4 Refractive Indices and Order Parameter

The refractive indices and order parameter were measured for 1% concentration of SRB-288 in 5CB, and for pure 5CB.

The ordinary refractive index (Fig. 4.6) showed no difference within the error.

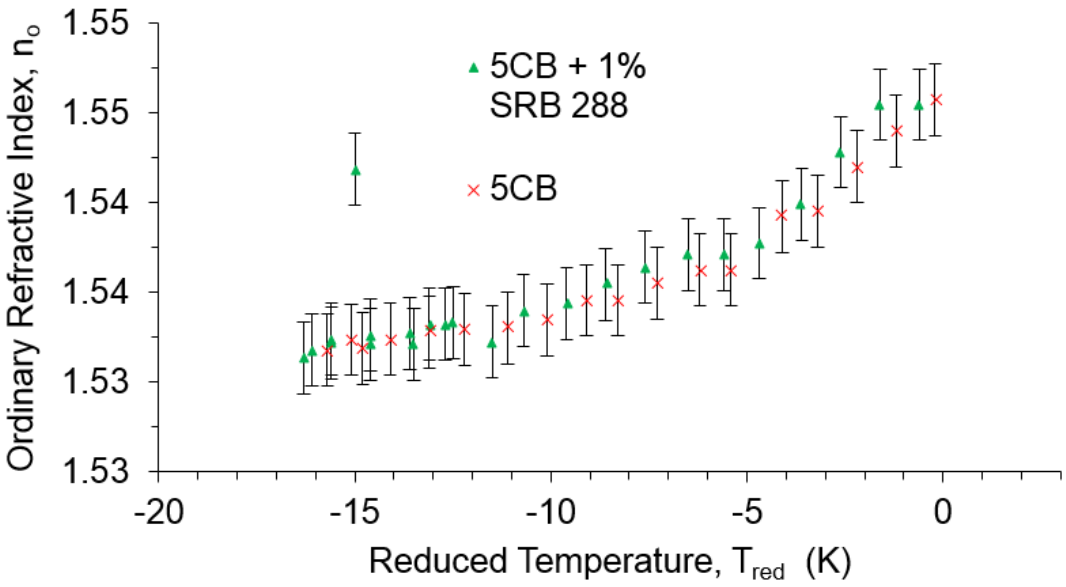

Fig. 4.6. Ordinary refractive index as a function of temperature. Note that the outlier was not used in the fitting for calculating the order parameter.

However, the extraordinary refractive index (Fig. 4.7) appears to show a significant difference between the pure 5CB and the mixture once within ~10° of the nematic-isotropic transition. Again, the uncertainty in the transition temperatures (or specifically, the difference in transition temperatures) means that the difference could be explained by that, so it can't be concluded that there is a significant difference.

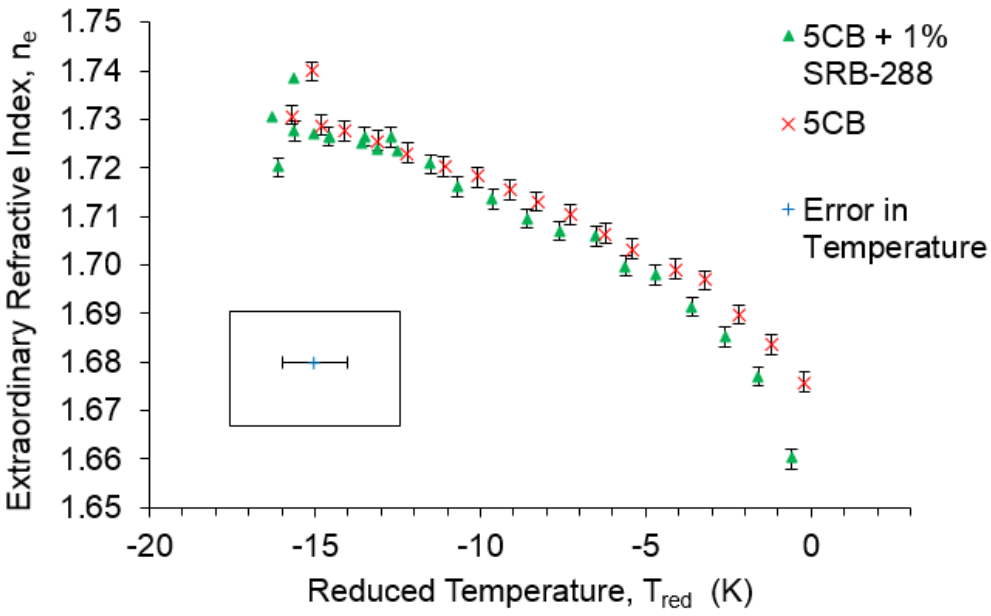

Fig. 4.7 Extraordinary refractive index as a function of temperature

The order parameter measurement (Fig. 4.8) showed no significant difference in the pure 5CB and with 1% SRB-388.

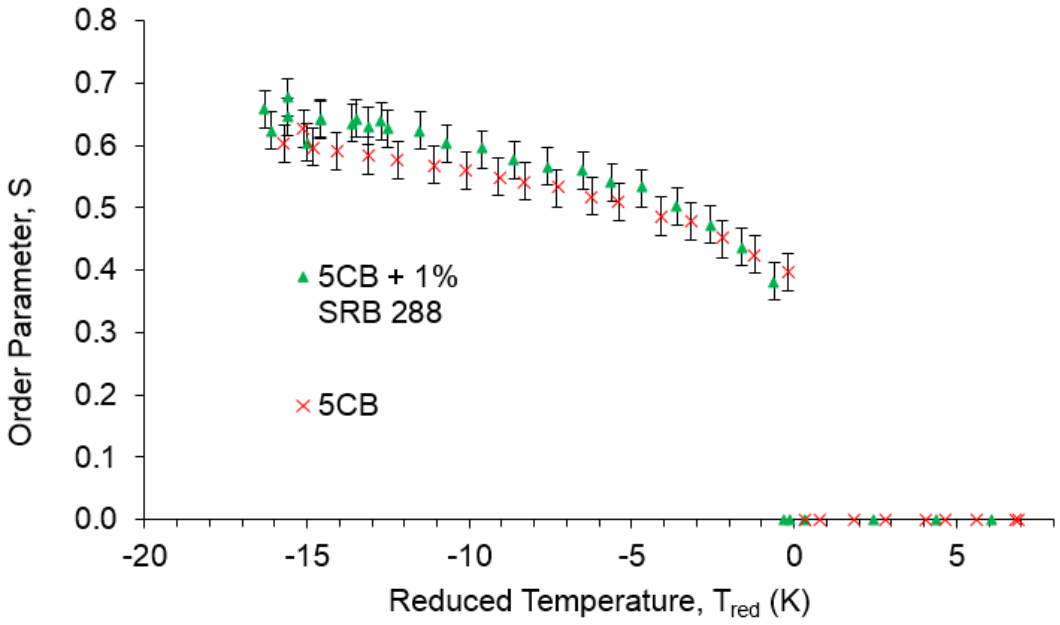

Fig. 4.8. Order parameter as a function of temperature

The measurements of refractive index and order parameter for 5CB were consistent with literature. There could be no conclusion of any measurable effect on refractive indices or order parameter by adding the particles at a concentration of 1%.

4.5 Discussion and Conclusion

We chose to study submicron particles at concentrations low enough that most particles are likely to be dispersed in the sample (as opposed to the very high concentrations >50% studied by Meerker et al [10]), in this case, 1% and below. No significant effect could be found on any of the physical properties (dielectric constants, elastic constants, refractive indices and order parameter) measured within the systematic errors present within the measurements. Adding dielectric particles at lower concentrations into a device is unlikely to affect the device performance significantly.

It is clear that aggregation is a concern when working with particles. Aggregation is difficult to prevent in liquid crystal colloids [35]. In some colloidal systems, it is possible to avoid aggregation with the use of

surfactants. However, in liquid crystal colloids, thermal stability may only be possible in special cases such as <10 nm particles, with highly specialised surfactants [36]. The elastic interaction energies in LC colloids are high (>1000 k_BT/e).

While conducting the research above, it was also found that when particles are similar to or smaller than the wavelength of light, if difficult to draw conclusions about the location of the particles within the sample (whether they are aggregated, even whether they have been drawn into the centre of the cell). From the Rayleigh criterion (Eqn. 1.10), with a high numerical aperture lens (e.g. the 100x lens in chapter 3 has NA=1.3) is just possible to resolve particles of 200-300 nm in diameter:

$$r_{limit} = \frac{0.61\lambda}{NA}, \qquad \text{Eqn. 4.10}$$

and it is possible to resolve smaller particles by dark field microscopy [36], or specialised fluorescence techniques, which will be discussed in chapter 8.

In the upcoming chapters, the research will have a different focus. First, particles that will be studied will be 5 μm in diameter or larger: at this scale, location and surface alignment can be easily identified under a polarising microscope. Second, instead of studying bulk properties, the interactions of individual particles with defects will be investigated.

References

1. I. Dierking, G. Scalia, and P. Morales, Journal of Applied Physics **97**, 1 (2005).

2. S.-Y. Lu and L.-C. Chien, Optics Express **16**, 12777 (2008).

3. M. Rahman and W. Lee, Journal of Physics D: Applied Physics **42**, 63001 (2009).

4. S. P. Yadav and S. Singh, Progress in Materials Science **80**, 38 (2016).

5. M. Inam, G. Singh, A. M. Biradar, and D. S. Mehta, AIP Advances **1**, 0 (2011).

6. L. Cseh and G. H. Mehl, Journal of Materials Chemistry **17**, 311 (2007).

7. M. Mishra, R. S. Dabrowski, J. K. Vij, A. Mishra, and R. Dhar, Liquid Crystals **42**, 1580 (2015).

8. S. Al-Zangana, M. Iliut, M. Turner, A. Vijayaraghavan, and I. Dierking, Advanced Optical Materials **4**, 1541 (2016).

9. A. Hourri, T. K. Bose, and J. Thoen, Physical Review E **63**, 051702 (2001).

10. S. Meeker, W. C. K. Poon, J. Crain, and E. M. Terentjev, Physical Review E **61**, R6083 (2000).

11. S. Butterworth, Shape and Chemical Anisotropic Particles in Low Dielectric Constant Media, University of Manchester, 2013.

12. H. R. Sheu, M. S. El-Aasser, and J. W. Vanderhoff, Journal of Polymer Science: Part A: Polymer Chemistry **28**, 629 (1990).

13. G. W. Gray, K. J. Harrison, and J. A. Nash, Electronics Letters **9**, 130 (1973).

14. C. M. Hansen, Progress in Organic Coatings **51**, 55 (2004).

15. C. M. Hansen, Progress in Organic Coatings **51**, 77 (2004).

16. W. B. Russel, D. A. Saville, and W. R. Schowalter, *Colloidal Dispersions* (Cambridge University Press, 1989).

17. W. I. Goldburg, American Journal of Physics **67**, 1152 (1999).

18. J. C. Thomas, Journal of Colloid and Interface Science **117**, 187 (1987).

19. J. H. Badley, Journal of Polymer Science Part C: Polymer Symposia **8**, 305 (2007).

20. B. Jachimska, M. Wasilewska, and Z. Adamczyk, Langmuir **24**, 6867 (2008)

21. W. Zhou, R. Apkarian, Z. L. Wang, and D. Joy, in *Scanning Microscopy for Nanotechnology* (Springer, 2006), pp. 1–40.

22. L. Herbowski, H. Gurgul, and W. Staron, Zeitschrift Für Medizinische Physik **19**, 189 (2009).

23. K. Bohinc, V. Kralj-Iglič, and A. Iglič, Electrochimica Acta **46**, 3033 (2001).

24. K. K. Mahanta, G. C. Mishra, and M. L. Kansal, Applied Clay Science **59**–**60**, 1 (2012).

25. L. E. Drain, *The Laser Doppler Technique* (John Wiley & Sons, Ltd., 1980).

26. J. F. Miller, K. Schätzel, and B. Vincent, Journal of Colloid And Interface Science **143**, 532 (1991).

27. Malvern ZetaSizer Nano Specification, Malvern Instruments, (2004).

28. *Fredhybridpreepsfit* (Matlab Code), P. Brimicombe, University of Manchester (2011).

29. S. Kaur, J. Addis, C. Greco, A. Ferrarini, V. Görtz, J. W. Goodby, and H. F. Gleeson, Physical Review E - Statistical, Nonlinear, and Soft Matter Physics **86**, 1 (2012).

30. K. R. Welford and J. R. Sambles, Molecular Crystals and Liquid Crystals **147**, 25 (1987).

31. M. F. Vuks, Optics and Spectroscopy **20**, 361 (1966).

32. I. Haller, Progress in Solid State Chemistry **10**, 103 (1975).

33. P. G. Petrov and E. M. Terentjev, Langmuir **17**, 2942 (2001).

34. A. Bogi and S. Faetti, Liquid Crystals **28**, 729 (2001).

35. F. Mondiot, R. Botet, P. Snabre, O. Mondain-Monval, and J.-C. Loudet, Proceedings of the National Academy of Sciences **111**, 5831 (2014).

36. M. F. Prodanov, N. V. Pogorelova, A. P. Kryshtal, A. S. Klymchenko, Y. Mely, V. P. Semynozhenko, A. I. Krivoshey, Y. a. Reznikov, S. N. Yarmolenko, J. W. Goodby, and V. V. Vashchenko, Langmuir **29**, 9301 (2013).

37. A. V. Ryzhkova, M. Škarabot, and I. Muševič, Physical Review E **91**, (2015)

Chapter 4. Effect of Submicron Spheres and Janus Particles on a Nematic Liquid Crystal

.

Chapter 5 Particle Tracking and Features of Particle Trajectories of Mean Square Displacement Data

5.1 Introduction

In chapter 4, we investigated the bulk properties of a liquid crystal with the addition of microparticles. Given the results of chapter 4, which found particles to aggregate, we decided to study how the position of particles can be controlled by defects In chapter 3, we introduced the principles behind laser tweezing and particle tracking, which will be used to study the motion of particles near to defects in a liquid crystal. Here, we discuss our fitting methods and some features of positional data obtained with the particle tracking system. The chapter opens with an explanation of how the form and values of mean square displacement reflect the physical properties of a system of a particle suspended in a liquid or liquid crystalline medium. The MSD of a freely diffusing particle can be analysed to calculate the viscosity of the medium, and the MSD of a confined particle allows the quantification of confinement strength. Some other features may contribute to the mean square displacement that do not relate to the viscosity or confinement strength. This includes drift and other fluctuations. The procedure of analysis outlined here will inform the results and conclusions in chapter 6.

5.2 The Mean Square Displacement of Freely Diffusing and Confined Particles

In chapter 2, we outlined some physics behind the hydrodynamics of particles in liquid crystals. Applying the theory under that gives us some predictions for the form a particle's trajectory would take in a liquid crystal. From the trajectory, the MSD can be calculated. Let us consider a system consisting of a particle suspended in a fluid.

First, consider a particle that is diffusing freely under Brownian motion. In chapter 2, the viscosity in liquid crystals was shown to be anisotropic. In certain geometries, the viscosity 'experienced' by a particle travelling in a given direction corresponds to one of the Miesowicz viscosities η_i, but more generally, the viscosity will be a combination, η_i^{diff}, of Miesowicz viscosities. Stokes' law is therefore:

$$\xi_i = 6\pi\eta_i^{diff} a, \qquad \text{Eqn. 5.1}$$

for spherical particles in the low Reynolds number[3] regime (Stokes' law holds within ≤1% when $Re < 0.1$ [1]). Because the shear rate is low for low Reynolds numbers, the diffusion rate does not depend on whether the fluid is Newtonian or non-Newtonian.

It can be shown that the mean square displacement for a particle undergoing Brownian motion is linear in t:

$$\langle \left(R_i(t)\right)^2 \rangle = \frac{2k_B T}{\xi_i} t. \qquad \text{Eqn. 5.2}$$

From the gradient, ξ_i can be calculated, and therefore calculate viscosity. In Fig. 5.1, we see a representation of an MSD of a particle undergoing Brownian motion as described in Eqn. 5.1).

[3] Reynolds number is defined for a sphere travelling in a fluid as $Re = \frac{avp}{\eta}$.

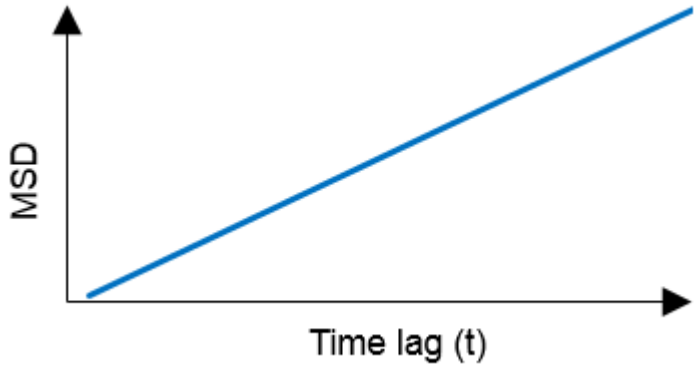

Fig. 5.1. The mean square displacement of a particle undergoing Brownian motion is linear.

Conversely, a particle that is highly confined by e.g. a laser trap should have a constant MSD:

$$\langle \left(R_i(t)\right)^2 \rangle = \frac{2k_B T}{\kappa_i}. \qquad \text{Eqn. 5.3}$$

From the value of $\langle \left(R_i(t)\right)^2 \rangle$, the 'spring constant' κ_i can be calculated. Plotting Eqn. 5.3 gives us the plot in Fig. 5.2 below.

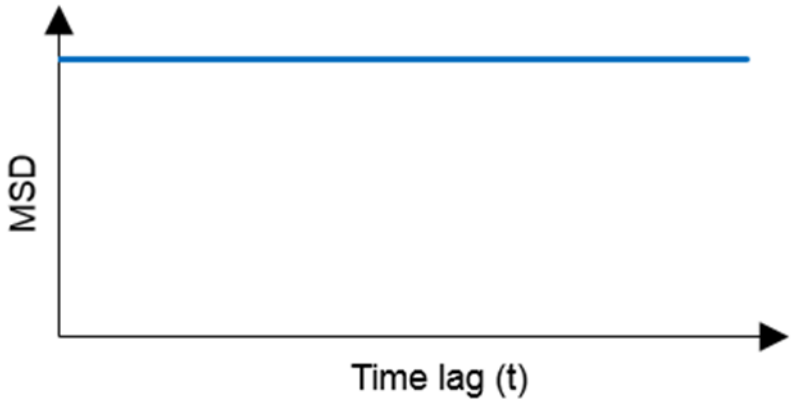

Fig. 5.2. The MSD of a highly confined particle should be constant.

The two cases (freely diffusing and confined) discussed above are described together by:

$$\langle \left(R_i(t)\right)^2 \rangle = \frac{2k_B T}{\kappa_i}\left[1 - \exp\left(-\frac{\kappa_i t}{\xi_i}\right)\right]. \quad \text{Eqn. 5.4}$$

The equation is taken from the case of a particle trapped in a potential well of a laser trap [2]. The MSD can be expected to follow the form shown below in Fig. 5.3.

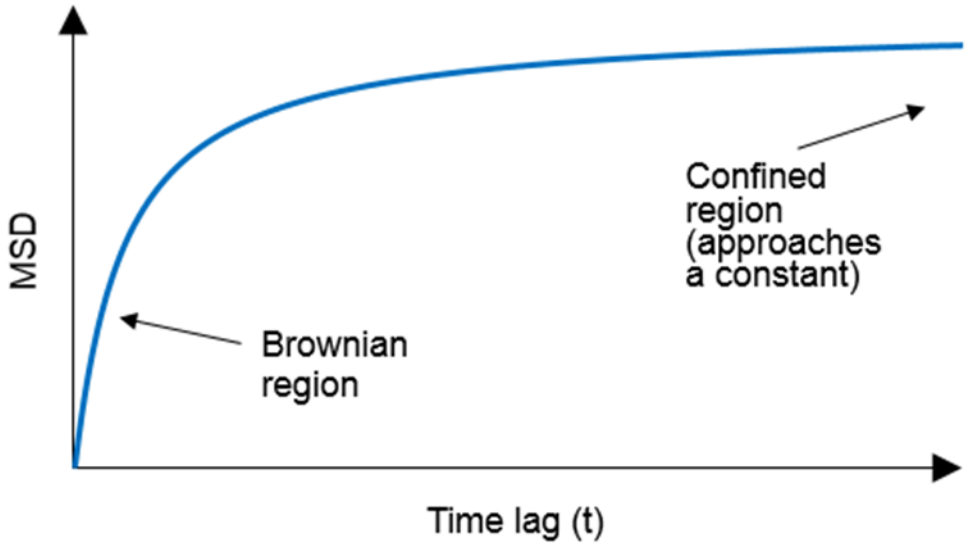

Fig. 5.3. MSD of a particle that diffuses freely at short timescales, and is confined at longer timescales (note: scales are log scales).

It can be shown that the limiting cases of Eqn. 5.4 give us Eqn. 5.1 and Eqn. 5.3, at short and long timescales respectively. To calculate what the limiting cases are, we can approximate Eqn. 5.4 by using a Taylor expansion (or more specifically, a Maclaurin expansion, since the expansion will be performed around $t = 0$). The Maclaurin expansion for e raised to the power x is given by:

$$e^x = \sum_{i=0}^{\infty} \frac{x^i}{i!} = 1 + x + \frac{x^2}{2!} + \frac{x^3}{3!} .... \quad \text{Eqn. 5.5}$$

where i is an integer.

If we apply this expansion to the exponential term in Eqn. 5.4, the term approximates to:

$$\exp\left(-\frac{\kappa_i t}{\xi_i}\right) = 1 - \frac{\kappa_i t}{\xi_i} + \frac{1}{2}\left(\frac{\kappa_i t}{\xi_i}\right)^2 \ldots \quad \text{Eqn. 5.6}$$

As t→0, the terms in Eqn. 5.7 of order 2 and above become negligible compared to the previous terms. Therefore Eqn. 5.8 approximates to:

$$\exp\left(-\frac{\kappa_i t}{\xi_i}\right) \approx 1 - \frac{\kappa_i t}{\xi_i}. \quad \text{Eqn. 5.7}$$

Eqn. 5.7 can then be substituted back into Eqn. 5.4, which gives us:

$$\langle\left(R_i(t)\right)^2\rangle \approx \frac{2k_B T}{\kappa_i}\left[1 - \left(1 - \frac{\kappa_i t}{\xi_i}\right)\right]. \quad \text{Eqn. 5.8}$$

Eqn. 5.8 can be simplified further to give:

$$\langle\left(R_i(t)\right)^2\rangle \approx \frac{2k_B T}{\kappa_i}\left[\frac{\kappa_i t}{\xi_i}\right] = \frac{2k_B T}{\xi_i} t, \quad \text{Eqn. 5.9}$$

which is identical to equation Eqn. 5.1.

For the case of long timescales, we can use knowledge of exponential functions to give an approximation for Eqn. 5.4. We know that for an exponential function $\exp(-x)$, as $x \longrightarrow \infty$, $\exp(-x)$ becomes very small, as $\exp(-x) = (\exp(x))^{-1} = 1/\exp(x)$. This means that the term $\exp\left(-\frac{\kappa_i t}{\xi_i}\right)$ in Eqn. 5.4 can be neglected. Therefore, Eqn. 5.4 approximates to:

$$\langle\left(R_i(t)\right)^2\rangle \approx \frac{2k_B T}{\kappa_i}, \quad \text{Eqn. 5.10}$$

which is the same as Eqn. 5.3. The full equation, Eqn. 5.3 takes account of both of these regimes.

Finally, note that all equations between Eqn. 5.1 and Eqn. 5.3 are given for the 1D regime (for the i^{th} component x, y or z). For the 2D and 3D cases, the total mean square displacement is given by:

$$\langle\left(R_{2D}(t)\right)^2\rangle = \frac{4k_B T}{\kappa_i}\left[1 - \exp\left(-\frac{\kappa_i t}{\xi_i}\right)\right] \quad \text{Eqn. 5.11}$$

for 2 dimensions, and

$$\langle \left(R_{3D}(t)\right)^2 \rangle = \frac{6T}{\kappa_i}\left[1 - \exp\left(-\frac{\kappa_i t}{\xi_i}\right)\right] \quad \text{Eqn. 5.12}$$

for 3 dimensions.

5.3 Methods of Fitting: Linear vs. Exponential

There are two alternative methods of finding the constants in Eqn. 5.4. by fitting. The first, as was used to analyse data in chapter 6, was to fit the confined region and the Brownian region separately as straight lines. The function used in the custom software to fit the data was from the SciPy [5] library (scipy.stats.linregress) which calculates the best fit by a least squares method. Most results, including details of analysis, will be discussed in chapter 6.

The second method is to fit the whole function shown in Eqn. 5.4. To compare this method, we tested the fitting on some data from a 5 µm borosilicate particle confined at a defect in the liquid crystal MLC-6648 (see chapter 6 for more context). To fit the data, we used Origin's [6] built-in fitting functions. We chose to fit to an equation that corresponded to Eqn. 5.4. In this case the equation fitted was:

$$y = A_1 \exp\left(-\frac{\mathrm{x}}{t_1}\right) + y_0 \quad \text{Eqn. 5.13}$$

where y was the dependent variable, x was the independent variable, and the three constants A_1, t_1 and y_0 were constants (i.e. the fitting parameters). The algorithm used in Origin to fit that function was a Levenburg-Marquadt algorithm, an algorithm that minimises the least squares for non-linear functions, first published in 1944 [7].

Performing the fitting resulted in the curve shown in Fig. 5.4 below.

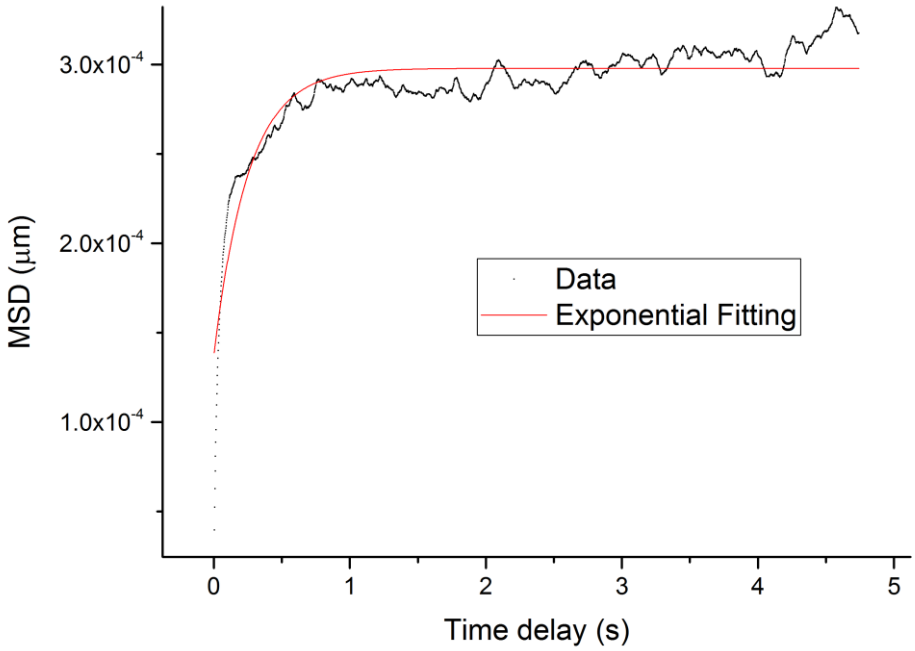

Fig. 5.4. Exponential fitting of MSD for x-component (1D case) of particle trapped at defect from chapter 6.

The above Eqn. 5.13 can be rearranged to take the same form as Eqn. 5.4.:

$$y = -A_1 * \left(\frac{-y_0}{A_1} - \exp\left(-\frac{\mathrm{x}}{t_1}\right)\right). \qquad \text{Eqn. 5.14}$$

This means that all the constants within Eqn. 5.4 can also be calculated. The fit in Fig. 5.4 gave a confinement strength (κ_i) of 43.9 pN with an error in fitting that parameter of 1%. When compared to the results of the linear fit, the results are similar, though larger than the error in fitting. The results for both fittings are shown in Table 5.1 below.

	Linear fit only	Exponential fit
Confinement strength κ_i (pN/μm)	44	51

Table 5.1 Comparison of confinement strength calculated from the same raw data, by linear fitting and exponential fitting.

The two results are still within the typical error of results in chapter 6 (above 25%).

In comparison, the two methods generate similar results not likely to make a significant difference to the results in chapter 6. However, the linear fit does fit to fewer parameters at once (only two as opposed to three).

5.4 Noise at Short Time Scales

Timescales under ~0.1 s often exhibit more noise than intermediate time scales. This is most likely because at these small timescales, as the frame rate is only ~100 μs, there are only a small number of data points that are in this region. A graph showing an example of the noise from the dataset examined in chapter 6 is shown in Fig. 5.5 below.

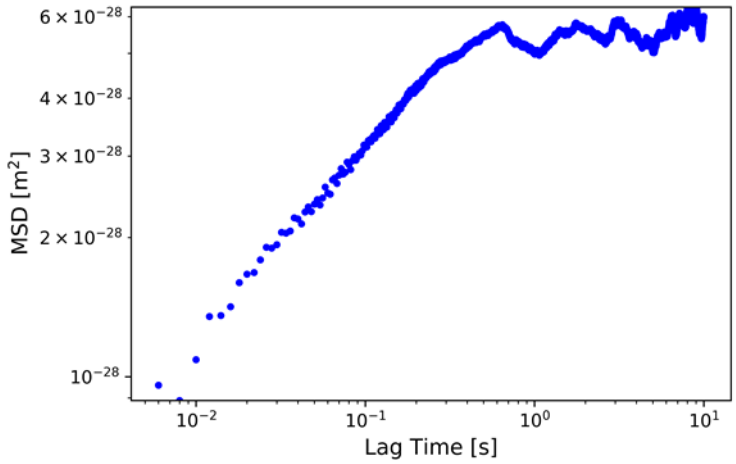

Fig. 5.5. At small timescales, under ~50 ms, few data points are present. (result is a component of particle confined at a line defect). This result is from a one-dimensional component of displacement only.

However, the error in linear fit is typically small compared to the error between repeated measurements, especially after the first ~5 data points.

5.5 Drop in MSD at long time scales [2,3]

At much longer timescales (typically >10 s), a more unexpected feature was identified in some datasets. The feature consisted of fluctuations, or a large drop, in MSD at long timescales. An example of the fall in MSD observed in the dataset from chapter 6 is seen in Fig. 5.6 below.

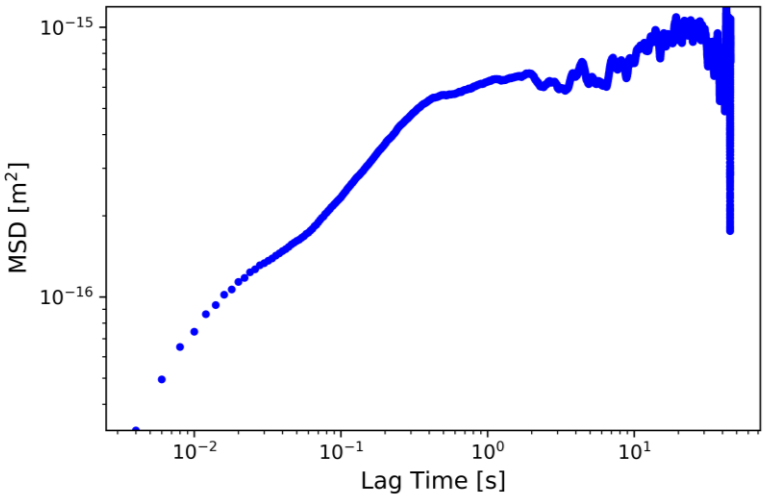

Fig. 5.6. A drop in MSD was sometimes observed at timescales typically above 100 s. At shorter timescales, the MSD appears to behave as expected for a freely diffusing/partially confined particle.

No consistency was found in when this feature appeared. The feature could appear on some MSDs of the same particle confined at the same defect, and not on others. A physical interpretation of the drop in MSD suggests that at long timescales, the particles have moved a shorter distance from the origin than at earlier timescales. There are a few plausible explanations, due to either a physical mechanism, or the frame rate and tracking system.

5.6 Drift

'Drift' in particle tracking experiments refers to relative motion of particles to the camera; specifically, motion that is independent of the physical properties of the particle or the medium. An example of drift might be the hot sample moving relative to the hot stage: the motion does not reveal anything about the rheology within the sample, yet will still be present in any raw particle tracking data. To illustrate what types of motion may be involved in the tracking data, a diagram has been provided in Fig. 5.6 below.

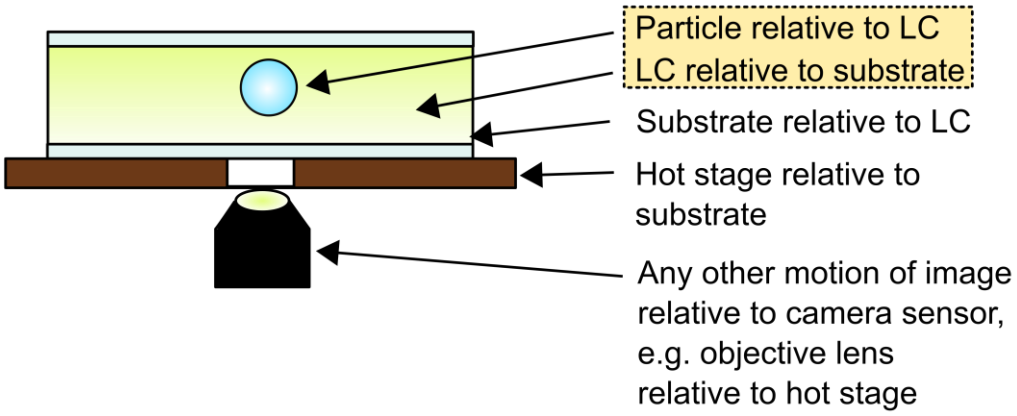

Fig. 5.7. Schematic diagram representing cross-section of a sample, with some possible causes of drift. In box with dotted line is motion that allows physical properties of particle and medium to be investigated.

Considering timescales can allow some types of drift to be eliminated with some confidence. Motion that occurs only at timescales of ≥1 s is likely to be caused by drift (visible as a rise in MSD at long timescales in Fig. 5.8 a). Since the timescales of drift are comparable with the whole time period of measuring the particle's motion (~100 s), drift correction often starts with looking at the trajectory of the particle over the whole time period. If the motion is linear, a linear fit can be performed over the whole trajectory, and then subtracting the drift as a baseline. When the drift was not linear, a Savitsky-Golay filter [4] was applied instead. A Savitsky-Golay filter performs a convolution to smooth data at a desired scale (in this case, ~10 s or above). An example of data from chapter 6 before and after drift correction can be seen in Fig. 5.8 below.

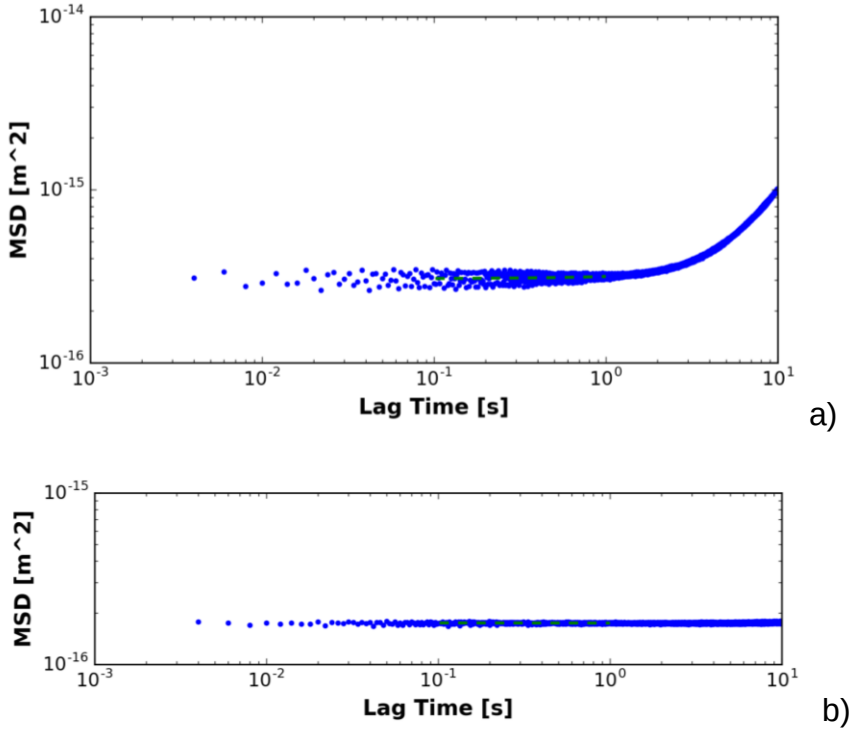

Fig. 5.8. The mean square displacement of a particle stuck to the inner surface of a sample before and after drift correction. Note that drift only becomes apparent after ~1 s timescales or larger.

The amount of drift varied between samples. In most cases, correcting for drift made no difference within the margin of error: in these cases, drift was not accounted for in the results.

Related to drift is the possibility of a particle shifting from one location to another during the measurement period. Such cases were identified from the histograms of particle positions. In these cases, two instead of one peak were visible (Fig. 5.9 below).

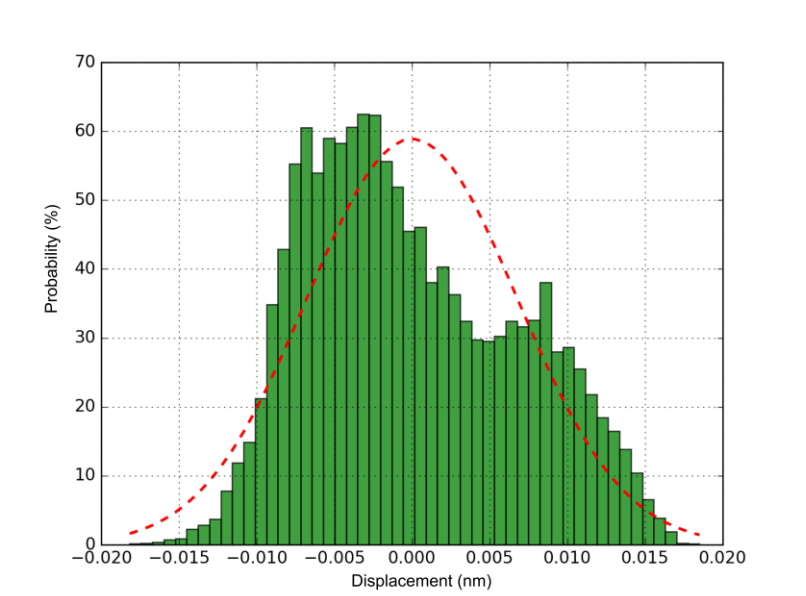

Fig. 5.9. Histogram of particle displacement, showing two peaks. The plot suggests a shift in position has occurred at some time over the measurement period.

A single displacement as discussed above can be confirmed by plotting the displacement as a function of position and time. In this case, the dataset can be split into before and after the displacement and analysed as normal.

The profile of the histogram in Fig. 5.9 [now Figure 1.9?) can be seen to be approximately the sum of two Gaussian distributions. A normal distribution (i.e. Gaussian profile) of probability densities $\rho(r)$ is given by:

$$\rho(r) = \frac{1}{\sqrt{2\pi\sigma^2}} \exp\left(-\frac{(r - r_{mean})^2}{2\sigma^2}\right) \qquad \text{Eqn. 5.15}$$

where σ is standard deviation, and r_{mean} is the mean of the distribution. If one sums together two normal distributions with different means appears consistent with the profile observed in Fig. 5.9. The mean corresponds to the x displacement of the peaks.

The profile of the data from Fig. 5.9 can be fitted with two Gaussian distributions. The algorithm used was also within Origin [6], designed to fit one or more Gaussian distributions. The algorithm also uses the Levenburg-Marquadt method. In this case, each peak is fitted to the following equation:

$$y = y_1 + \frac{A_2}{w\sqrt{\pi/2}} \exp\left(\frac{-2\left((x - x_c)\right)^2}{w}\right), \qquad \text{Eqn. 5.16}$$

where the fitting parameters are y_2, A_2, w and x_c.

We took the raw data from Fig. 5.9 and created a histogram before normalisation, with a profile of the same shape. The heights of the bins were used as the y coordinates for the fitting. We also constrained the fitting so that $y_1 = 0$ (as there should not be a baseline). Results of the fitting are shown in Table 5.2 and Fig. 5.10 below.

	x_c (μ)	w (μ^{-2})	A_2 (μ^2)
Peak 1	8.8270 ± 0.0003	0.00821 ± 0.0004	14 ± 1
Peak 2	8.8287 ± 0.0006	0.010 ± 0.001	8 ± 1

Table 5.2. Results of fitting data from Fig. 5.9 before normalisation, including standard error from fitting.

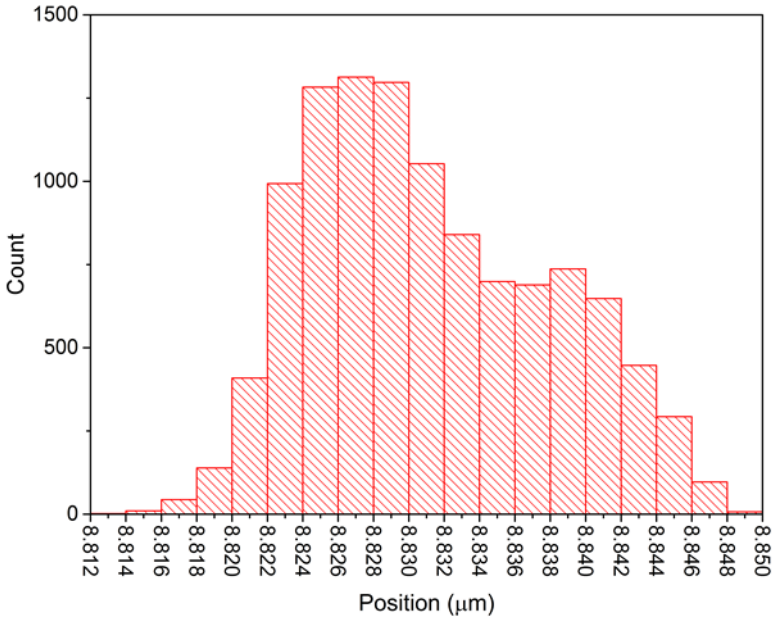

a)

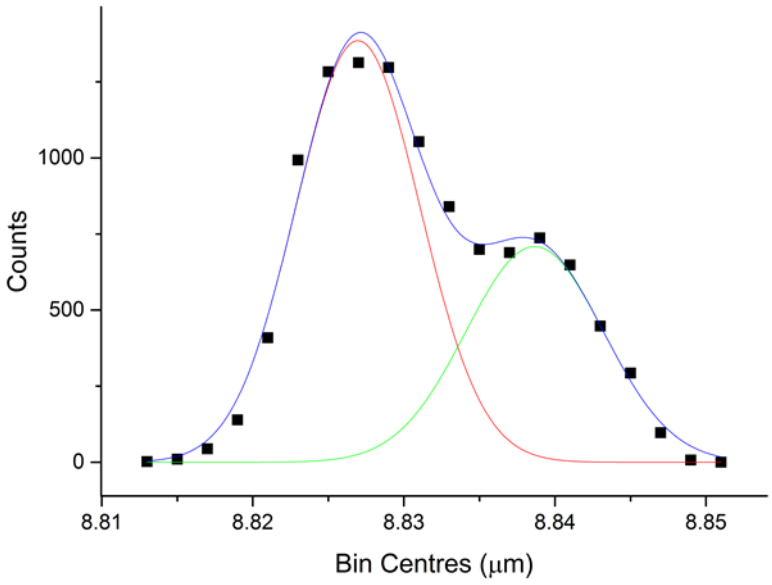

b)

Fig. 5.10. a) profile of histogram of raw data before normalisation from Fig. 5.9. The heights of the centres of the bins were fitted to produce b). double Gaussian fit of profile of a).

As can be seen from both Fig. 5.10 and the standard error in Table 5.2, the fitting converged and all parameters were fitted to within ~10%.

5.7 Spatial Artefacts

In some cases, plotting the positions of the particles sometimes revealed a regular pattern in the recorded displacement of the particles. The artefact was only observed when particles were confined to the surface of the glass substrate, and was most apparent after drift correction was applied. An example from the dataset taken for chapter 6, though not included in the results, is shown in Fig. 5.11 below.

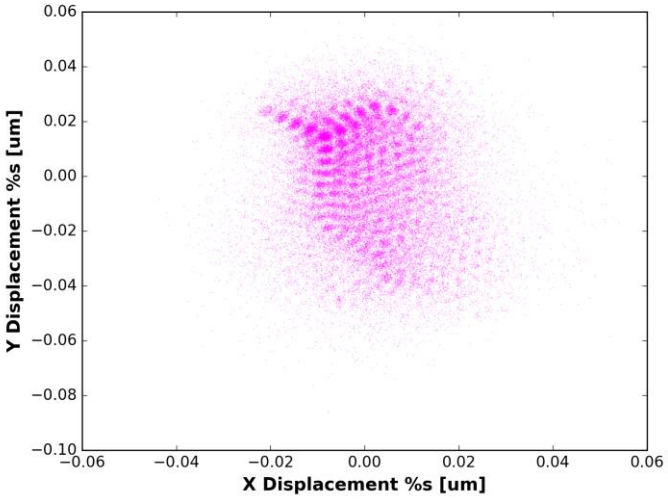

Fig. 5.11. Pattern observed in particle position.

While no cause was identified, this is likely to be an artefact due to the thresholding software, due to the regularity and symmetry of the pattern. Datasets containing this feature were not included in the final results for defect confinement strength.

5.8 Conclusion

Here we have discussed the form of MSD taken by freely diffusing and confined particles. Knowing the form expected allows MSDs obtained from particle tracking results to be evaluated critically. In the cases where the expected form is taken, the viscosity of the liquid crystal and trapping strength can be evaluated. Some features may not correspond to this model. In these cases, the cause may be related to the tracking system,

experimental setup, or some other physical occurrence. In the next chapter, some results of particle tracking will be presented. The contents of this chapter will help to inform the interpretation of results in the next chapter.

References

1. B. P. Le Clair, A. E. Hamielec, and H. R. Pruppacher, Journal of the Atmospheric Sciences **27**, 308 (1970).

2. M. Tassieri, *Microrheology with Optical Tweezers: Principles and Applications*, edited by M. Tassieri (Pan Stanford Publishing Pte., 2016)

3. G. M. Gibson, in (2007), pp. 1–32.

4. A. Savitzky and M. J. E. Golay, Analytical Chemistry **36**, 1627 (1964).

5. E. Jones, E. Oliphant, and P. Peterson et al, *SciPy: Open Source Scientific Tools for Python* (2001), http://www.scipy.org/.

6. OriginPro, Version 2016*,* OriginLab Corporation, Northampton, MA, USA.

Chapter 6 Quantifying the Strength of Confinement of Particles at Defects in Nematic Liquid Crystals

6.1 Introduction

Previously, we discussed the process of analysing the trajectory of a particle in a liquid crystal, and using that information to quantify:

- The viscosity of the fluid in a given direction, if the particle is diffusing freely.
- Trapping strength, if the particle is confined.

In particle tracking experiments in the literature, the 'trapping strength' κ is typically the strength of an optical trap (see chapter 3). In this chapter, we apply the same type of analysis to a different variety of trap, namely, a defect in a liquid crystal.

Microviscometry measurements can be divided into 'active' and 'passive' methods. Active methods depend on the strength of the laser trap. Active methods have been used in the literature to study properties of liquid crystals, for example, measuring viscosity [1,2]. However, the active methods are not appropriate when investigating another trapping system. This suggests the passive methods as more appropriate to investigate strength of trapping by defects.

One method that may be considered passive, in that it does not depend on the strength of the laser trap, can only be applied to line defects. In this method by Trivedi, Engström, and Smalyukh [3], the line defect is 'stretched' by a trap, and the defect energy calculated by the angle.

However, what if you want to investigate a system where the particles are already 'stabilised' at defects? The typical tweezing method, which requires $n_{particle}>n_{medium}$, may not be available, depending on particle type. The

alternative tweezing method sometimes used in liquid crystals, ‘local melting’ may be difficult to apply to systems with a melting point much higher than room temperature. For example, the nematic phases of known bent-core liquid crystals are above 100°C, with melting points above 200°C [4].

There is a precedent for using passive methods to measure properties of liquid crystals, for example, again using to investigate liquid crystal viscosity [1]. Another method is much more similar to the method applied in this chapter. In this case, the tracking begins with particles at a substantial distance (> 3 x particle diameter). After accounting for Brownian motion, the attractive force towards the centre of the defect can be quantified. This method was first used by Pires, Fleury and Galerne [5], which includes taking into account the radial symmetry of the defects. The method was then applied to some other systems (defects associated with other particles, more particle sizes) by Ryzhkova and Muševič [6].

In this chapter, we demonstrate how a method that does not depend on laser trapping may be used to determine how strongly a particle is confined at a defect, and applied to different systems. We applied the method to investigate how trapping strength depends on anchoring conditions, liquid crystal type, and cell gap.

6.2 Quantifying the Confinement Strength of Defects Trapping Particles with Weak and Strong Surface Anchoring

We observed particles with weak surface anchoring in a liquid crystal, and recorded the particles’ trajectories. We aimed to determine if using particle tracking allowed us to quantify the strength of trapping at defects in the liquid crystal. After studying particles with weak anchoring, we studied particles with strong anchoring conditions.

6.2.1 Weak Anchoring Case

6.2.1.1 Experimental Method

The microscopy setup was based on a Leica DM-IRB Inverted Microscope, as opposed to the Nikon setup described in chapter 4. The objective lens was 100 x as usual, but with a numerical aperture of 1.3. Aside from minor differences in specifications, the setup was nearly identical to the Nikon setup. The setup included an optical tweezing system. The optical tweezers were used to control the position of the particles and determine whether the particles were adhered to the glass (see section 6.2.1.2), but were never used as an active microrheology method. A schematic diagram of the Leica setup is shown in Fig. 6.1 below.

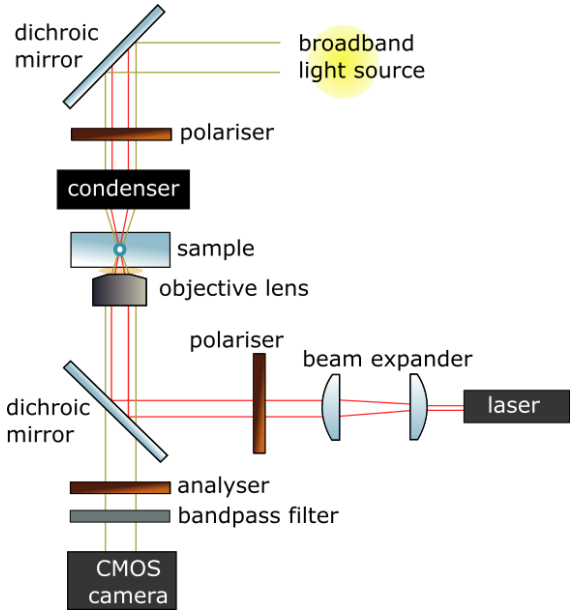

Fig. 6.1. Leica microscope laser tweezing setup. The layout is almost identical to the Nikon setup in chapter 4.

The laser was a continuous wave Laser Quantum Ventus 1064 (wavelength = 1064 nm). The laser spot was used to trap the particles optically, then position the particles relative to the defects.

In chapter 3, we gave the equation for the trapping force of a spherical dielectric particle in a laser trap [7]:

$$F_{particle} = \frac{Q_{OT} n_1 P}{c}. \qquad \text{Eqn. 6.1}$$

The Q factor, Q_{OT}, depends on the beam shape, laser spot size, and the difference between refractive index of the medium and the particle. The Q factor also varies depending on the particle position within the beam, but here we will be quoting the maximum value. While the Q factor was not measured in the experiment in this chapter, an estimate can be made based on a similar experiment in the literature, using the same equipment. In crystal chapter 7 of Sanders [1], Q_{OT} was measured for a 6μm polystyrene particle in MLC-6648, in the x-y plane. In this case, $n_2 - n_1 = 0.08$ when PS is used in Sanders' experiment, and $n_2 - n_1 = 0.17$ in the experiments in this chapter, so Q_{OT} cannot be assumed to be identical. Nevertheless, the Q factor is likely to be of the order ~0.2. Trapping a particle in MLC-6648 with $Q_{OT} = 0.2$ at a laser power of 50 mW corresponds to a trapping force of 50pN. Furthermore, taking into account the viscosity of the liquid crystals, Sanders also measured the trap stiffness of particles trapped in a 50 mW laser trap, for 2 μm particles in MLC-6648 and 6 μm particles in another liquid crystal, MLC-6609 (which has viscosity within 20% of MLC-6648). In both cases, trap stiffness was between 10-40pN/μm [1,8].

There was no acousto-optic modulator in this setup, but instead an electronically controlled xy stage was used to position the sample relative to the laser focus and camera. The camera was an Allied Vision Prosilica EC 1280 CMOS, which operated at a frame rate up to 500 fps.

We chose a combination of particles and liquid crystal that satisfied $n_{particle} > n_{medium}$ in every direction, thus allowing for 'traditional' optical tweezing. To satisfy these conditions, we selected a liquid crystal with a low refractive index, and a nematic phase at room temperature, MLC-6648 (Merck). The particles were high refractive index melamine resin spheres (melamine formaldehyde, MF) particles (Microparticles GmbH), 4 μm in

diameter. The refractive indices of the MF particles and the liquid crystal MLC-6648 are shown in Table 6.1 below.

	MF Particles	MLC-6648 [1,2]
Refractive index	1.68	n_e = 1.48, n_o = 1.55

Table 6.1. Refractive indices of melamine resin particles and MLC-6648. The particles were 4 μm in diameter.

6.2.1.2 Results

At high magnification (100 x), no evidence of satellite defects could be seen accompanying the particles in the liquid crystal. From this, it was concluded that the anchoring at the surface of the particles was weak. The trajectories were recorded for a number of particles, recorded as 'trapped' in a defect or 'not trapped'. Particles were assumed to be trapped if within approximately <1/10th the diameter of the particle from the centre of the defect. Particles were assumed not to be trapped if more than ~10 x the particle diameter away from the centre of any defect, typically 100 μm or more. The trajectory of the same particle was measured at a number of locations, at both line and point defects, such as the line defect shown in Fig. 6.2 below.

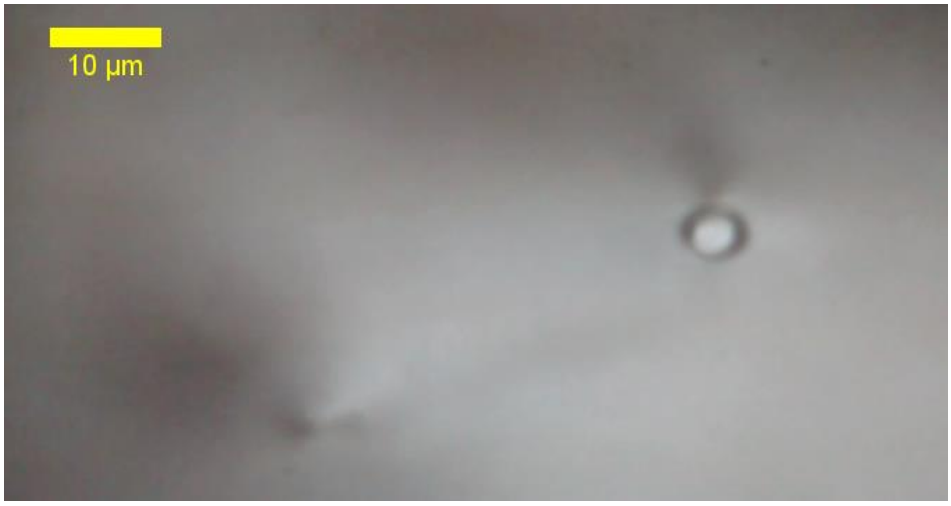

Fig. 6.2. Image of particle trapped at a line defect in MLC-6648, taken by polarising microscopy. The laser trap could be used to pull the particle off the defect if needed.

As discussed in chapter 5, the mean square displacement a particle should take the form:

$$\langle \left(R_i(t)\right)^2 \rangle = \frac{2k_B T}{\kappa_i}\left[1 - \exp\left(-\frac{\kappa_i t}{\xi_i}\right)\right]. \qquad \text{Eqn. 6.2}$$

Indeed, the above form was observed for particles confined in defects of whichever type, in other words, MSD increasing linearly at small timescales (Brownian motion) and remaining constant at longer timescales (confinement). Above 100 seconds, some features due to drift and other causes became significant, so timescales above ~100 s were not included in any linear fits. Details on the analysis of MSDs, including any data that was excluded, and how drift correction was performed, can be found in chapter 5. An example MSD is shown in Fig. 6.3 below.

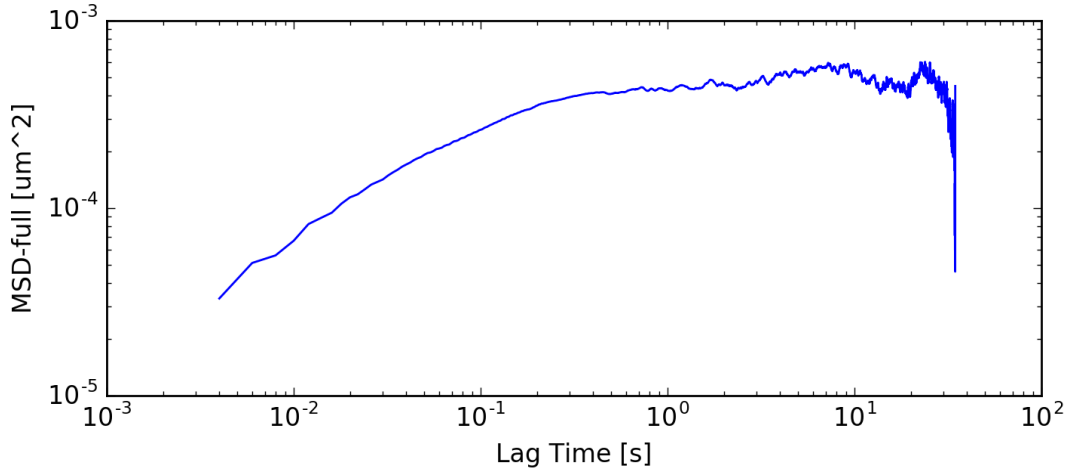

Fig. 6.3. MSD for 4 μm particle trapped in ±1 defect. The form is approximately as predicted in Eqn. 6.2.

As in chapter 5, the exponential can be fitted with an equation of the form:

$$y = A_1 \exp\left(-\frac{\mathrm{x}}{t_1}\right) + y_0 \qquad \text{Eqn. 6.3}$$

where y is the dependent variable, x is the independent variable, and the three constants A_1, t_1 and y_0 are constants, which can be shown to be equivalent to Eqn. 6.2. Fitting the equation gives us the results in Fig. 6.4 below.

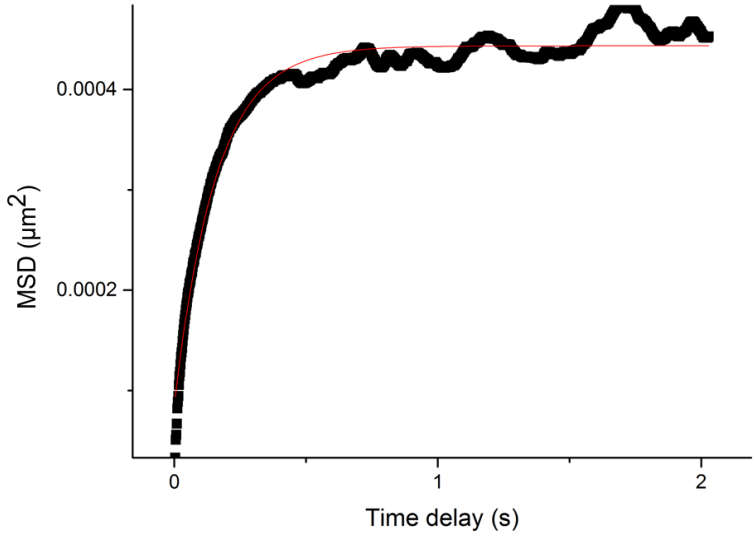

Fig. 6.4. Graph of exponential fitting of same data in Fig. 6.3 above.

The result of the fitting gives a confinement strength of κ =23 (with an error on the fit of ±0.2, similar to κ =23 given by fitting a straight line. As in chapter 5, both methods appear valid ways of fitting the data, and do suggest that the particles are behaving as the modelled behaviour, although only the straight line fitting method was used to process the majority of the data.

A histogram of particle positions reveals information about the location of the particles. The histograms of confined particles were usually approximately Gaussian (of the form $f(R_i) = Ae^{BR_i{}^2}$ where A and B are constants), with some noise, such as Fig. 6.5 below.

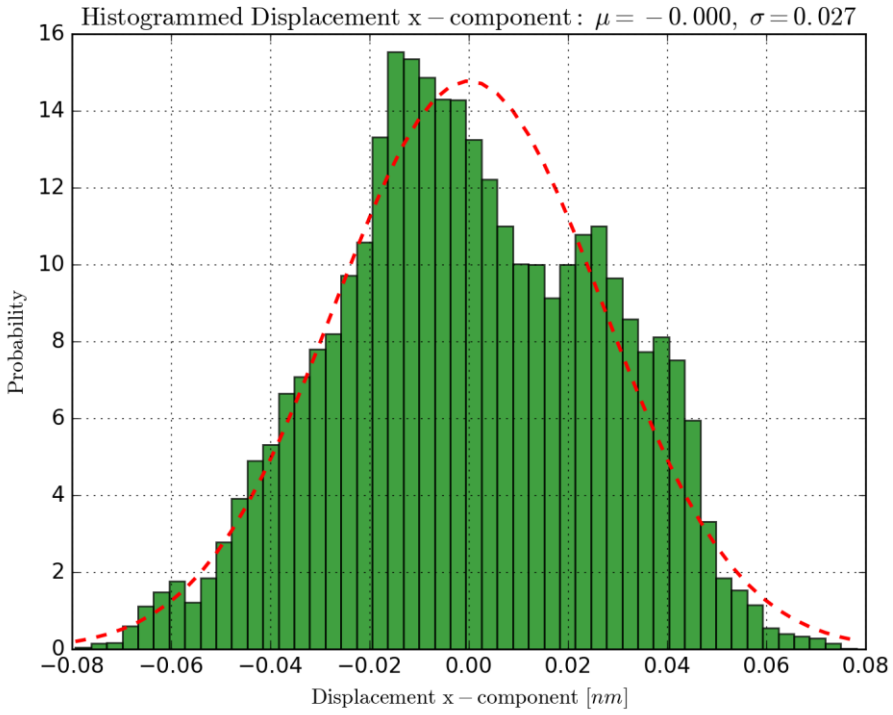

Fig. 6.5. Histogram of particle positions for particle trapped in a ±1 defect. Probability is given as a %.

The type of defect (±1 vs ±½, line vs point) did not appear to have any effect on the form of the MSD, as can be seen by comparing e.g. the MSD of a particle at a point defect (Fig. 6.3, above) and the MSD of a particle trapped at a line defect (Fig. 6.6, below).

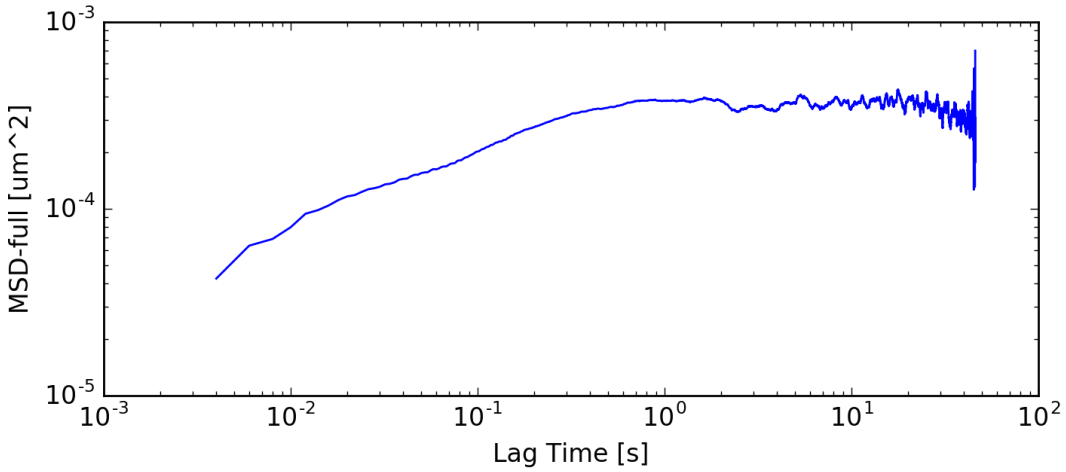

Fig. 6.6. The MSD for a particle trapped at line defect in MLC-6648 was of the same form as a particle trapped at a point defect.

We did not test a large enough number of defect types to determine if there was a statistically significant effect of defect type on defect strength, but each type studied had the same order of magnitude.

In the process of measurement, we also tracked some particles that were not close to defects. When we used the laser trap to attempt to move these particles from their original position, no movement was observed, something we will comment on further in the discussion section. We believe these particles were somehow adhered to the surface through either Van der Waals type force, or possibly elastic forces. On further observation, the 'adhered' particles were found to all lie in one of two planes (as determined by microscope focussing), further suggesting that these particles were adhered to the substrates.

We found that the MSDs of 'adhered' particles could be analysed in a similar way to MSDs of particles at defects. Due to being stuck on the surface, the effect of drift was often immediately apparent, such as in Fig. 6.7 below (before drift correction) and Fig. 6.8 below (from the same raw data, after drift correction).

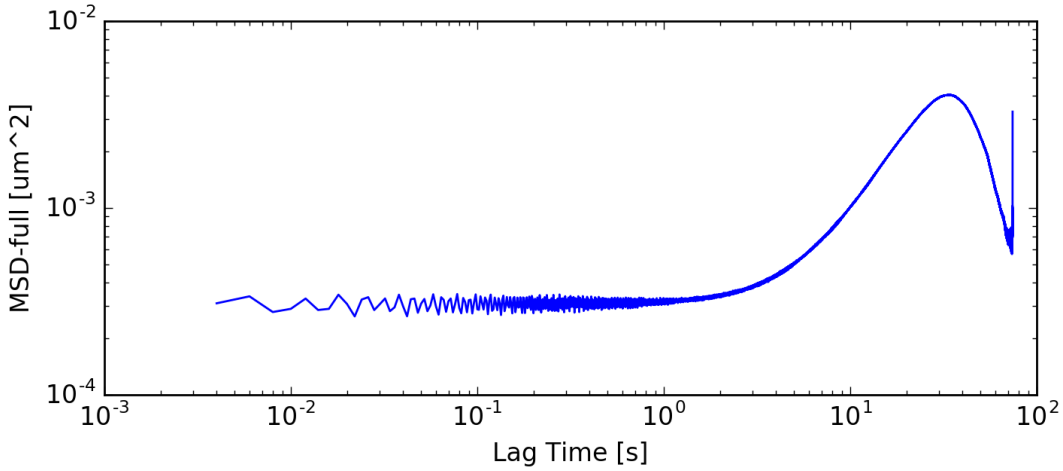

Fig. 6.7. MSD of particle adhered to substrate in MLC-6648. In timescales in the 10s of seconds, the MSD increases exponentially, as would occur if linear drift were occurring.

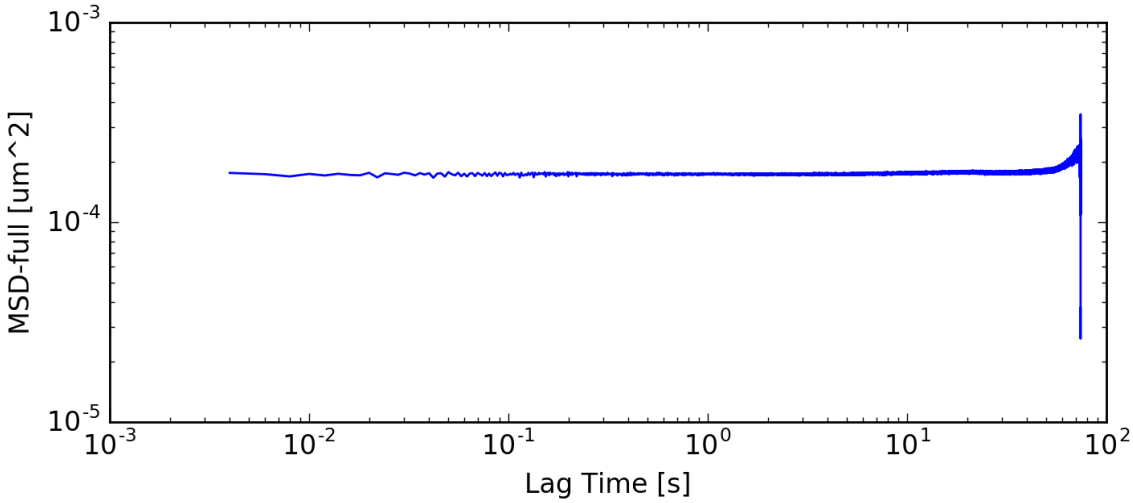

Fig. 6.8. After drift correction, the MSD is approximately constant.

The histograms of the adhered particles (e.g. Fig. 6.9 below) were approximately Gaussian in form.

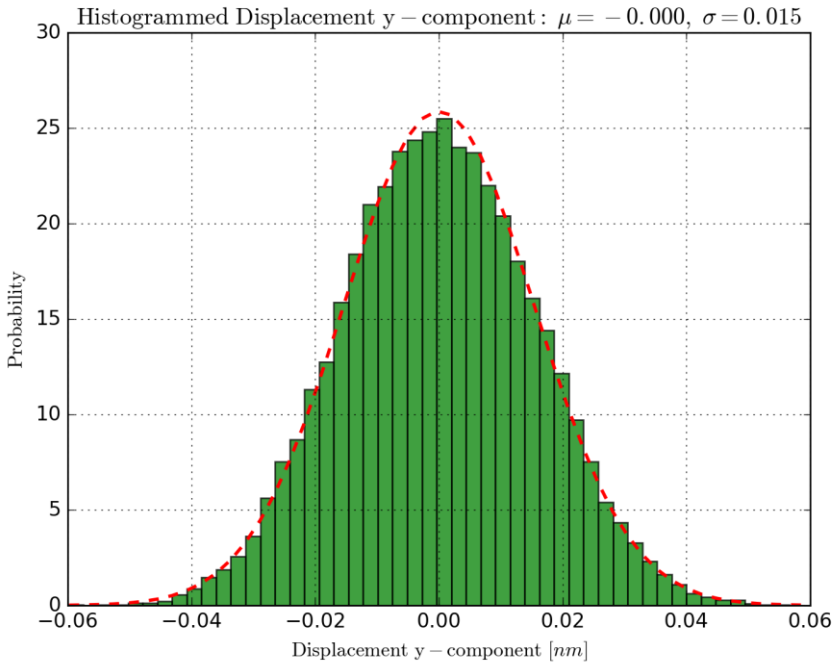

Fig. 6.9. Histogram of particle confined on surface of glass after drift correction. The histogram has a similar form to that of a particle confined at a defect. In this case, the distribution is very nearly Gaussian.

From these results, the confinement strengths (given in Table 6.2 below) were quantified.

Particle Location	Confinement strength, κ (pN/µm)
Adhered to glass	20±10
Near to defect	15±10

Table 6.2. Confinement strengths for melamine resin particle confined at defects in MLC-6648, including ±½ and ±1 defects.

Particles far from defects were also tracked. On observing a scatter plot (Fig. 6.10 below), it is clear that that the particles were not localised. The path shown in the scatter plot is typical for Brownian motion.

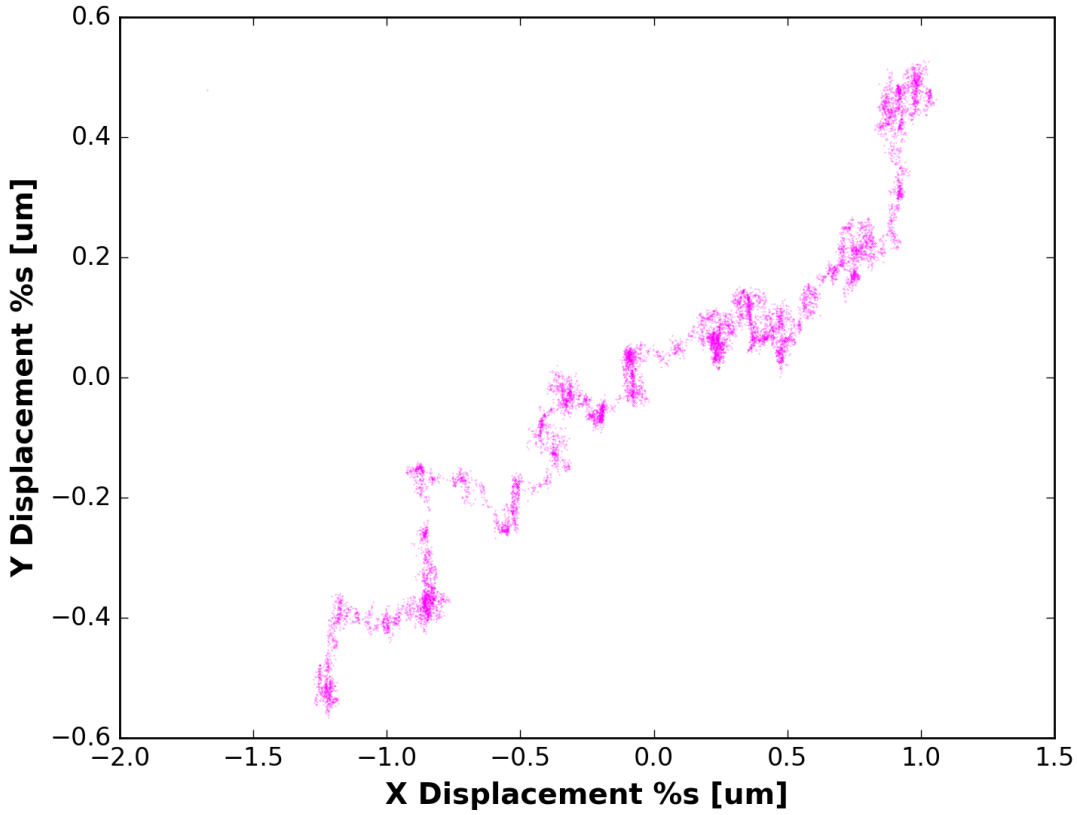

Fig. 6.10. Scatter plot of position for particle in MLC-6648, away from defects (measured over a timescale of approximately 100 s).

The MSDs of the particles away from defects (such as Fig. 6.11 below) were linear up to timescales of 100 s, as expected for a particle undergoing Brownian motion.

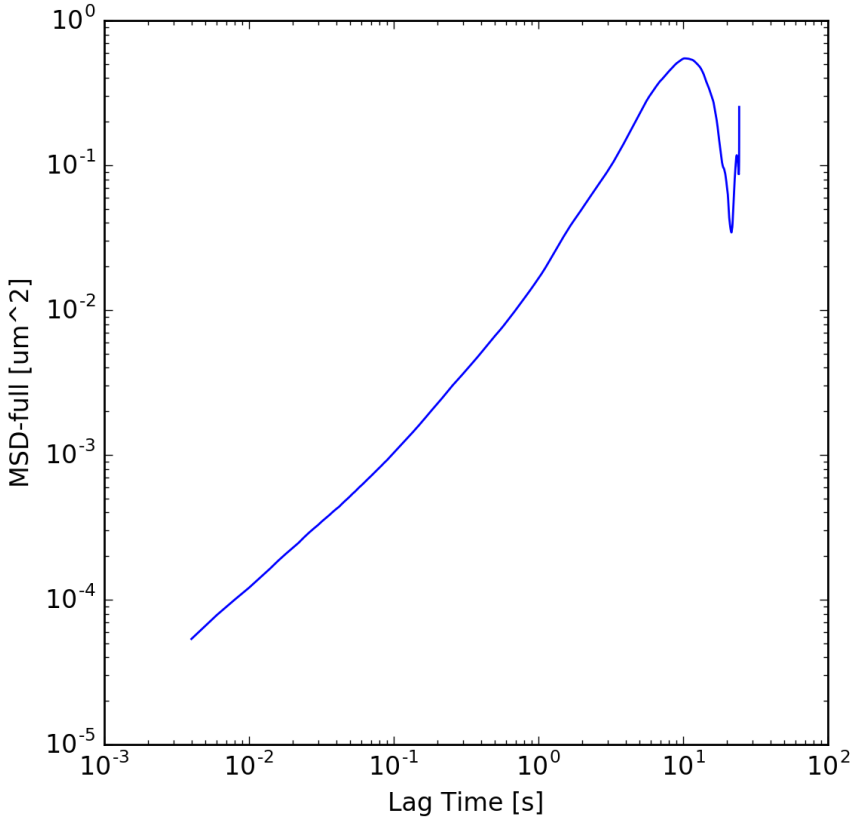

Fig. 6.11. The mean square displacement of particle dispersed in MLC-6648 away from defects was linear, except at timescales of above ~100 s. For comments on the drop at longer timescales, see chapter 5.

Like the confined regions, the mean square displacements of diffusing particles can also be fitted, this time to a straight line. We fitted to a short timescale to ensure none of the confined region was affecting the results, the fitting shown in Fig. 6.12 below. This fitting was performed in Origin with a similar least squares method to the Python fitting.

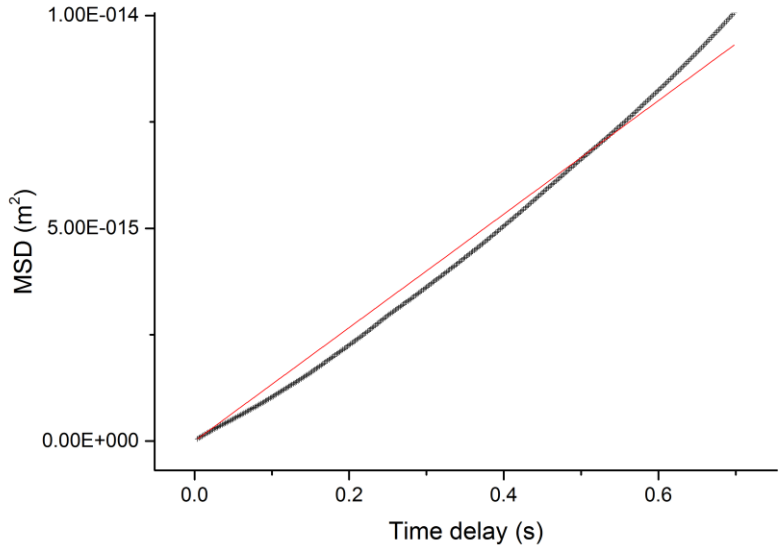

Fig. 6.12 Mean square displacement of particle in Fig. 6.11 with linear fit, at short timescales.

We also constrained the fit to intercept at (0,0), as we know that the mean displacement at zero time must also be zero. The calculated viscosities are shown in **Error! Reference source not found.** below, deduced by applying Stokes' law. The viscosities are shown below. The error on the particle size (used in Stokes' law) is assumed to be ±0.5 μm.

	1D	2D	3D
Viscosity (m Pa s)	7	15	22
Error from particle size (m Pa s)	±1	±2	±2

Table 6.3. Viscosities calculated from the fitting performed on Fig. 6.12. According to chapter 5, equations 5.4, 5.11 and 5.22 respectively for the 2D and 3D cases.

When comparing to results in the literature, both the 2D and 3D cases are within 2 standard deviations of e.g. the bulk viscosity for MLC-6648 recorded

in Table 6.9 below, and other similar results in the literature. The MSD was calculated from the average of x and y components only. However, it is possible that the particles are also diffusing in the z-direction also, something not captured by the results.

Observing a histogram (such as Fig. 6.13 below) also shows clearly that the particle is not confined to a single region of the cell.

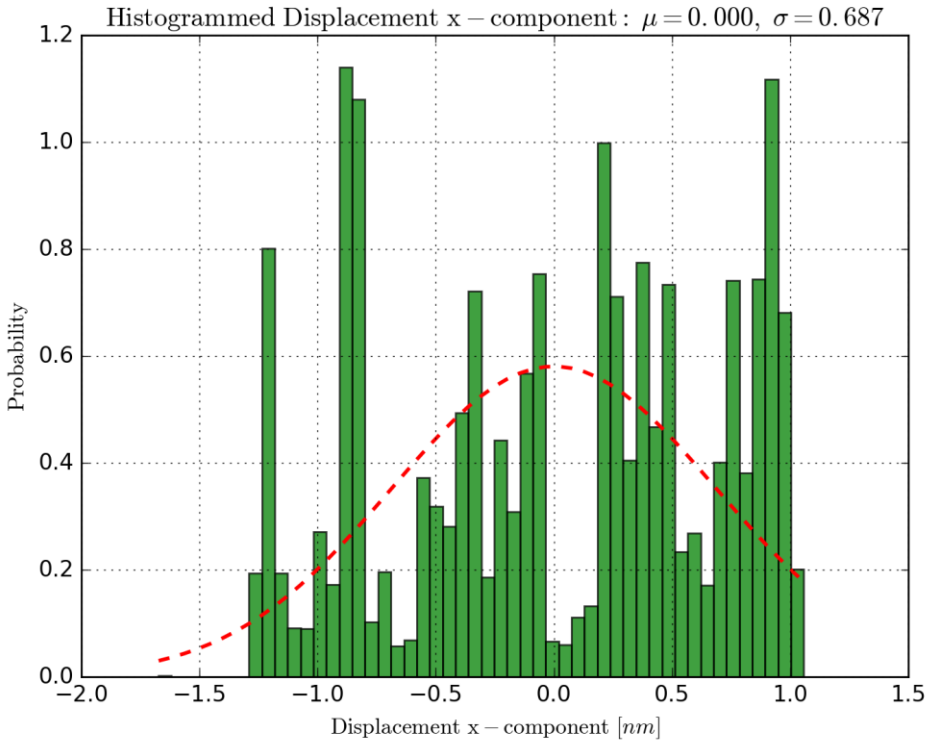

Fig. 6.13. Histogram of positions for a particle away from a defect. The distribution is definitely not Gaussian.

Considering longer timescales, we could also calculate the maximum possible value for confinement. By taking the value of MSD at the highest timescale measured, we could conclude that if there is any confinement of the particles in these regions, it must be lower than ~1 pN.

6.2.2 Strongly Anchored Particles

6.2.2.1 Experimental Method

The experimental setup was the Nikon inverted microscope and laser tweezing system described fully in chapter 4.

We did not succeed in using DMOAP (n-dimethyl-n-octadecyl-3-aminopropyltrimethoxysilychloride,) to promote homeotropic alignment on the melamine resin particles. This is possibly due to the lack of OH groups in melamine resin: when DMOAP binds to glass, it uses OH groups on the surface of the glass to bind to, by a bond shown in Fig. 6.14 below. Instead, we treated 5 µm diameter borosilicate particles.

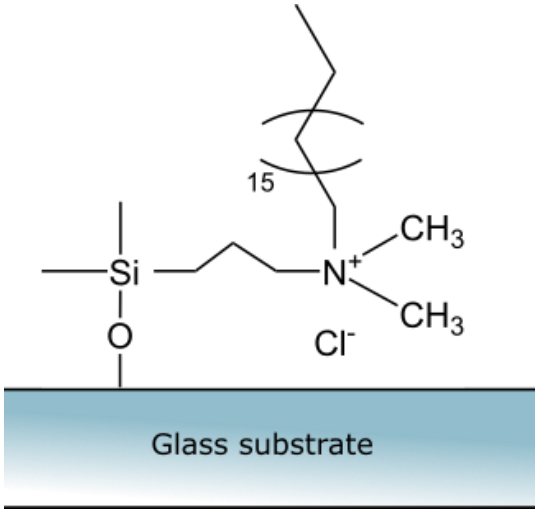

Fig. 6.14. Chemical structure of DMOAP bound to a glass surface, based on diagram from D'Elia and Barna et al [9]. Note that the first part of the alkyl chain runs parallel to the substrate, whereas the second alkyl chain is oriented perpendicular to the substrate

A small quantity of dried particles were added to a centrifuge tube, followed by 1ml of de-ionised water (measured by volume, Eppendorf Research Plus 100-1000 µl pipettor). Then a quantity of (0.2% vol/vol) of DMOAP solution (Fluorochem, 60% in Methanol) is added via an Eppendorf Research Plus 0.1-10 µl pipettor. The mixture was then vortex mixed for 1.3 krpm in a VWR Digital vortex mixer. To encourage sedimentation of the particles, the

mixture was centrifuged (Eppendorf Minispin) for 90 s at 6.5 krpm. Once the particles were no longer dispersed in the water/silane, excess water/silane solution was removed with a pipettor (Eppendorf Research Plus 10-100 µl). Another 1 ml of DI water is then added, and the particles are re-dispersed in the vortex mixer. The sedimentation and washing process was repeated a further four times for each batch of particles. Finally, the particles were dried to remove any excess water not removed by the pipettor, by placing in an oven (Cook Works toast oven KWS1009) and baking at 90°C for 30 minutes.

Application of the local melting method [10] instead of optical tweezing allows us to use $n_2<n_1$.

The trajectories were recorded for the melamine particles in MLC-6648 (in section 6.3 we studied particles in 5CB. Some results from 5CB are included in this section for illustration).

6.2.2.2 Results

Under observation, satellite defects could clearly be seen accompanying the particles, both of the Saturn ring and hyperbolic hedgehog type. The defects were visible even without polarisers due to the difference in refractive index. Satellite defects were present in both liquid crystal types, MLC-6648, and 5CB (compared in section 6.3). Both defect types are shown in Fig. 6.15 below in 5CB, and Fig. 6.16 below in MLC-6648.

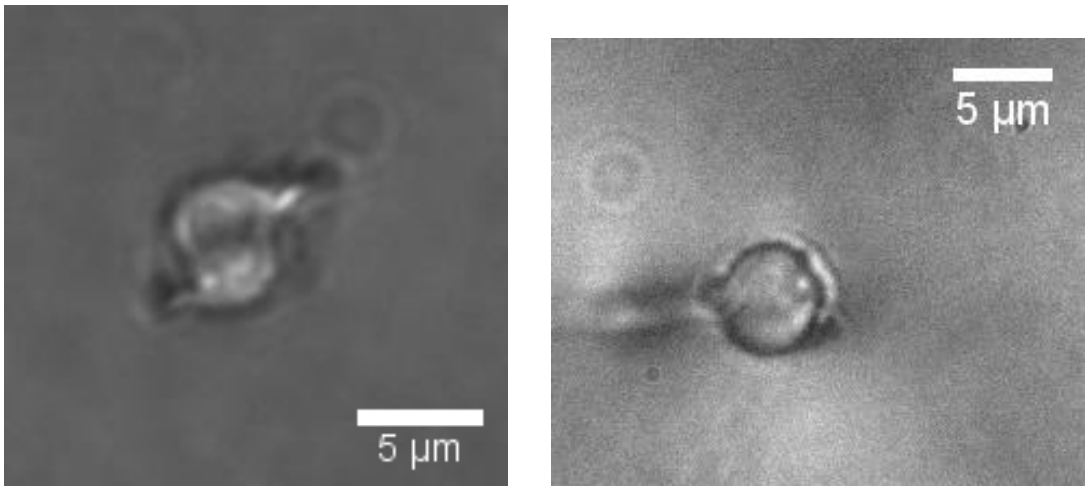

a) b)

Fig. 6.15. Images of 5 µm DMOAP-treated borosilicate particles in 5CB, with satellite defects: a) Saturn ring defect b) Hyperbolic hedgehog defect. Image b) had its contrast and brightness enhanced digitally.

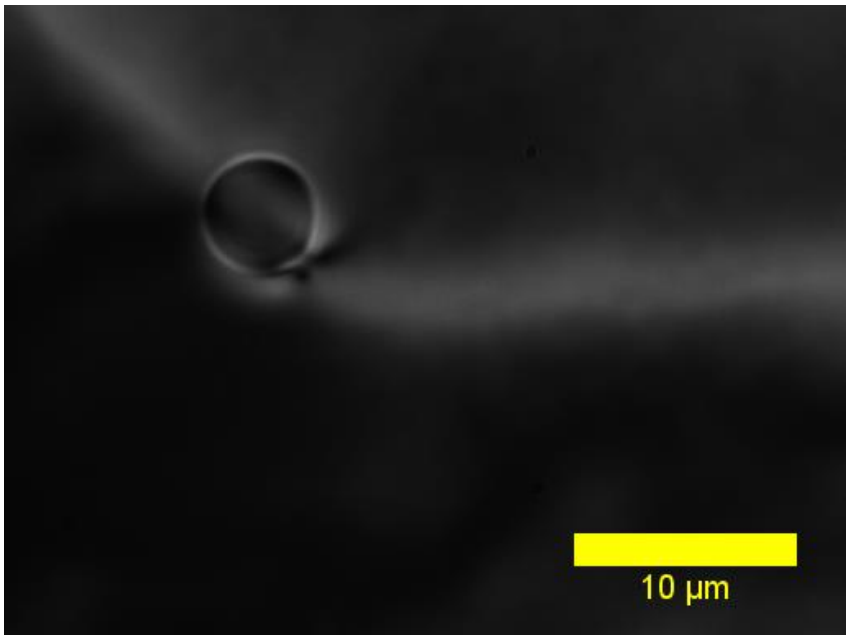

Fig. 6.16. Image of 5 µm DMOAP treated particle in MLC-6648. Note that the hyperbolic hedgehog satellite defect is attached to the line defect.

The trajectory was recorded for the particle with a hyperbolic hedgehog defect trapped at a ±1 defect, with one of the recorded MSDs of the particle's trajectory in Fig. 6.17 below.

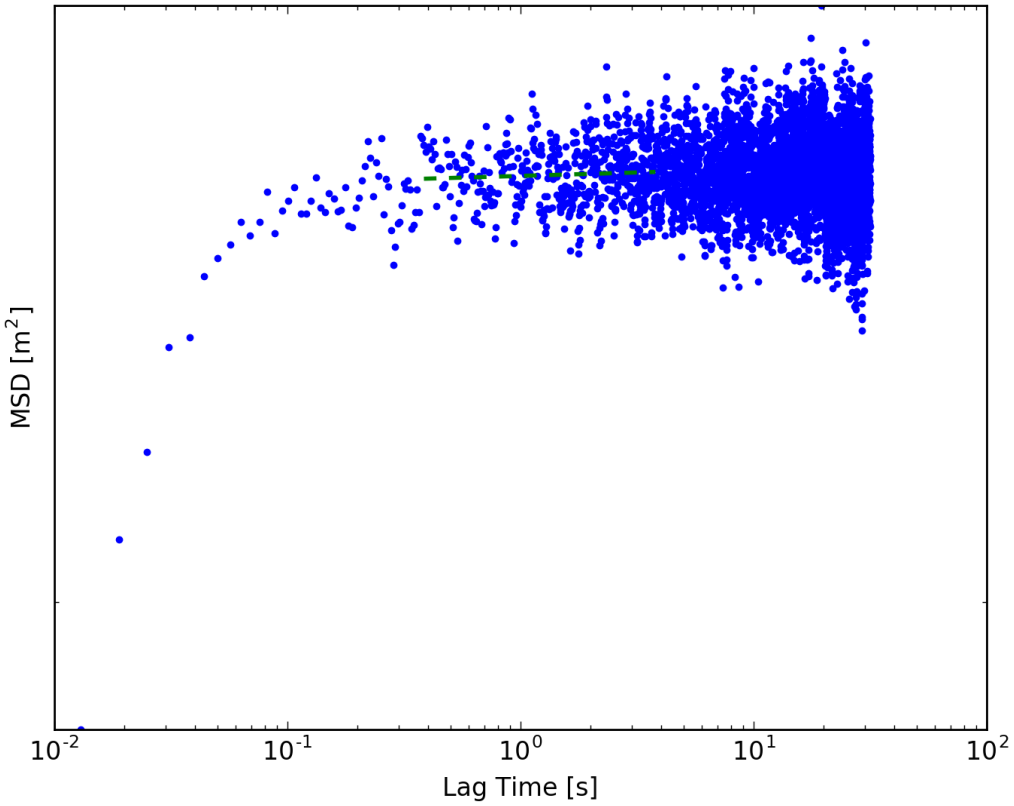

6.17. MSD for particle with HH defect at ±1 defect in MLC-6648.

The MSD takes the same form as the non-treated particles such as the MSD in Fig. 6.18 below. The histograms (e.g. Fig. 6.19 below) also show that the particles are confined to one region of the cell around the defect, which is also backed up by the scatter plots (e.g. Fig. 6.19 below. The positions shown in the scatter plot have a very different distribution to the Brownian motion in Fig. 6.10).

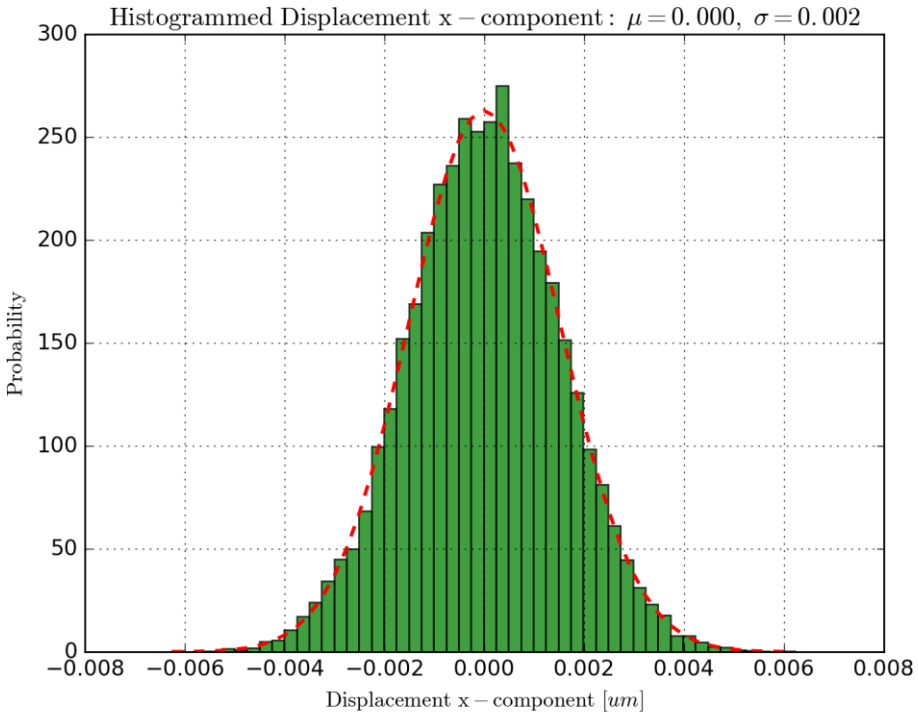

Fig. 6.18. Histogram/scatter plot for particle with HH defect at ±1 defect in MLC-6648

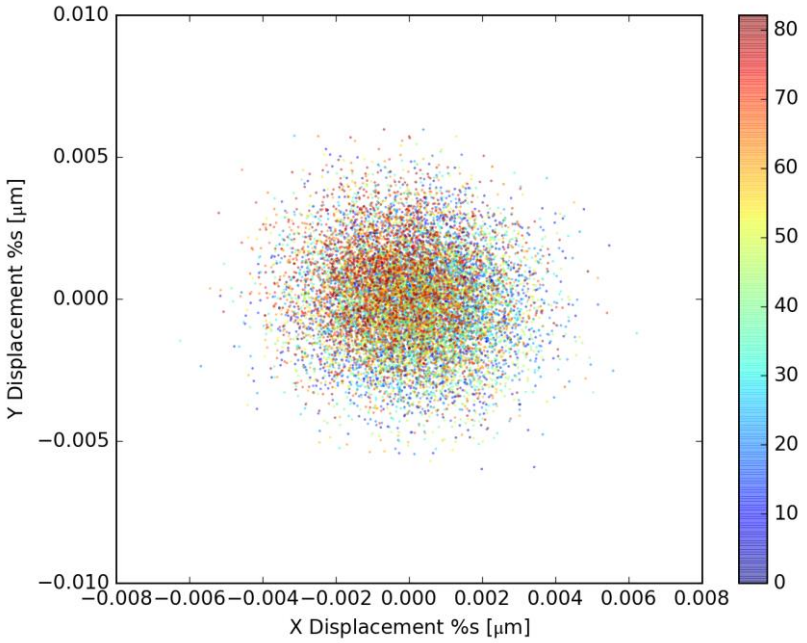

Fig. 6.19. Scatter plot showing the location of DMOAP-treated particle with HH defect at ±1 defect in MLC-6648

The results for the confinement strength of the particle with HH defect at ±1 defect in MLC-6648 are given below in Table 6.4.

Liquid Crystal	Confinement Strength (pN/μm)
MLC-6648	1500±400

Table 6.4. Confinement strength for DMOAP-treated particle with HH defect at ±1 defect in MLC-6648

6.2.3 Discussion

Comparing the two types of particle, we should bear in mind that the two types are not exactly the same. First, the diameters are not the same. In chapter 2, we saw that Stokes' law, which tells you the drag F on a particle moving in a fluid is given by:

$$F = 6\pi\eta a v. \qquad \text{Eqn. 6.4}$$

So affecting the diameter a will change the amount of drag on the particle. The density may also have an effect, as it will affect the particle's mass. Some differences in the two particles type (anchoring conditions excepted) are given below in Table 6.5.

Particle Type	Diameter	Density
Melamine resin	4 μm	1.51 g/cm^3
Borosilicate	5 μm	1.85 g/cm^3

Table 6.5. Summary of some characteristics of melamine resin and borosilicate particles that may affect their motion.

There are some differences but only approximately 20%, so any differences would not expected to be large (not growing linearly or more) either with diameter or with density.

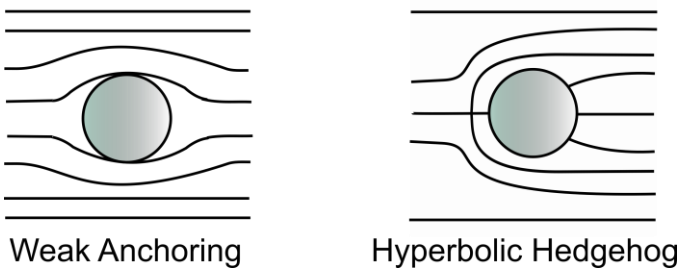

Fig. 6.20. Symmetries of director around particle with weak anchoring vs particle with hyperbolic hedgehog satellite defect.

When we compare the confinement strengths of all three scenarios (Fig. 6.21 below), there is a very large difference in confinement strength, of two orders of magnitude. It is not likely this is caused by the difference in particle material, but by some consequence of the anchoring conditions (two possible anchoring conditions around the particles shown in Fig. 6.20 above). It seems possible that the elastic forces become far more significant when anchoring conditions are strong compared to when the surface anchoring is broken.

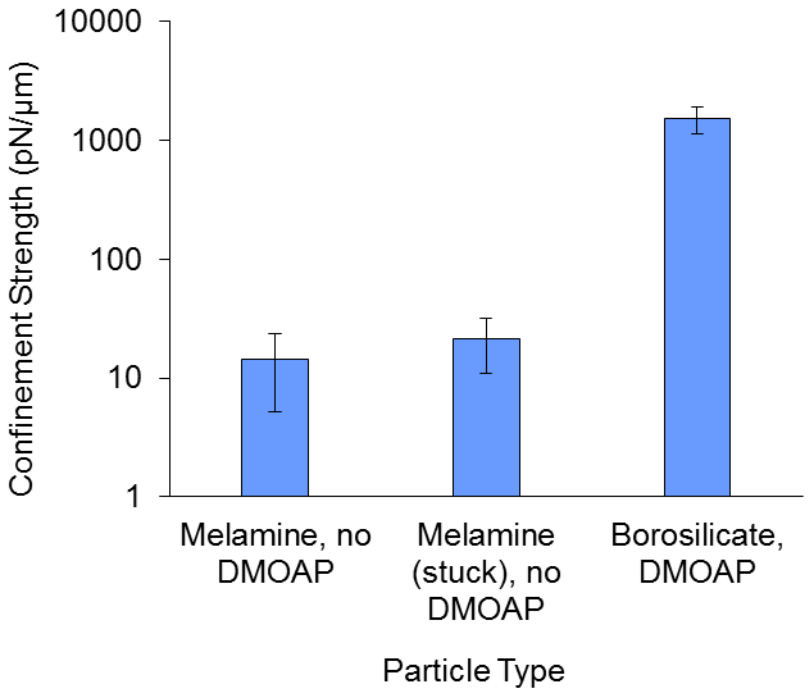

Fig. 6.21. The confinement strengths of particles confined in MLC-6648, for melamine and DMOAP-treated borosilicate particles.

There are some more things to consider that may have influenced results. The tracking software located the centre of a particle by creating a threshold above or below a certain brightness level, and taking the mean position (illustrated in Fig. 6.22 below). In the case of particles with satellite defects, the software identified the satellite defects as part of the 'edge' of the particle, thus shifting the location of the particle centre, as determined by the software (Fig. 6.23 below).

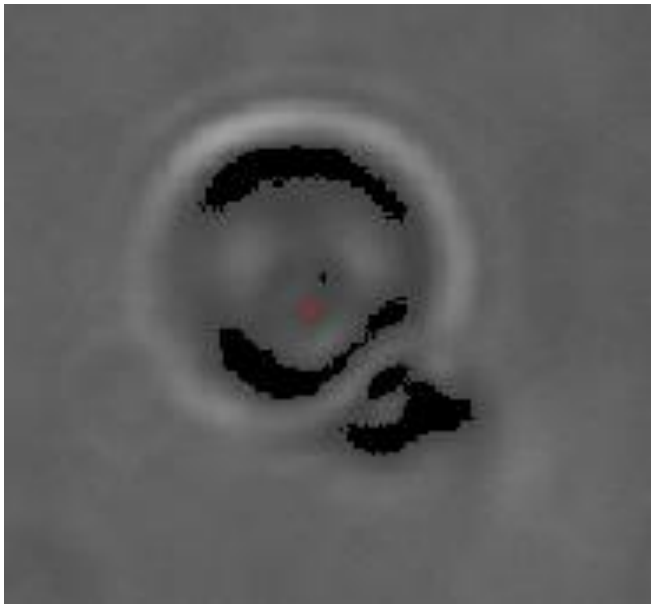

Fig. 6.22. Image of particle with hyperbolic hedgehog defect in 5CB. The edges of the particle as determined by the software are shown in black, and the centre of the particle as determined by the software is shown in red. The calculated centre of the particle has been shifted towards the hyperbolic hedgehog defect compared to the physical centre.

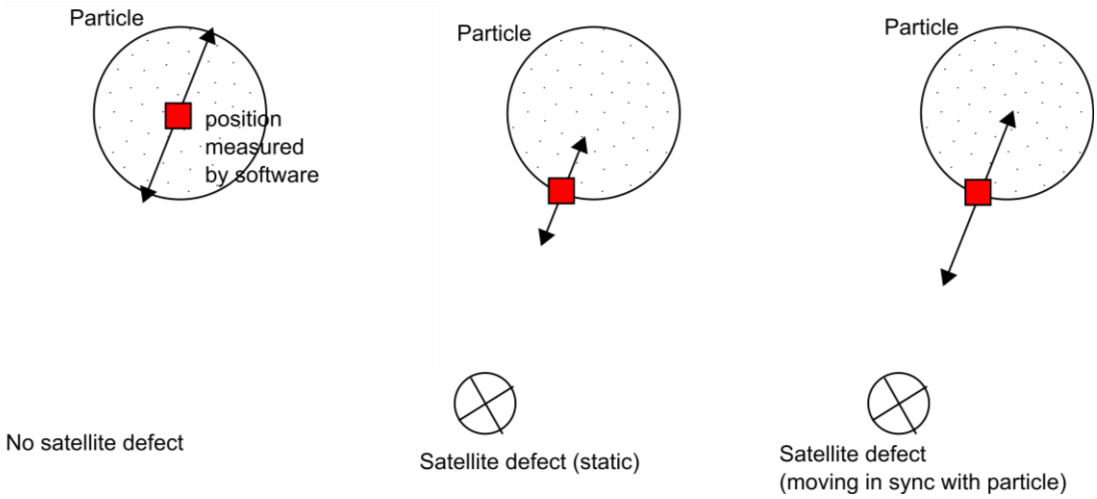

Fig. 6.23. If the particle and defect maintain the same position relative to each other, it should not affect the confinement strength, but if the defect and particle move relative to each other, it may affect results.

It may be possible to set up the experiment in such a way as to avoid this issue. Either more specialised tracking software could be used that could distinguish multiple particles, especially combined with Gaussian fitting, such as the algorithm by Rogers et al [11]. An alternative would be to use fluorescently labelled particles and a filter. However, even if the current setup cannot distinguish defects from particles, it may still be useful to compare confinement strength in different systems.

Another difference between the weakly- and strongly- anchored particles was a difference in the stability of the sample. In the samples with weakly anchored particles, most particles became attached to the upper and lower substrates within ~1 h of sample construction (within ~1 d, no freely suspended particles could be located in the samples). When particles had strong anchoring, samples contained some freely suspended particles for several weeks or more after sample construction. This must be due to the elastic repulsion forces when a particle with strong surface anchoring is in proximity of a planar-anchored substrate, described by Pishnyak et al [12].

Having found a significant difference in trapping strength between the different systems, we decided to extend the experiment to test some other variations on particles trapped in defects, and see if there were any effects on confinement strength. Only strongly anchored particles (the DMOAP-treated borosilicate particles) were used due to greater sample stability.

6.3 Confinement Strength and Liquid Crystal Type, Cell Gap and Particle Size

Since succeeding in quantifying the confinement strength of particles confined in a defect, we decided to investigate other factors that might affect confinement strength. We chose to look at the type of liquid crystal, cell gap, and particle size. In all the following experiments, the 5 μm borosilicate particles with DMOAP-treatment were used.

6.3.1 Experimental Methods

The microscope and tweezing setup was the same Nikon microscope described in chapter 4. Schlieren cells were constructed and filled by the same procedure described in chapter 4, section 4.2.

6.3.2 Effect of Liquid Crystal on Confinement Strength

We chose to compare the effect of liquid crystal on confinement strength. The two liquid crystals were 5CB and MLC-6648.

Samples had 50 µm cell gaps, and were made with 5 µm borosilicate spheres treated with DMOAP according to the same method as 6.2.3 Comparisons were made for ±1 strength point defects in the bulk, with hyperbolic hedgehog defects.

The MSDs had the same form for the two liquid crystals, but different average confinement strengths (Fig. 6.24 and Fig. 6.25 below).

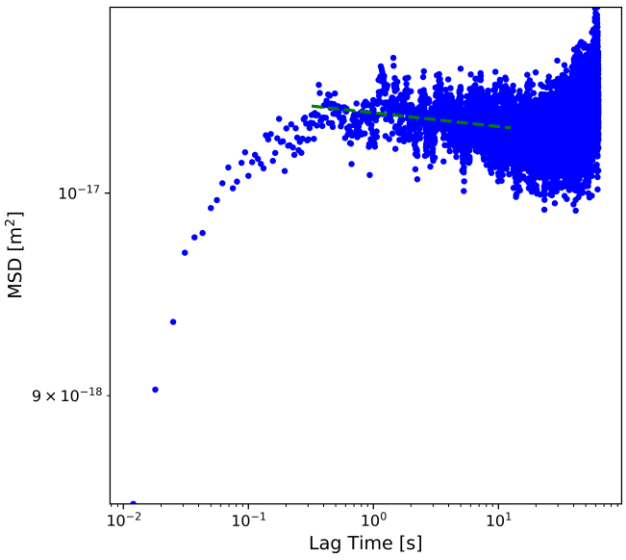

Fig. 6.24. MSD for 5 µm borosilicate particle with HH defect at ±1 defect in 5CB.

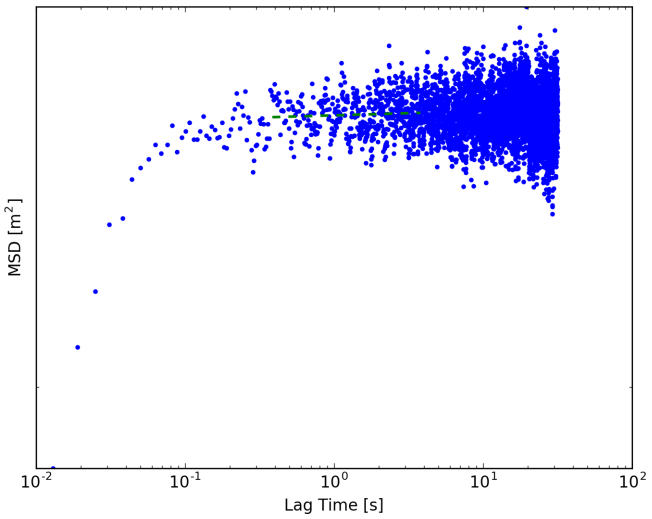

Fig. 6.25. MSD for particle with HH defect at ±1 defect in MLC-6648.

Average confinement strengths are given below in Table 6.6.

Liquid Crystal	Confinement Strength (pN/μm)
5CB	300±150
MLC-6648	1500±400

Table 6.6. Trap stiffness in two different liquid crystals, 5CB and MLC-6648 (5μm particles with homeotropic surface anchoring)

6.3.3 Effect of Cell Gap on Confinement Strength

So far, we have neglected any effect of the z – direction. Even in a simpler fluid system, the proximity of a boundary can have an effect on the motion of a particle suspended in a fluid [13,14]. In addition to this, the director field in the liquid crystal can vary in the z-direction.

Certainly, many experiments on particle tracking in the literature are conducted in cell gaps relatively small compared to the diameter of the particles. We investigated cell gap as one way to determine whether the proximity to the substrates have any effect on the behaviour of particles, and if so, whether there is a certain distance at which the effect becomes significant.

We used Schlieren cells with 50 μm, 19 μm and 10 μm gaps, with 19 μm particles with strong surface anchoring. The liquid crystal was 5CB. Comparisons were made for particles with hyperbolic hedgehog defects at ±1 defects.

The cell expected to have the most difference was the 10 μm cell, having twice the diameter of the particle. Scatter plots show the location is very small. The scatter plots also illustrate the application of drift correction as in chapter 5 section 5.6.

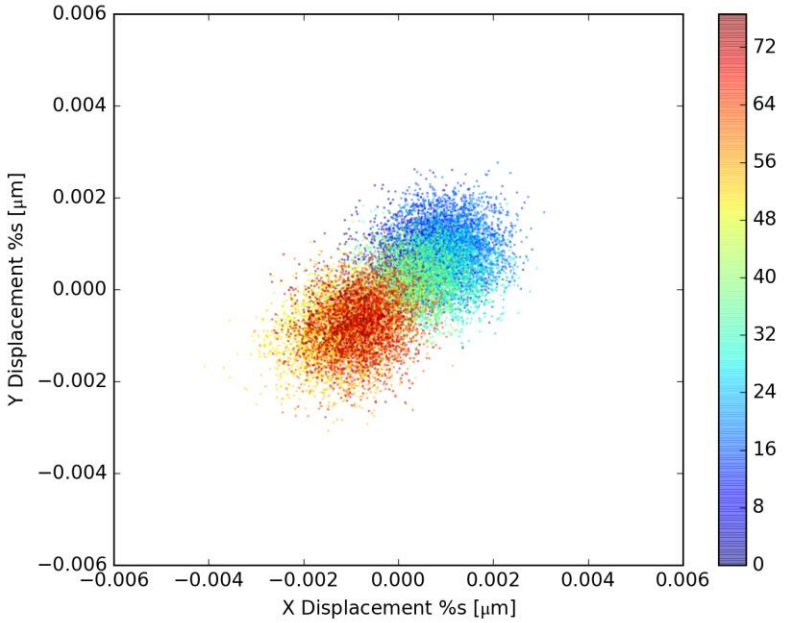

Fig. 6.26 Scatter plot of location of 5 μm particle in 10 μm cell, before drift correction.

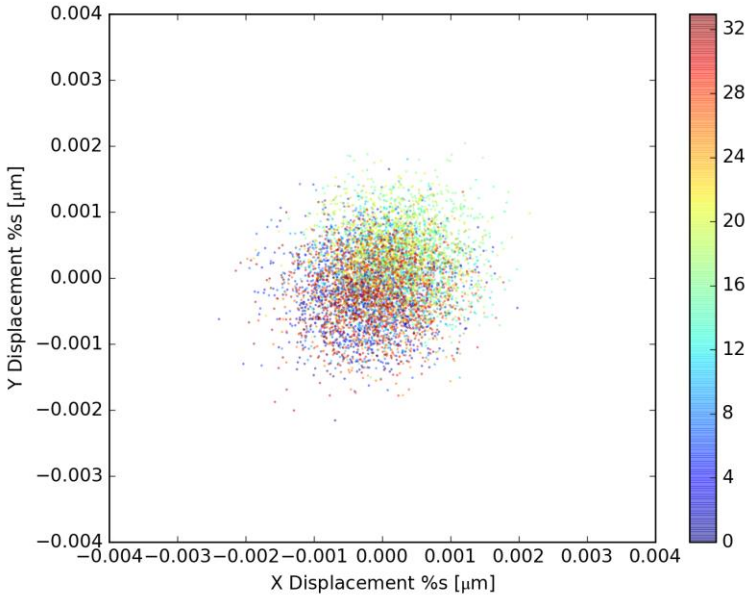

Fig. 6.27. Scatter plot of location of 5 μm particle in 10 μm cell, at ±1 defect, after drift correction.

The corresponding mean square displacements are shown in Fig. 6.28 and Fig. 6.29 below.

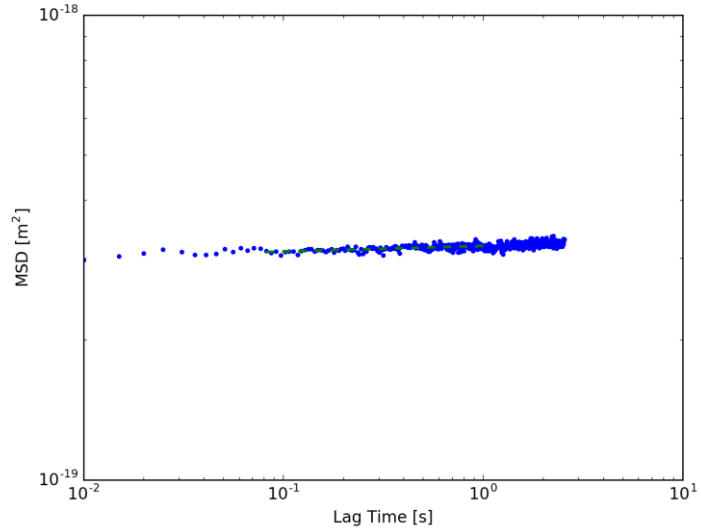

Fig. 6.28. MSD for particle in 10 μm cell, before drift correction.

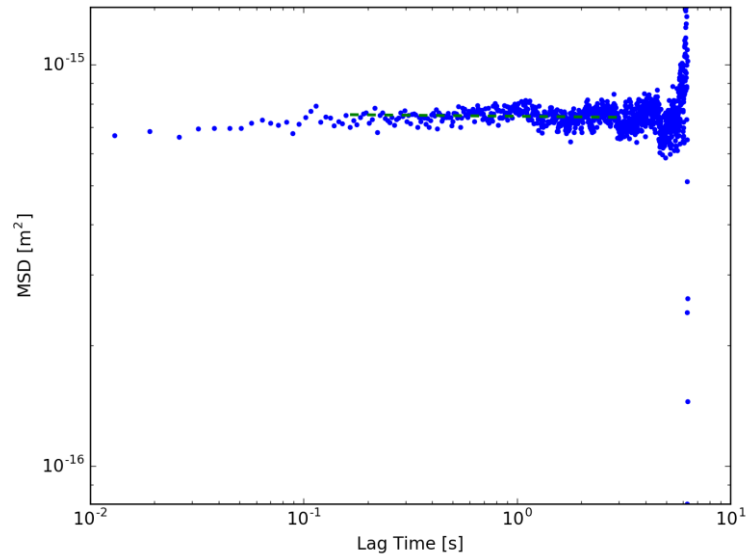

Fig. 6.29. MSD for particle 5 μm particle in 10 μm cell, at ±1 defect after drift correction.

The average confinement strengths are shown in Table 6.7 below.

Cell Gap (μm)	Confinement Strength (pN/μm)
10	10,000±5,000
19	5±2
50	300±100

Table 6.7. Confinment strength as a function of cell gap. Particles are 5 μm in diameter with homeotropic surface anchoring.

6.3.4 Effect of Particle Diameter

We investigated if particle size has an effect on confinement strength. Two particle sizes, 2 μm diameter and 5 μm diameter borosilicate particles were compared at ±1 defects in 5CB, examples in Fig. 6.30 and Fig. 6.31 respectively, both below.

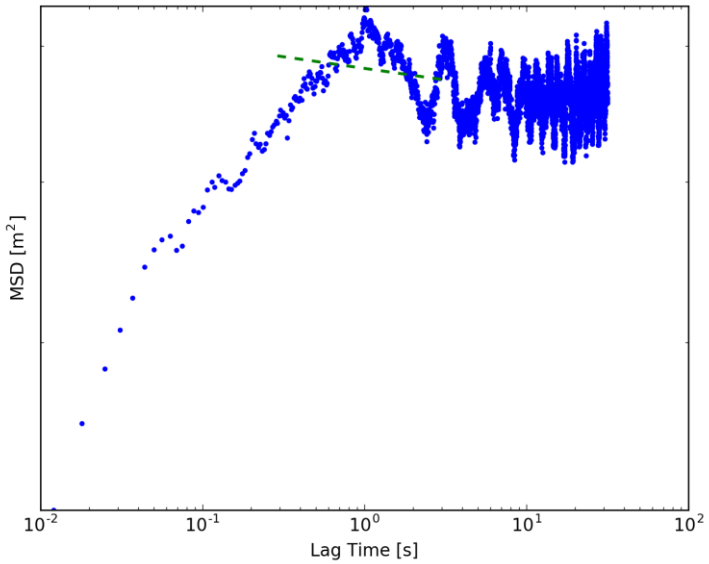

Fig. 6.30. MSD for 2 μm particle confined at ±1 defect in 5CB.

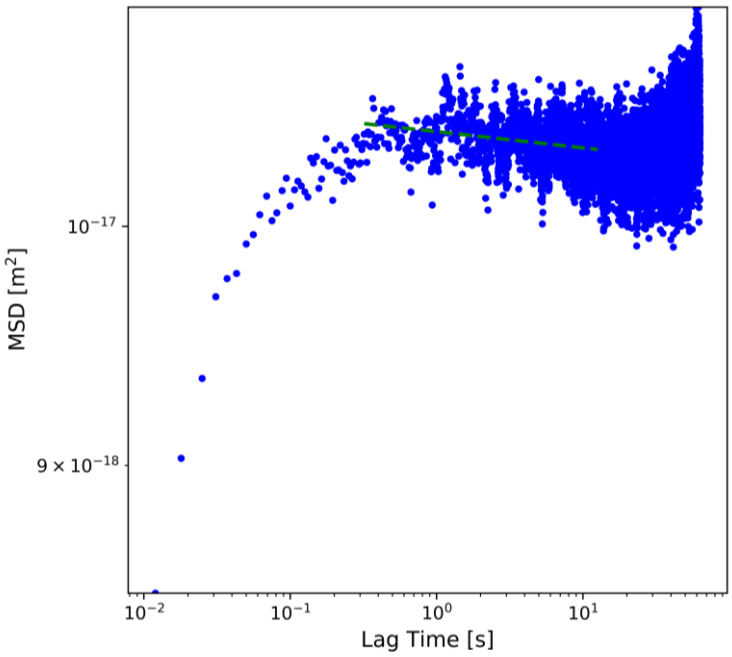

Fig. 6.31. MSD for 2 μm particle confined at ±1 defect in 5CB.

The average calculated confinement strengths are reported below in Table 6.8.

Particle Size (μm)	Confinement Strength (pN/μm)
2	180±10
5	300±100

Table 6.8. There are some suggestions of trap stiffness lowering with smaller particle size.

6.3.5 Discussion

6.3.5.1 Liquid Crystal Type

There does appear to be a significant effect of the liquid crystal choice on the confinement strength, as can be seen in the graph below (Fig. 6.32).

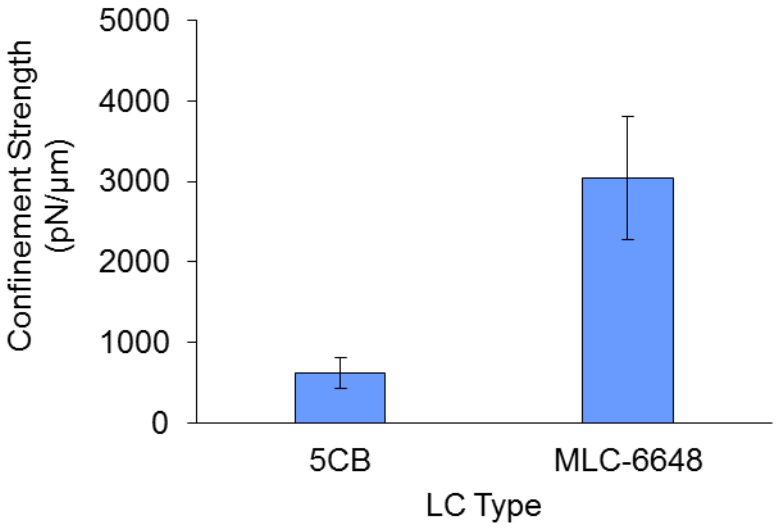

Fig. 6.32. Confinement strength for 5 μm borosilicate particles with DMOAP, in ±1 defects in 5CB vs. MLC-6648.

We measured a factor 5 increase in confinement strength for MLC-6648 compared to 5CB. To understand this we can consider some differences in the physical properties of the two liquid crystals.

One characteristic of the liquid crystals that are likely to be highly important to the interaction between particle and defect are the elastic constants,

including both splay and bend. In Fig. 6.20, we can see that hyperbolic hedgehog defects contain both splay and bend deformations. A point defect will also contain splay deformation.

Liquid Crystal	Splay elastic constant (pN)	Bend elastic constant (pN)
5CB [15]	~7	~10
MLC-6648 [16]	11.0±1.0	-

Fig. 6.33 . Splay and bend elastic constants of 5CB and MLC-6648. The elastic constant for MLC-6648 was recorded at 'room temperature', assumed to be ~20°C, and the values for 5CB are given at 20°C.

From the literature, MLC-6648 has a significantly higher splay elastic constant than 5CB, a difference of more than 30% (Fig. 6.33 above).

Viscosity may also contribute to the recorded 'trap stiffness' due to Stokes' law, although in this case the viscosities, or at least bulk viscosities, are similar for both liquid crystals (within 5%, Table 6.9 below).

Liquid Crystal	Flow Viscosity (m Pa s^{-1})
5CB	20 [17]
MLC-6648	19 [18]

Table 6.9. Average viscosity of 5CB and MLC-6648 at 20°C.

If the elastic constants are the only contribution, then the effect must be more than linear with elastic constants (approximately quadratic).

6.3.5.2 Cell Gap

We found that the confinement strength when the cell gap was similar to the particle diameter was very much larger (at least one order of magnitude)

than when the cell gap was much larger than the particle diameter. A comparison of confinement strengths for different cell gaps is shown in Fig. 6.34 below.

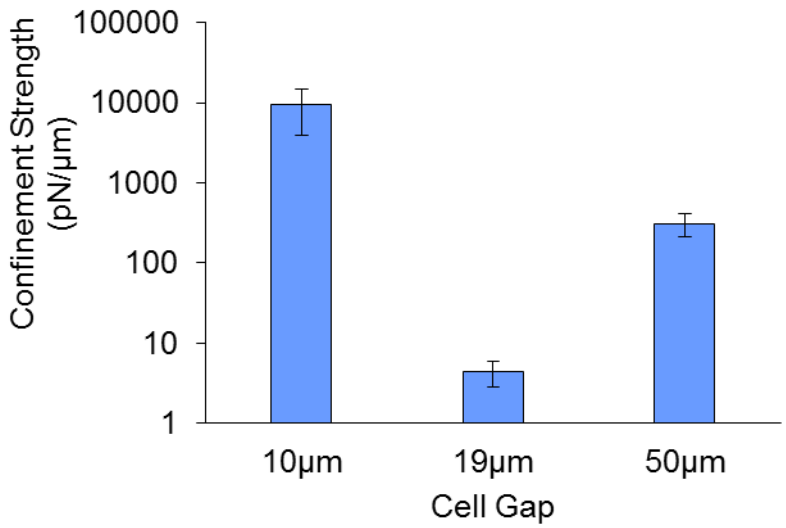

Fig. 6.34. Confinement strength as a function of cell gap for 5 μm particles confined in ±1 defects in 5CB.

The 19 μm cell appears to have a lower confinement strength than the others. This is unexpected, as it does not follow the trend of the other two measurements.

When returning to the dataset for the 19 μm cell, it is clear that there are some features of drift in the raw data. This was the one case where the Savitsky-Golay filter was used in processing the results. It is possible that this fitting is the cause of the unusual result.

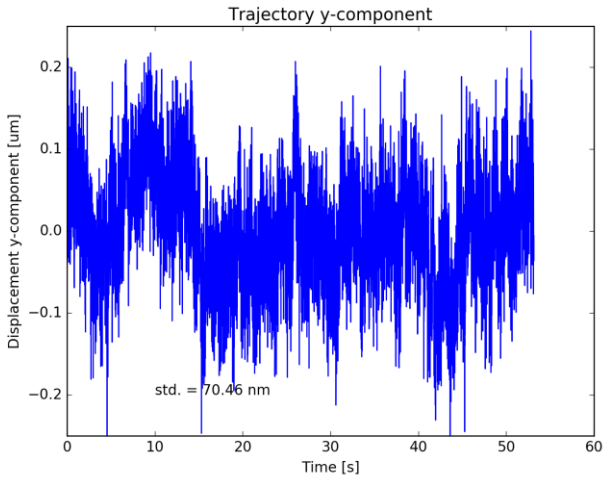

Fig. 6.35. Trajectory of y-component of particle in 19 μm cell. There is an appearance of drift that is not linear.

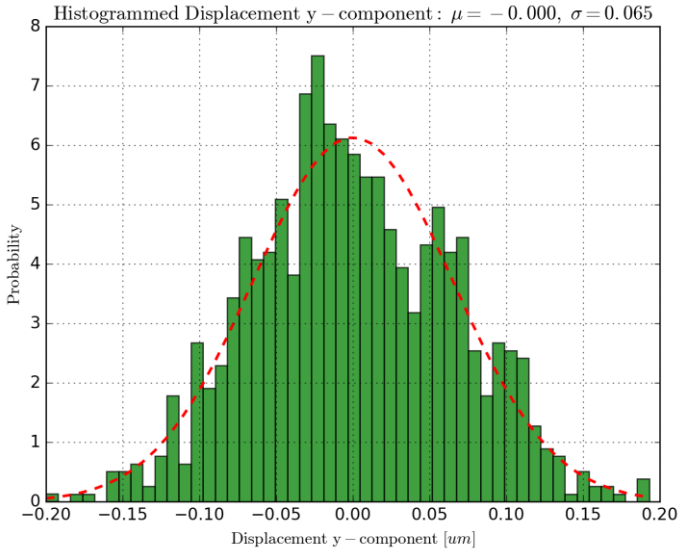

Fig. 6.36. Histogram of particle position in 19 μm cell. While the profile appears almost Gaussian, there is a large amount of noise.

This does raise some potential problems with drift corrections, especially using the Savitsky-Golay filter. Although this approach has been used by several authors to smooth data, it is appropriate to ask whether it is always a valid method to apply drift correction to results? In this case, it seems the smoothing carried out on data with drift has given an erroneous result. In the

case of this experiment, I would recommend repeating the results for the 19 µm cell with a new sample.

Considering this situation does reveal a potential difficulty with the passive method of particle tracking. This could be improved if there was a way to better account for drift. If the inside of the cell substrate was etched with a pattern on the same scale as the particle, the ‘background’ could also be tracked by the particle tracking system and used as a reference point. This would be an objective way of distinguishing movement of the sample from movement of the particle within the sample.

If the 19 µm measurement is assumed to be erroneous, the results do suggest that the confinement strength becomes very high at smaller cell gaps.

6.3.5.3 Particle Size

From the two particle sizes investigated, we found that particle size had a small or insignificant effect on confinement strength. From a graph ofthe results in Fig. 6.37 including standard deviations, it can be seen that the 2 µm particle lies between 1 and 2 standard deviations of the 5 µm result, giving a probability between 68% and 95% of being statistically significant.

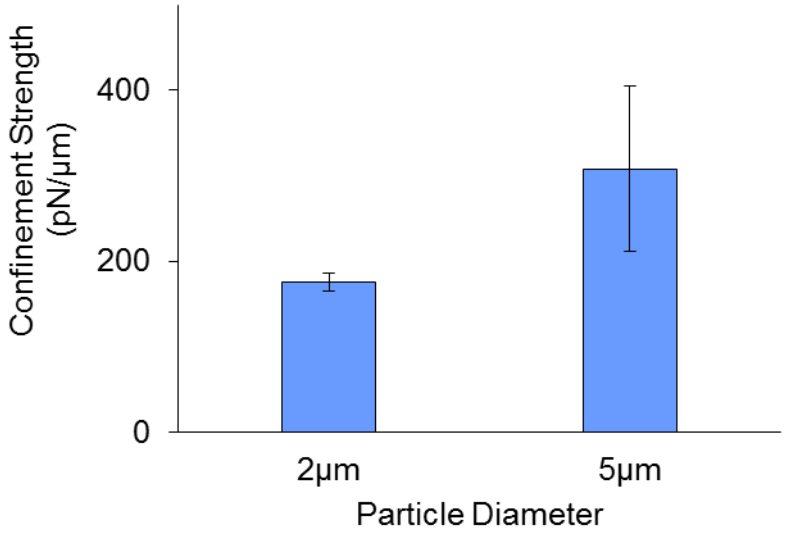

Fig. 6.37. Strength of confinement for 2 μm particles and 5 μm particles, measured at ±1 defects in 5CB. If there is an effect on confinement strength due to particle size, it is not large in the case of these two particles.

Given that result, it is unlikely that particle size (within the range studied) has any large effect on the confinement strength of a particle at a defect.

6.3.6 Conclusion

We used a technique in passive micro-viscometry to quantify the strengths of particles trapped at defects in liquid crystals.

Particles confined in defects had MSDs with a form that increased linearly at short timescales with Brownian motion, and remained constant at longer timescales. Particles with ‘strong’ anchoring and satellite defects were more strongly confined than particles with weak surface anchoring.

Liquid crystal type had a significant effect on confinement strength, the LC with larger splay and bend elastic constants resulting in greater confinement strength. Smaller cell gap showed higher confinement strength than larger cell gap. Particle size did not have a large effect on confinement strength in the size range studied (2 μm-5 μm diameter).

In our next chapter, we will continue the work on micron-sized particles in liquid crystals, but with a different particle geometry, investigating the director structure around polymeric Janus particles in a liquid crystal.

References

1. J. L. Sanders, A Study of Microviscosity in Liquid Crystals Using Laser Tweezers, University of Manchester, 2012.

2. H. F. Gleeson, T. A. Wood, and M. R. Dickinson, Philosophical Transactions. Series A, Mathematical, Physical, and Engineering Sciences **364**, 2789 (2006).

3. R. P. Trivedi, D. Engström, and I. I. Smalyukh, Journal of Optics **13**, 044001 (2011).

4. H. F. Gleeson, S. Kaur, V. Görtz, A. Belaissaoui, S. Cowling, and J. W. Goodby, ChemPhysChem **15**, 1251 (2014).

5. D. Pires, J. B. Fleury, and Y. Galerne, Physical Review Letters **98**, 247801 (2007).

6. A. V. Ryzhkova and I. Muševič, Physical Review E **87**, 032501 (2013).

7. A. Ashkin, Biophysical Journal **61**, 569 (1992).

8. J. L. Sanders, Y. Yang, M. R. Dickinson, and H. F. Gleeson, Philosophical Transactions of the Royal Society A **371**, 20120265 (2013).

9. S. D'Elia, V. Barna, N. Scaramuzza, G. Strangi, and R. Bartolino, Journal of Materials Research **24**, 2784 (2009).

10. M. Škarabot, Ž. Lokar, and I. Muševič, Physical Review E **87**, 1 (2013).

11. S. S. Rogers, T. A. Waigh, X. Zhao, and J. R. Lu, Physical Biology **4**, 220 (2007).

12. O. P. Pishnyak, S. Tang, J. R. Kelly, S. V. Shiyanovskii, and O. D. Lavrentovich, Physical Review Letters **99**, 1 (2007).

13. F. Hilding, Annalen Der Physik **373**, 89 (n.d.).

14. J. Leach, H. Mushfique, S. Keen, R. Di Leonardo, G. Ruocco, J. M. Cooper, and M. J. Padgett, Phys. Rev. E **79**, 26301 (2009).

15. A. Bogi and S. Faetti, Liquid Crystals **28**, 729 (2001).

16. S. Kaur, Y. Kim, H. Milton, D. Mistry, I. M. Syed, J. Bailey, J. C. Jones, P. B. Morgan, J. Clamp, and H. F. Gleeson, Optics Express **24**, 8782 (2016).

17. *Merck Datasheet, K Series* (Merck KGaA, 1987).

18. *Merck Datasheet, Licrystal Liquid Crystal Mixtures for Electro-Optic Displays* (Merck KGaA, 1997).

Chapter 7 Surface Alignment around Janus Particles in Nematic Liquid Crystals

7.1 Introduction

We have been investigating the topic of how micron-sized particles interact with a liquid crystalline medium. We saw how, as in the literature, adjusting the anchoring conditions at the surface of a particle affects the presence or absence of ‘satellite defects’. The presence or absence of satellite defects in turn affects how the particles move within the liquid crystal, and as we saw in chapter 6 influences how the particles interact with defects in the bulk of the liquid crystal.

In this chapter, we will begin to expand our work to look at a new particle geometry: the Janus particle. The ‘Janus particle’ was first given its name by PG De Gennes [1], in reference to Janus, the ancient Roman god of thresholds, who was known for having two faces. A Janus particle is any particle that consists of two halves, each of which has different physical properties. Through choice of materials, this could be any property such as colour or electric charge. Janus particles are of interest in many areas, such as drug delivery [2–4] and self-assembly [5–7].

Janus particles are not trivial to manufacture. The first Janus particles were manufactured in 1988 by Casagrande et al [8,9]. While the details of manufacturing Janus particles are highly varied [10–15], there are two main approaches to Janus particle manufacture, ‘top-down’ and ‘bottom-up’. Top-down approaches are usually most suitable for producing particles of several ~ μm and larger (although patchy particles of ~270 nm diameter [16] have been produced by a top-down method). Top-down approaches are often based on a ‘masking’ approach, where one half of the particle is protected by a layer of e.g. polymer, while a layer of some other material is deposited

on the second half (this was the approach used in the first Janus particles [8,9], which were 50 µm - 90 µm in diameter). Bottom-up approaches are based on growing particles in solution, for instance, using seeding and phase-separation methods [17–22].

In the case of liquid crystals, of particular interest is what would happen with a particle that has hybrid surface anchoring, where one half of the particle has homeotropic anchoring, and the other half has homogeneous anchoring. In liquid crystal research, there has been success in creating hybrid anchoring, with different approaches. First, Conradi, Ravnik and Bele [23,24] used gold sputtering to coat borosilicate spheres, to create hybrid anchoring in a nematic liquid crystal. Another group looked at ring-shaped polymeric particles which were treated later with DMOAP [25].

We were offered the opportunity to study three different varieties of Janus particle. One type was produced by the bottom-up method, the ~50 µm diameter particles. The other two types were polymeric, synthesised by the bottom-up method, and were of sizes ~500 nm and ~5 µm in diameter. The most important thing to determine was the surface alignment of the liquid crystal at the surface of the particles, hence polarising microscopy was used to observe individual particle and determine surface alignment.

7.2 ~500 nm Janus Particles

In chapter 4, we dispersed some submicron particles in a nematic liquid crystal. The majority of results are in chapter 4, but findings on alignment are summarised here for comparison with the results on the Janus system.

The Janus particles were composed of two polymers (shown in Fig. 7.1), GDMA and HEAm, synthesised[4] by the dynamic swelling method [26], a method first developed by Okubo et al [19]. The particles were doublet- and triplet-shaped in nature (a larger sphere of HEAm, with smaller GDMA spheres, shown in Fig. 7.2 below).

[4] Synthesised by S. Butterworth et al, School of Chemistry, University of Manchester

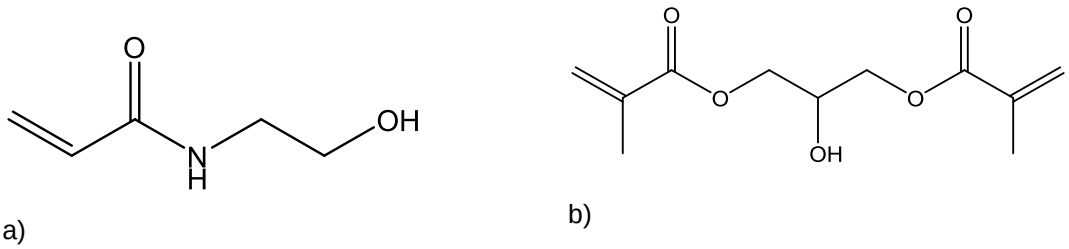

Fig. 7.1. Chemical structures of a) glycerol dimethacrylate (GDMA) and b) *N*-hydroxyethyl acrylamide (HEAm)

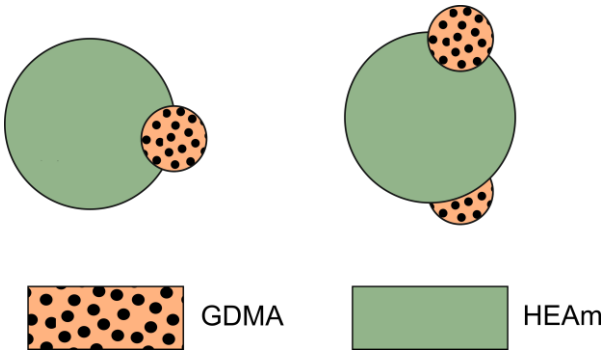

Fig. 7.2. Composition of ~500 nm doublet- and triplet-shaped Janus particles. Shape was confirmed by scanning electron microscopy (SEM) by Butterworth et al [26].

Particles were dispersed in 5CB at a concentration of 1 %, and used to fill 5µm Linkam planar-aligned cells. At a magnification of 50x, individual particles could not be distinguished visually, though large aggregates were visible. No evidence of defects surrounding the particles was identified, suggesting that the particles were in the weak anchoring regime.

The total elastic energy of distortions around a particle scales with the elastic constants and particle radius $\sim Ka$, and the anchoring energy scales like the surface area of the particles and the polar anchoring energy, $\sim W_\theta a^2$ [27]. The strong anchoring condition is found when $a \gg K/W_\theta$ and weak anchoring when $a \ll K/W_\theta$. It should be noted that the Rapini-Papoular potential W_θ can differ by several orders of magnitude (10^{-6} to 10^{-3} Jm^{-3}) depending on the combination of substrate and liquid crystal.

7.3 ~50 µm Janus Particles

Uniquely among Janus particles, it is possible to purchase particles commercially at a large size regime, the smallest available being 50 µm in diameter. We purchased some particles of this size from Cospheric LLC. Although details on the composition are not available due to commercial confidentiality, we know that the particles are based on polyethylene. The particles were developed specifically for Gyricon-like displays described in chapter 1. The particles are opaque, built on a paramagnetic, highly absorbing core (black), with an optically reflective (white) coating, shown in Fig. 7.3 below.

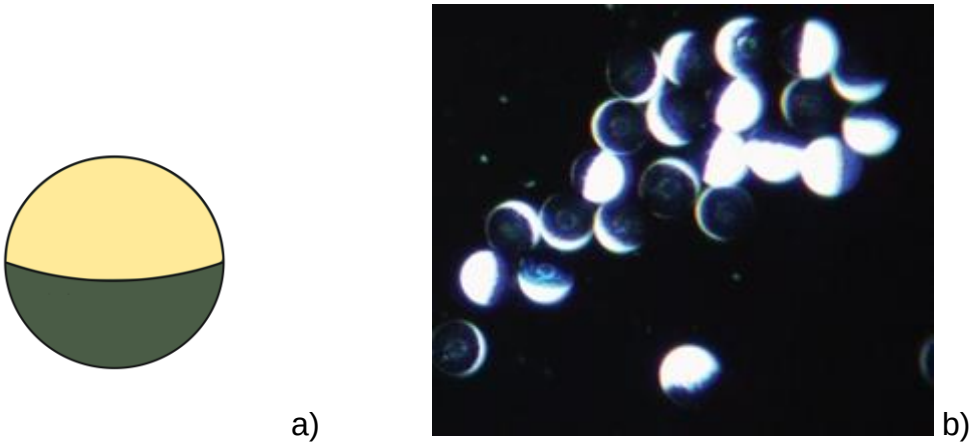

a) b)

Fig. 7.3. Approximate shape of 50 µm Commercial Janus Particle, with photograph (from Cospheric LLC). Composition is not known, but is based on polyethylene with some additives.

We placed a small amount (~1 mg) of particles in a vial and added ~100 mg of 5CB. The mixture was used to capillary fill a cell. There are several remarks about the experimental study of this mixture that can be made.

Firstly, due to the large size of the particles, the cell containing them had a large cell gap (100 µm) resulting in slow switching speeds (response time scales as the square of the cell gap). Secondly, and disappointingly, the particles sedimented to the cell substrate before any results could be obtained for particles in the bulk (for example, on heating and cooling, no movement of particles could be seen).

At 26 °C, density of 5CB is 1.02 kg/m^3 [28]. Based on the density of the core particles, which have a density of ~1.20 kg/m^3. One can apply Stokes' law at low Reynolds numbers (< 0.1), to show the sedimentation rate:

$$w = \frac{2\left(\rho_{particle} - \rho_{fluid}\right) g a^2}{9\mu} \quad \text{Eqn. 7.1}$$

,

where μ is the dynamic viscosity of the fluid. Since the sedimentation rate is proportional to a^2, we should expect a sedimentation rate due to gravity 100 x that of the 5 μm particles and 10,000 x that of the 500 nm particles.

7.4 ~5 μm Janus Particles

We were able to obtain some particles in an intermediate size regime, between 1-10 μm which would be expected to stay dispersed in the LC for much longer timescales. Based on our previous results, we expected this size regime to be a good compromise between the smaller particles, which did not appear to show satellite defects and were difficult to observe under optical microscope, and larger particles, which sedimented quickly and had to be placed in a large cell. As a first step, we were most interested in determining the surface alignment on the particles.

These particles were manufactured[5] by a bottom-up method based on Okubo et al [29]: like the 500 nm particles, the method was based on seeded polymerisation. The particles are composed of two well-known polymers, Poly(methyl methacrylate) (PMMA) and polystyrene (PS). The chemical structure of PMMA and PS is shown in Fig. 7.4 below, and the shape of the particles is represented in Fig. 7.5 below. An optical photograph of the particles is also shown in Fig. 7.6, suspended in water.

[5] Manufactured by A. Leeson et al, School of Chemical and Process Engineering, University of Leeds

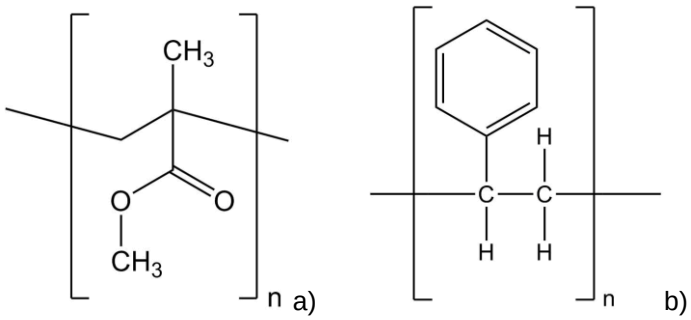

Fig. 7.4. Chemical structures of a) PMMA and b) PS. The structure of the particles is intermediate between spherical and doublet-shaped. Particles were approximately ~5 μm in diameter, but were quite polydisperse, with some of the smaller particles half the diameter of the largest.

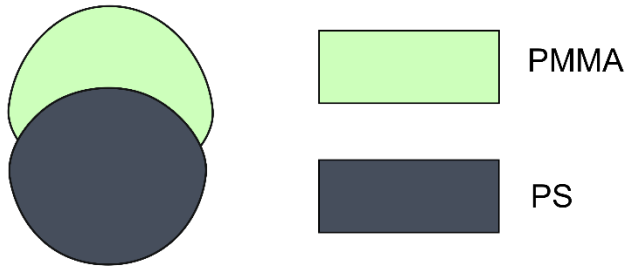

Fig. 7.5. Approximate shape and composition of ~5 μm Janus Particles.

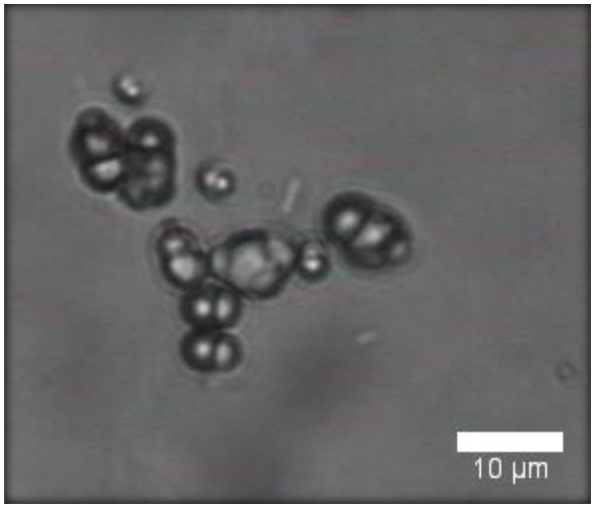

Fig. 7.6. Janus particles suspended in water. Note that the particles are very polydisperse, and variations in Janus particle morphology can be seen.

Originally, the particles were in a suspension 1 % by weight in water. To remove the water, particles were centrifuged at 10 krpm for 90 s. The remaining water was evaporated at 50 °C for 2 hours. On observing under a microscope, the particles do not appear to be damaged by the process of removing them from suspension. Approximately ~1mg of particles were added to a clean vial, then ~100 mg of 5CB was added to the vial, aiming for ~1 % density of particles (in practice, the density varied throughout the sample and was usually lowest at the centre of the cells). The mixture was vortex mixed for 1 minute at 1600 rpm.

7.4.1 Alignment at Surface of Particles

For observation, the mixture was used to capillary-fill a cell with a 10 µm cell gap. This cell gap was chosen to make it easiest to determine alignment in combination with a lambda wave plate. To determine the orientation of the director around the particles, polarising microscopy was employed with the addition of a lambda wave plate with a retardance of 530 nm. The use of a wave plate to determine the orientation of the optic axis of a material is described fully in chapter 3, and a diagram is reproduced in Fig. 7.7 below for convenience.

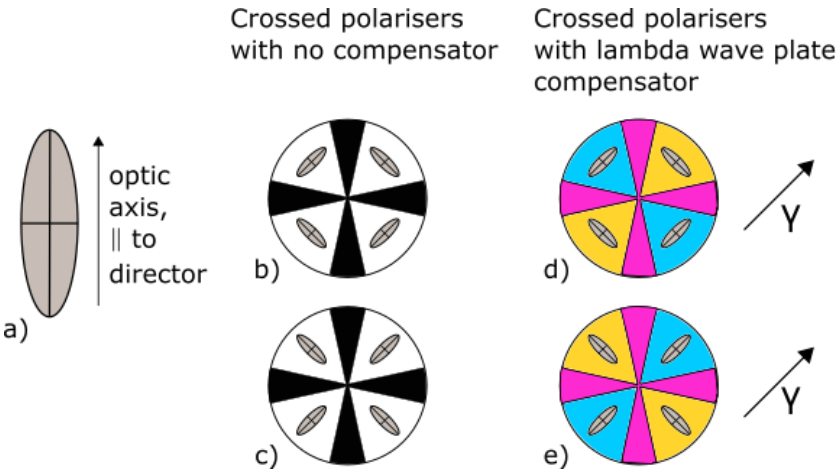

Fig. 7.7. Reproduced from chapter 3. In conventional polarising microscopy, the orientation of the optic axis in the x-y plane cannot be determined. If a lambda waveplate (vibration direction γ) can be inserted at 45° to the crossed polarisers, one can determine whether the optic axis is lying parallel or perpendicular to the vibration direction of the wave plate. The birefringence colours are either additive (e.g. blue) or subtractive (e.g. yellow).

We first observed some particles without any surface treatment dispersed in 5CB, in hand-made 10 µm cells treated with PVA to promote planar alignment within the cell (see chapter 3 for method). By observing the birefringence colours, we estimated the orientation of the director around the particles, as according to Fig. 7.7. Additive colours are observed when the director is parallel to the vibration direction of the lambda wave plate, and subtractive colours are observed when the director is perpendicular to the vibration direction of the lambda wave plate. We observed several particles, but most appeared to have approximately planar alignment (Fig. 7.8 below).

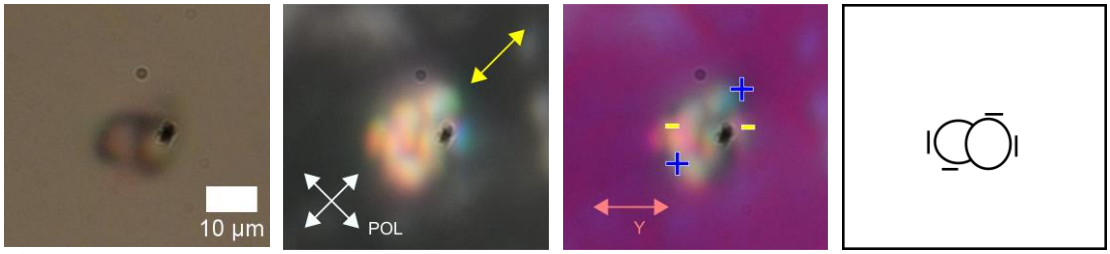

Fig. 7.8. Janus particle without DMOAP treatment under a) optical microscope, b) polarising microscope (rubbing direction shown with yellow arrows) c) polarising microscope with lambda plate, vibration direction shown with γ. From the subtractive and additive birefringence colours (represented by blue (+) and yellow (-)) we estimated the orientation of the director shown in d). In this case, the alignment appears to be approximately planar.

We were interested to see if we could promote anisotropy in surface anchoring as well as shape anisotropy. So, we treated the particles with DMOAP by the same method as in chapter 6. Photographs of the particles after treatment with DMOAP are shown in Fig. 7.9, Fig. 7.10, and Fig. 7.11 below, as optical microscopy only, then polarising microscopy without and with lambda plate respectively, then finally a representation of the likely orientation of the director at the surface of the particles, given the results of the polarising microscopy.

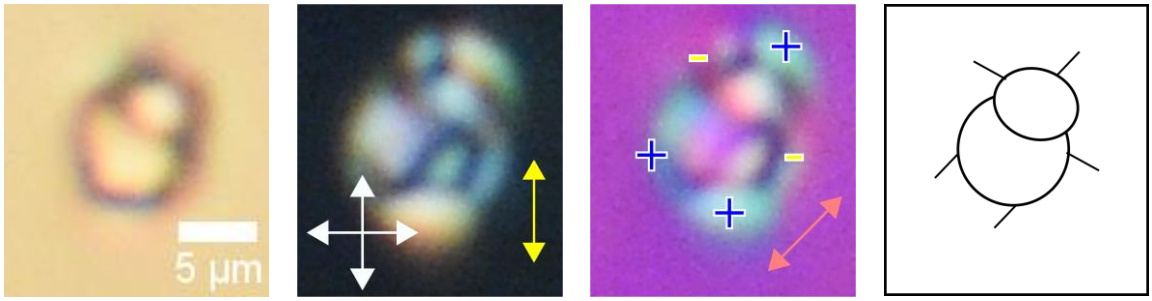

Fig. 7.9. Janus particle with DMOAP treatment under a) optical microscope, b) polarising microscope (rubbing direction shown with yellow arrows) c) polarising microscope with lambda plate, vibration direction shown with γ. From the subtractive and additive birefringence colours (represented by blue (+) and yellow (-)) we estimated the orientation of the director shown in d). The alignment appears to be homeotropic on one side, and planar or weakly anchored on the other side.

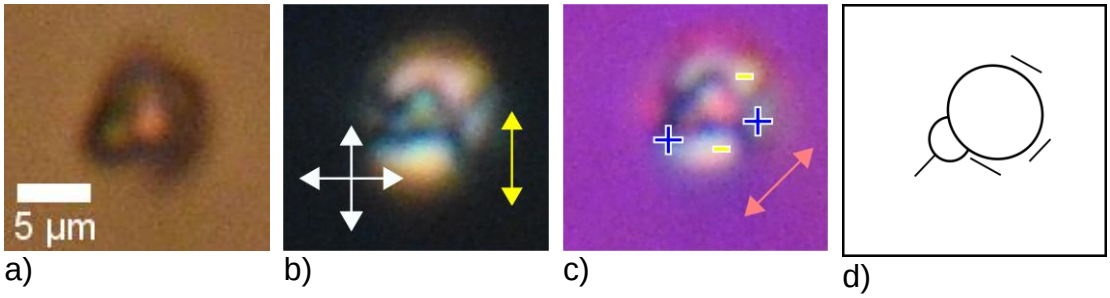

Fig. 7.10. Janus particle with DMOAP treatment under a) optical microscope, b) polarising microscope (rubbing direction shown with yellow arrows) c) polarising microscope with lambda plate, vibration direction shown with γ. From the subtractive and additive birefringence colours (represented by blue (+) and yellow (-)) we estimated the orientation of the director shown in d). The alignment appears to be approximately planar on one side, and approximately homeotropic on the other side.

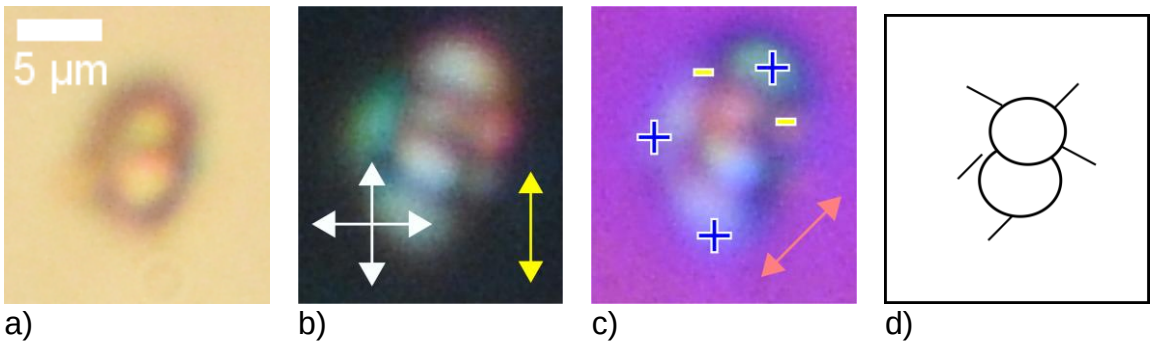

Fig. 7.11. Janus particle with DMOAP treatment under a) optical microscope, b) polarising microscope (rubbing direction shown with yellow arrows) c) polarising microscope with lambda plate, vibration direction shown with γ. From the subtractive and additive birefringence colours (represented by blue (+) and yellow (-)) we estimated the orientation of the director shown in d). The alignment was assumed to be weak on one side, and homeotropic on the other side.

On observing several particles, either the anchoring appeared to be hybrid between homeotropic and planar, or between homeotropic and weakly anchored. There may be inconsistency because the particles are not monodisperse. However, one section of the particles was always homeotropic, which suggests the DMOAP treatment affected one of the polymers (PS or PMMA) and not the other.

7.4.2 Alignment on PMMA and PS Flat Sheets

To further support the evidence of alignment, and determine whether alignment is influenced by chemical structure as opposed to shape, we tested the alignment of 5CB on flat sheets.

We received sheets of PMMA (0.20 mm thick) and PS (0.19 mm thick). Before use, we cleaned the sheets by sonicating in a solution of DI water and Decon 90 (~ 2 %) for 30 min at 50 °C, drying with compressed air, then sonicating again in a solution of DI water only for 30 min at 50 °C, and drying with compressed air.

A drop of 5CB was sandwiched between two sheets in a similar format to a cell. From polarising microscopy, it could be seen that both PMMA (Fig. 7.12 below) and PS (Fig. 7.13, below) induced similar alignment in 5CB, which was approximately planar.

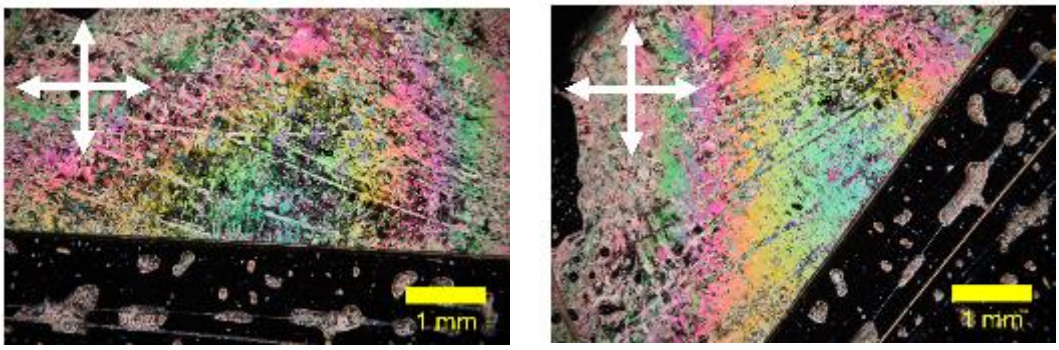

a) b)

Fig. 7.12. Alignment of 5CB on PMMA flats, where b) is rotated 45 ° relative to a). Edge of liquid crystal is shown running horizontally in a), with the liquid crystal at the top.

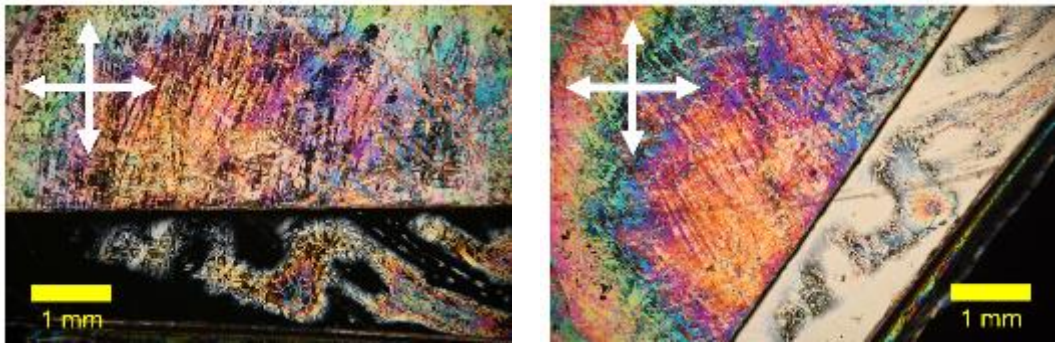

a) b)

Fig. 7.13. Alignment of 5CB on PS flats, where b) is rotated 45 ° relative to a). Edge of liquid crystal is shown running horizontally in a), with liquid crystal at the top.

The alignment on the flat PMMA and PS was consistent with our observations of particles before DMOAP treatment in Fig. 7.8. It is clear that DMOAP treatment is important, and that the untreated particles will not exhibit the unusual hybrid alignment. It appears likely that DMOAP is selectively binding to either the PS or the PMMA. We know that DMOAP binds to the OH group on glass [30], and oxygen is only present on PMMA

as opposed to polystyrene, which suggests that the DMOAP may be binding to PMMA, but not able to bind to PS.

7.4.3 Electric Field Behaviour

We also applied an electric field to the commercial cell. We attached electrodes and applied a waveform of 7 V_{RMS}. A small number of the Janus particles appeared to undergo some rotation and translation under application of the field, as observed in Fig. 7.14 below.

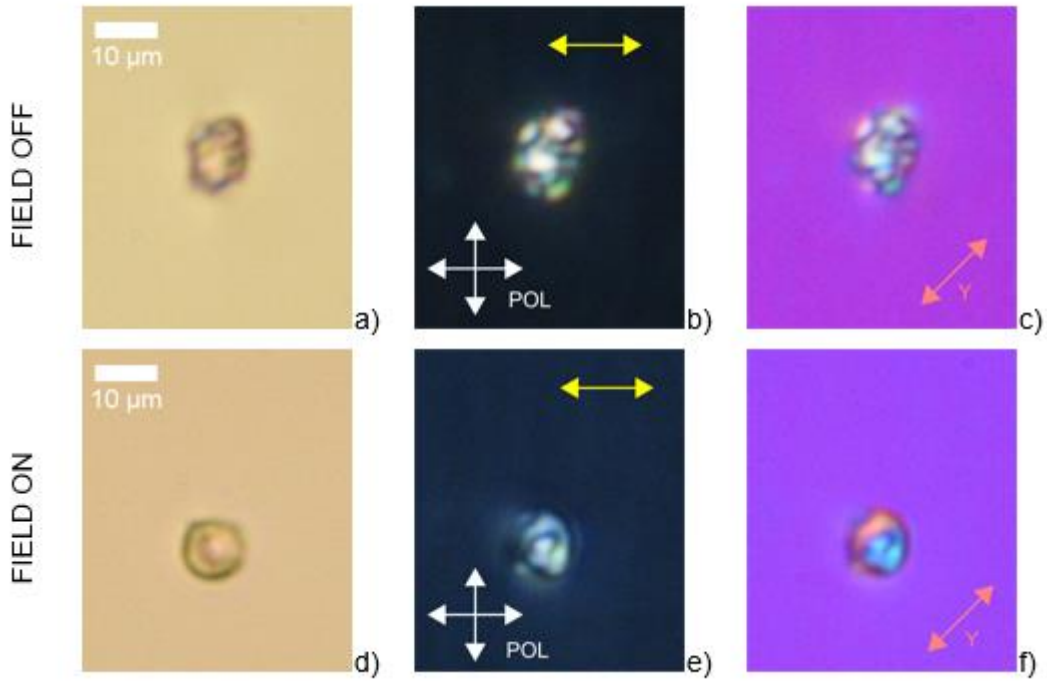

Fig. 7.14. Some Janus particles appeared to undergo some movement when the electric field is applied. Movement is reversible for at least 3 on-off cycles. The displacement is a similar magnitude to the particle diameter.

The effect was not consistent, and only seen in less than 10 of more than 50 particles. This could be because most particles become attached to substrates before application of the field.

7.5 Discussion and Conclusion

The main conclusion of looking at three types of Janus particles is that the size regime is highly important to any observations made in a liquid crystal. Larger particles (~50 µm or above) require very large cell gaps. Smaller particles (500 nm or less) are difficult to observe optically, and are likely to be in the weak anchoring regime. The 5 µm particles were at a scale that is relatively easy to observe in a liquid crystal. Without DMOAP-treatment, the anchoring appeared to be approximately planar, the same alignment found for untreated flat sheets of PMMA and PS. This suggests that the addition of DMOAP is required for the hybrid alignment. After treatment of the particles with DMOAP, there was some suggestion that the particles may be able to produce hybrid alignment. Furthermore, on application of an electric field, some particles were found to undergo rotation/translation. This seems promising in terms of building a Janus particle based device which uses liquid crystals, our original aim. If position can be further controlled with defects in the bulk of the liquid crystal, as explored in chapters 5 to 6, we may have more possibility to control the position of the Janus particles. In this chapter we demonstrated the first time possible hybrid alignment has been observed for polymeric particles in liquid crystals, without the use of any top-down techniques such as vapour deposition in the manufacture of the particles.

The process of synthesising Janus particles is still under development, and we believe it would be best to continue this work when particles are available which are more monodisperse and consistent in shape. We will discuss some more suggestions for Janus particle experiments in the next chapter.

The next chapter will be the final chapter in this thesis. As well suggestions for further experiments, we will be summarising and discussing the main conclusions of this project, and relating them to our original aims.

References

1. P.-G. De Gennes, Angewandte Chemie International Edition **31**, 842 (1992).

2. D. Patra, S. Sengupta, W. Duan, H. Zhang, R. Pavlick, and A. Sen, Nanoscale **5**, 1273 (2013).

3. H. Xie, Z. G. She, S. Wang, G. Sharma, and J. W. Smith, Langmuir **28**, 4459 (2012).

4. Y. Zhang, H. F. Chan, and K. W. Leong, Advanced Drug Delivery Reviews **65**, 104 (2013).

5. S. Gangwal, O. J. Cayre, and O. D. Velev, Langmuir **24**, 13312 (2008).

6. A. Nikoubashman, E. Bianchi, and A. Panagiotopoulos, Soft Matter (2015).

7. S. A. Mallory, F. Alarcon, A. Cacciuto, and C. Valeriani, New Journal of Physics **19**, (2017).

8. C. Casagrande and M. Veyssié, C. R. Acad. Sci. Paris, Série II **306**, 1423 (1988).

9. C. Casagrande, P. Fabre, E. Raphaël, M. Veyssié, E. Raphael, and M. Veyssie, EPL (Europhysics Letters) **9**, 251 (1989).

10. J. Hu, S. Zhou, Y. Sun, X. Fang, and L. Wu, Chemical Society Reviews **41**, 4356 (2012).

11. J. Du and R. K. O'Reilly, Chemical Society Reviews **40**, 2402 (2011).

12. S.-M. Yang, S.-H. Kim, J.-M. Lim, and G.-R. Yi, Journal of Materials Chemistry **18**, 2177 (2008).

13. J. Zhang, B. A. Grzybowski, and S. Granick, Langmuir **33**, 6964 (2017).

14. D. Rodríguez-Fernández and L. M. Liz-Marzán, Particle and Particle Systems Characterization **30**, 46 (2013).

15. A. B. Pawar and I. Kretzschmar, Macromolecular Rapid Communications **31**, 150 (2010).

16. G. Zhang, D. Wang, and H. Möhwald, Nano Letters **5**, 143 (2005).

17. H. R. Sheu, M. S. El-Aasser, and J. W. Vanderhoff, Journal of Polymer Science: Part A: Polymer Chemistry **28**, 629 (1990).

18. M. Okubo, Y. Iwasaki, and Y. Yamamoto, Colloid & Polymer Science **270**, 733 (1992).

19. M. Okubo, E. Ise, and T. Yamashita, Journal of Polymer Science: Part A: Polymer Chemistry **36**, 2513 (1998).

20. J. Kim, R. J. Larsen, and D. A. Weitz, Synthesis 14374 (2006).

21. J. W. Kim, R. J. Larsen, and D. A. Weitz, Advanced Materials **19**, 2005 (2007).

22. S. Onishi, M. Tokuda, T. Suzuki, and H. Minami, Langmuir **31**, 674 (2015).

23. M. Conradi, M. Ravnik, M. Bele, M. Zorko, S. Žumer, and I. Muševič, Soft Matter **5**, 3905 (2009).

24. M. Conradi, M. Zorko, and I. Muševič, Optics Express **18**, 500 (2010).

25. M. Cavallaro Jr, M. A. Gharbi, D. A. Beller, S. Čopar, Z. Shi, R. D. Kamien, S. Yang, T. Baumgart, and K. J. Stebe, Soft Matter **9**, 9099 (2013).

26. S. Butterworth, Shape and Chemical Anisotropic Particles in Low Dielectric Constant Media, University of Manchester, 2013.

27. O. D. Lavrentovich, Soft Matter **10**, 1264 (2014).

28. J. Deschamps, J. P. M. Trusler, and G. Jackson, Journal of Physical Chemistry B **112**, 3918 (2008).

29. N. Saito, Y. Kagari, and M. Okubo, Langmuir **22**, 9397 (2006).

30. S. D'Elia, V. Barna, N. Scaramuzza, G. Strangi, and R. Bartolino, Journal of Materials Research **24**, 2784 (2009).

Chapter 8 Conclusions and Further Work

8.1 Introduction

Our motivation for this project began with the topic of electronic paper (chapter 1). Despite huge progress being made in display technology in the past few decades, we are still some way from developing electronic paper that can perform at video-rate [1,2]. While there may be a number of paths to creating such a display, our starting point was two existing display types, the electrophoretic display, and the liquid crystal display. Is it possible to combine the desirable optical properties and low power of an EPD with the speed of an LCD? In the literature, some prototype devices have already been built that use particles suspended in liquid crystals [3–8]. While some of these prototypes were promising, there are still many problems to be overcome in order to develop a commercially viable device. We also discussed the possibility of, rather than using the migration of particles to build a device, instead using the rotation of particles. Perhaps a device could be built that is similar to the Janus particle based device, the Gyricon [9,10].

The subject of liquid crystal colloids is highly complex. In chapter 2 we summarised some of the important physical properties of liquid crystals and colloids, both of which are complex topics in their own right. The combined systems, ‘liquid crystal colloids’ have some unusual properties, for example, long-range elastic forces, and topological ‘satellite defects’ associated with particles. These properties all affect how particles in liquid crystals interact with electric fields, other particles, and defects.

We began our experiments in chapter 4. Our first aim was to identify if the bulk properties of a liquid crystal change with the addition of particles (in this case, polymeric particles of ~500 nm diameter, including some unusual doublet-shaped Janus particles). Changes in properties such as electrical and elastic properties would affect the performance of a device, positively or negatively. Most studies of liquid crystal colloids in the literature concentrate

on single particles only, or only on particles with unusual electrical, photonic, or magnetic properties (gold nanoparticles, graphene flakes etc). It was found that for our particle at concentrations of ~1% wt/wt or less, no significant change could be seen in the order parameter, refractive indices or elastic constants. At higher concentrations of particles, aggregates were formed. While aggregates in liquid crystals are an interesting topic in their own right, if our aim is to create a device based on rotating Janus particles, particles must remain separate from one another.

Given those conclusions, we decided to approach the topic of controlling the position of particles in a liquid crystal, in this case by using defects. We also changed to a larger (~1-10 μm) particle size regime in order to facilitate imaging. The topic of defects interacting with LC colloids has been studied for many different systems in the literature, but fewer studies have been both experimental and quantitative [11,12]. We wanted to see if a passive method of microviscometry (method described in chapter 3) could be used to quantify how strongly a particle is confined at a defect, and then explore which parameters are important to confinement strength. Passive microviscometry has only been rarely used to investigate particles in liquid crystal [13]. In this chapter we will be discussing some more possible experiments using this technique.

In chapter 5, we discussed the tracking system, and what the trajectories and mean square displacements of a particle might be predicted to look like for confined and free particles. Our tracking results are shown and discussed in chapter 6. Confined particles indeed show trajectories consistent with form:

$$\langle \left(R_i(t)\right)^2 \rangle = \frac{2k_B T}{\kappa_i}\left[1 - \exp\left(-\frac{\kappa_i t}{\xi_i}\right)\right], \qquad \text{(Eqn. 8.1)}$$

from which we calculated ‘confinement strengths’, κ. Confinement strengths are of the order of a particle confined at a laser trap [13] or higher.

Anchoring conditions appeared to be significant, with particles with ‘strong’ anchoring and satellite defects appearing more confined than particles with

weak surface anchoring. Confinement strength was also affected by liquid crystal type, with more confinement in an LC with larger splay and bend elastic constants. Cell gap also had an effect, with very large confinement experienced when cell gap was ~2 x the particle diameter. In this regime it may be difficult to determine which part of the confining force is caused by surface interactions and which is caused by elastic deformations in the LC. Particle size within the size range 2 µm - 5 µm diameter did not have a large effect on confinement strength for significantly different particle size to cell gap. Since the behaviour of the particles in the 5 µm particle size range and a cell gap much larger than the particle diameter is better understood, using that size range and cell gap would be recommended for any experiments that expand on the results in chapter 6.

Our last set of experiments returned to an unusual particle geometry, the Janus particle. Janus particles have only recently become available at the micron scale, and in this case, not commercially. We found evidence of hybrid alignment, and some evidence of particles rotating in an electric field, which could be potentially used to build a device, although this was not observed for all particles. This is not the first time hybrid alignment for particles in liquid crystals has been reported [14,15], but it is the first report of hybrid alignment for particles built by a bottom-up method, which allows a different scope for mass production, fine-tuning and customisation of particles.

Based on what we found so far, this final chapter contains recommendations for new experiments, any preliminary work that might inform these experiments, and suggestions for overcoming potential challenges. We also discuss which methods may be used to perform these experiments.

8.2 Particles in Unusual Nematic Phases above Room Temperature

In chapter 6, we conducted most of our results in the well-known liquid crystal 5CB, and a second liquid crystal (MLC-6648) with low birefringence.

Both have only one possible liquid crystal mesophase, the nematic phase, and both liquid crystals exist in the nematic phase at room temperature (~25 °C). However, we know that a wider range of elastic constants and their ratios can be exhibited in liquid crystals that have a non-calamitic geometry or more than one liquid crystalline mesophase, particularly when approaching the transition between mesophases. The examples we are going to consider are 8CB and bent-core liquid crystals. In these cases, as we will see, the elastic constants behave in an unusual manner. It would be interesting to observe particles trapped in defects in such systems, since we already found that that elastic constants have a significant effect on confinement. We might also be able to start investigating the effect of elastic constant ratios, allowing a deeper insight to particle confinement than is considered in most theoretical studies that consider just the single elastic constant approximation. Simulations have shown that the ratios of elastic constants influence the structure of defects [16] and an extension of the experiments that we have carried out here, would be an excellent way of probing more details of defects.

Conducting such experiments would require significant modification to the laser tweezing and particle tracking setup described in chapter 4, as experiments would no longer being conducted at room temperature. A typical commercial microscope hot stage would not be sufficient because of the geometrical constraints of the experiment. The inverted microscope already requires a specialist hot stage in order to secure the sample and in order to extract useful physical information near to the transition temperature, temperature control must be fine, ideally to within ± 0.2 °C. The fine temperature control may not be straightforward to achieve, since the small working distance required for high magnifications means that the hot stage could not be enclosed. Even the heat conducted by the objective lens could cause significant thermal gradients in the sample [17], so the objective lens may also need to be heated to the same temperature as the hot stage. While constructing a setup with the required temperature control that is also suitable for high magnification laser tweezing is possible, the setup would

require careful design, testing, and selection of equipment. Being able to control the temperature to a precise degree would allow the investigation of some temperature ranges in certain liquid crystals where the ratios of elastic constants diverge. It would also be vital if the nematic phases of bent-core systems were to be studied. Studying these systems may allow us to determine which elastic constants are most important in the interaction between particles and defects.

8.2.1 Elastic Constants near Sm-A Transition in 8CB

In chapter 6, we looked at the relationship between liquid crystal and confinement strength, and concluded that elastic constants have an effect on strength of confinement, with larger elastic constants resulting in higher confinement. A method of investigating the relationship between elastic constants and confinement in detail would be to choose a single liquid crystal, and track the particle at different temperatures. The liquid crystal 4-n-octyl-4′-cyanobiphenyl (8CB) undergoes a Smectic-A to Nematic ($N - S_A$) transition between 33.6 - 33.8 °C [18]. The bend and twist elastic constants diverge as the liquid crystal approaches to the S_A phase [19], unlike the purely first-order transition observed in liquid crystals with only a nematic mesophase and a nematic to crystal transition [20, 21]. For comparison, take the temperature region within 1 °C of the ($N - S_A$) transition. In this region, viscosity does not change significantly (η_{22} and η_{33} change very little, and η_{33} changes by <15 % [20]). In the same region the splay elastic constant (which does not diverge) changes <15 %, whereas bend and twist change by >30% [22].

We recommend an experiment of the form in chapter 6, quantifying confinement strength for a particle in a defect in 8CB, as a function of temperature near to the $N - S_A$ transition.

8.2.2 Bent-Core Liquid Crystals

The family of ‘bent-core’ liquid crystals, of much interest in liquid crystal research [24,25], has some unique properties. In terms of elastic constants,

for most calamitic (rod-shaped) nematic liquid crystals, $K_{11} < K_{33}$, but the opposite ($K_{11} < K_{33}$) can be true for bent-core liquid crystals [26-31]. Furthermore, the temperature dependence of the elastic constants can be very different to calamitic systems.

We'll discuss the properties of two bent-core liquid crystals with elastic constants that have been studied recently. Both are oxadiazole-based and have the chemical structures shown in Fig. 8.1, but for brevity, will be referred to in this chapter as 'compound 1' and 'compound 2'.

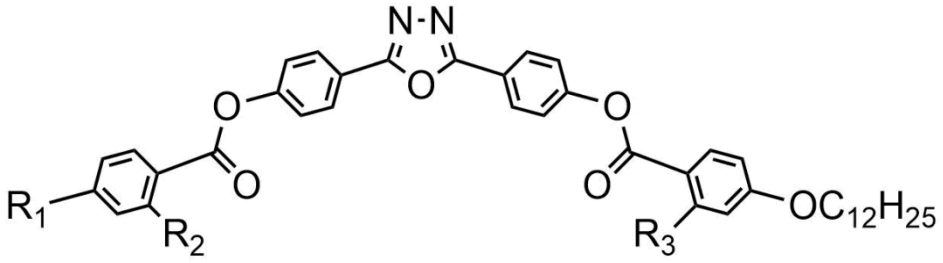

Compound 1: R_1= $C_{12}H_{25}O$, R_2 = Me, R_3 = OMe **Iso 115 N 88 SmX 64 Cr**

Compound 2: R_1=C_5H_{11}, R_2 = R_3 = H **Iso 230 N 170 DC 100**

Fig. 8.1. Structure for two bent-core compounds, 'compound 1' and 'compound 2' [32]. The phase behaviour is also described, where Iso is the isotropic phase, N is the nematic phase, SmX is an unknown smectic phase, Cr is Crystalline, and DC is the 'dark conglomerate' phase. The dark conglomerate phases [33] consist of 'sponge-like' structures of smectic layers, and are optically isotropic.

The elastic constants of 'compound 2' were first published in 2012 [34], shown in Fig. 8.3. The splay elastic constant was found to decrease linearly as temperature approached T_{NI} (from ~8 pN to ~3 pN), and the bend elastic constant remained almost constant (~3 pN) at all temperatures in the nematic range. More recently, the elastic constants for 'compound 1' were published, along with mixtures of compound 1 and compound 2 [32]. The elastic constants of 'compound 1' are shown in Fig. 8.2. It was found that

‘compound 1’ had an unusually small value of K_{33}, (~1.2 pN), in combination with temperature independence.

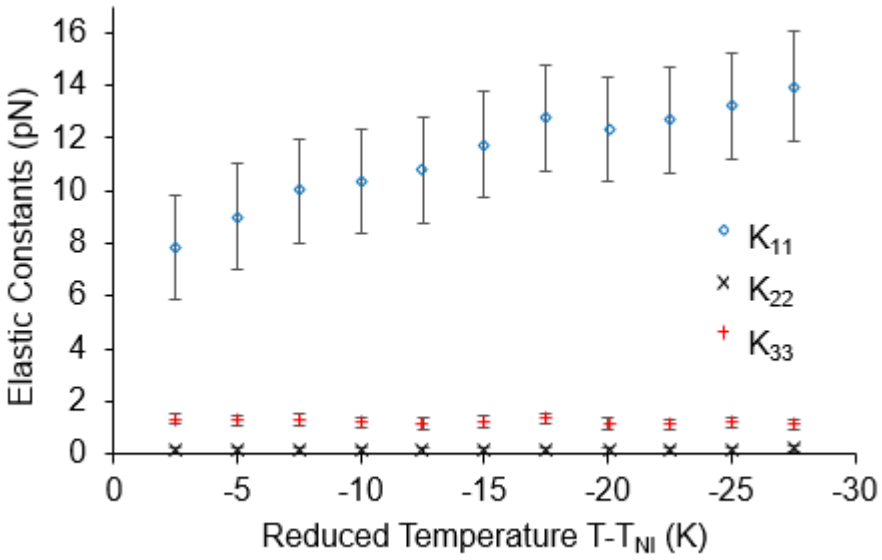

Fig. 8.2. The elastic constants of 'Compound 1'. Reproduced from data published in [32], with permission. At low temperatures, the nematic phase approaches an unknown smectic phase.

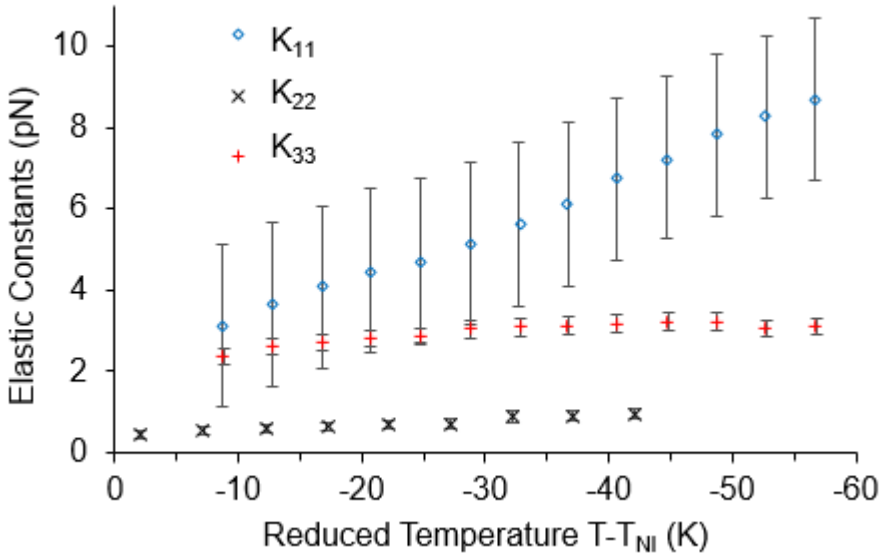

Fig. 8.3. The elastic constants of 'Compound 2'. Reproduced from data published in [34], with permission. At low temperatures, the nematic phase approaches the dark conglomerate phase.

We can also see that the elastic constant ratios of the elastic constants change over the nematic ranges for both these compounds, as shown in Table 8.1.

		Elastic Constant Ratio (dimensionless)		
		K_{11}/K_{33}	K_{22}/K_{33}	K_{11}/K_{22}
5CB	Low temp	0.9	0.5	1.8
	High temp	0.8	0.4	1.9
Compound 1	Low temp	1.3	0.17	5.8
	High temp	2.8	0.12	7.6
Compound 2	Low temp	5.9	0.10	61
	High temp	12.4	0.18	67

Table 8.1. Ratios of elastic constants for compound 1 [32] and compound 2 [32] in the nematic range. 5CB is included for comparison [35].

Given the unique properties of the elastic constants in bent-core liquid crystals, it would be interesting to study particles' confinement in defects, particularly near to the smectic phase. As with the Smectic A system, keeping the particles suspended in the bulk would require the temperature of the sample to be maintained at a value large enough to keep the liquid crystal in the nematic phase or above. In order to avoid particles being ejected during the manufacture of the sample, cells can be filled in situ on the hot stage, by placing dried particles along the edge of the cell. 8CB was added by spatula, and drawn into the cell by the liquid crystal.

8.2.3 Particles in Lyotropic and Chromonic Phases[36, 37]

All the work on liquid crystals in this thesis has been conducted on thermotropic liquid crystals. In other words, all experiments in the thesis were conducted on liquid crystals with highly temperature dependent phase behaviour. None of the experiments were performed on 'lyotropic liquid crystals', another family of liquid crystals with phase behaviour that depends

on concentration in a solvent instead of temperature. It might be interesting to explore the behaviour of particles in a lyotropic system, for reasons which will be discussed below.

Lyotropic phases are the first liquid crystals to be studied scientifically [38], with work on the lyotropic liquid crystal myelin published as early as 1854 [39], predating the earliest work on cholesteric liquid crystals by several decades [40, 41]. Lyotropic phases are typically formed by ‘amphiphilic’ molecules. Amphiphilic molecules are single molecules, within which different regions of the molecule have different interactions with a solvent. A ‘solvent-loving’ part, usually a group with a positive or negative charge is attached to a ‘solvent-hating’ part, typically one or more hydrocarbon chains. An example of an amphiphilic molecule which forms lyotropic phases is sodium dodecyl sulphate (SDS), also known as sodium lauryl sulphate (SLS). SDS is used commonly as a detergent, e.g. in household cleaning products, shampoos and toothpastes. The structure of SDS is shown in Fig. 8.4 below.

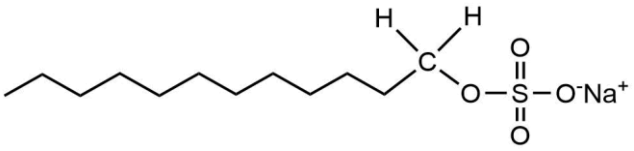

Fig. 8.4. Chemical structure of SDS ($CH_3(CH_2)_{11}SO_4Na$). The nonpolar hydrocarbon chain is not soluble in water (hydrophobic). The sodium ion is polar, and highly soluble in water (hydrophilic). In addition to its usefulness as a detergent, SDS also forms liquid crystalline phases at certain concentrations in water.

The interactions between the parts of the amphiphilic molecule and the solvent prompt the amphiphilic molecules to ‘self-assemble’ into structures that are often liquid crystalline in nature. Some examples of structures formed by amphiphilic molecules are shown in Fig. 8.5 below.

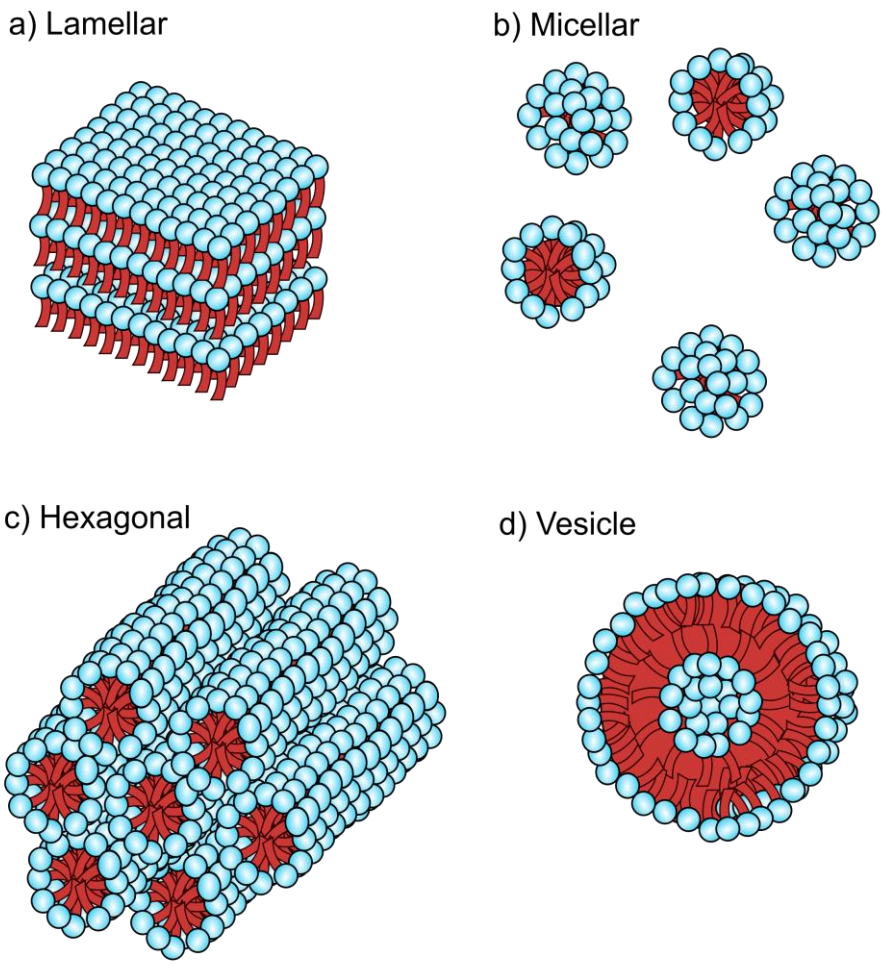

Fig. 8.5. A variety of phases and structures associated with lyotropic liquid crystals. Amphiphilic molecules may form lamellar (a) and hexagonal (c) phases at high concentrations, and micelles (b) and vesicles (d) at lower concentrations. The structure adopted will depend on the type of solvent and solute molecule, and the concentration. Temperature is also a factor. Note that not all of these structures represent examples of liquid crystals. For example, a suspension of micelles (b) and/or vesicles (d) does not exhibit any type of long-range order, which would be required for a liquid crystal.

The length scales of the structures that form depend on the dimensions of the amphiphilic molecules. Molecular dimensions are on the scale of ~1 nm. As the density is high, the layers in a lamellar phase will be spaced apart ~1 nm (measured for SDS in water [42]), and micelles have diameter also on

the scale of ~1 nm (measured for SDS in water [43]). This length scale is much smaller than the ~µm size of particles investigated in this thesis.

The structure most relevant to larger particle scales may be vesicles (hollow, enclosed structures with a bilayer of amphiphilic molecules), which can be at least ~1 µm in size. Vesicles are also a features of cell biology, as enclosed structures formed by lipid bilayers play a vital role in transport, storage and communication [44]. The size of vesicles in cell biology depends on function, but can range from ~10 nm to several µm. Fluorescent labelling and tracking of substances within a cell is already a subject of great interest in biology [45], and combining this with analysis similar to that conducted in chapter 5 and 6 may offer insight into how substances are stored and transported on this scale in biology. Thus, the proposal would be to use lyotropic liquid crystal systems as model structures to examine the potential of tracking particle motion to understand defects in such structures.

There is a second family of lyotropic liquid crystals that form phases following the self-assembly of flat molecules into stacks, the chromonic phases [37]. The mechanisms behind the formation of chromonic phases are a subject of current research as they are less well understood than other lyotropic systems. However, it is known that the molecular stacking occurs to minimise the interactions of hydrophobic (usually aromatic) parts of the molecule with water, while maximising the interactions between water and the solubilising units.

One of the best studied examples of a material forming chromonic phases is ‘Sunset Yellow’ (Disodium 6-hydroxy-5-[(4-sulfophenyl)azo]-2-naphthalenesulfonate), abbreviated SSY [37, 46]. The chemical structure of SSY is shown in Fig. 8.6 below.

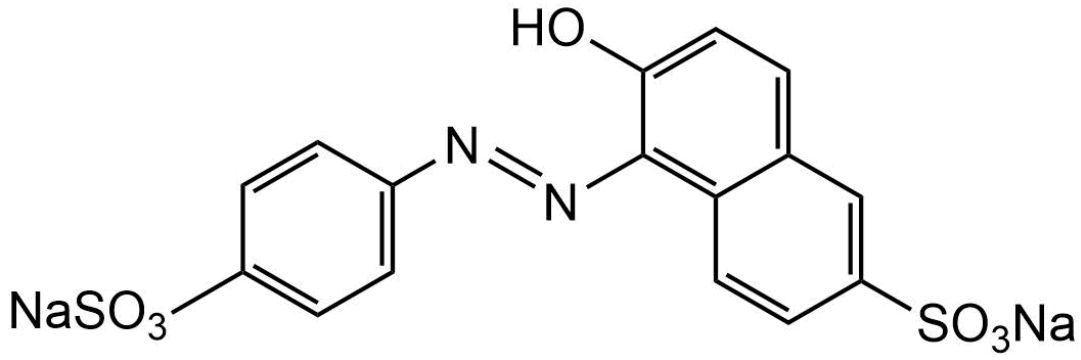

Fig. 8.6. Chemical diagram of sunset yellow.

Sunset yellow is commonly used as a dye in food [47, 48], medicines [48] and cosmetics [48]. Like many thermotropic liquid crystals, SSY forms a nematic phase. The nematic phase can be observed under a polarising microscope forming Schlieren patterns similar to that in a thermotropic nematic such as 5CB [46]. Unlike a conventional nematic liquid crystal, the nematic phase is formed by stacks of molecules [49, 50] represented in Fig. 8.7 below.

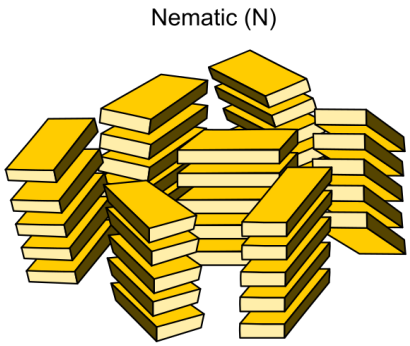

Fig. 8.7. Representation of a nematic (N) phase formed by stacks of molecules in a chromonic liquid crystal such as SSY. [49, 50]

There are still aspects of chromonic liquid crystal assembly that are still not well understood, such as how the molecular structure of the LC affects self-assembly, and also the kinetics behind formation of the stacks [51]. Another challenge related to chromonic liquid crystals is alignment. Uniform alignment of chromonic liquid crystal was first reported as recently as 2010 [52], using specialised methods of substrate manufacture. A method of alignment based on mechanical rubbing of the substrate by an abrasive was recently demonstrated by Collings et al [53]. In 2015, the same group added micron-scale particles to the system and reported self-assembly of particles into chains similar to that found in thermotropic nematic liquid crystals [54]. Most recently, passive microviscometry was used to measure the viscosity of a chromonic liquid crystal system [55].

There is scope to investigate how particles interact with defects in a chromonic liquid crystal, and determine whether the behaviour is quantitatively or qualitatively different to that in a thermotropic system. For example, the elastic constants in chromonic liquid crystals have some unusual properties. In 2012, a group measured the elastic constants of SSY by using magnetic field [56]. It was found that K_{11} and K_{33} are similar to in thermotropic liquid crystals, but K_{22} was one order of magnitude smaller. Furthermore, the ratio of K_{11}/K_{33} and K_{11}/K_{22} increase when the concentration of SSY increases, or when the temperature of the system

decreases. Carrying out such experiments would be especially interesting if the outcome was compared to bent-core systems where similar extremes of elastic constants are known.

8.3 Particle Interaction with Defects

In chapter 6, the defects we created were due to domains of planar alignment at the substrates in a Schlieren cell. This meant we were somewhat limited in the control we had over the shape of the defects. Having more control over the director structure might allow us more insight into the systems, both qualitatively and quantitatively.

There are a number of methods that have been used in the literature to create non-uniform alignment patterns of liquid crystals on a substrate, though currently all of these methods require specialist materials and equipment. A radially symmetric rubbing pattern can be produced in a similar manner to the standard method of planar rubbing. Using a circular lathe, it is possible to create radially symmetric alignment patterns, containing a defect in the centre of the pattern [57]. Most recently, a research group succeeded in using an atomic force microscope to ‘draw’ radially symmetric patterns onto a substrate, creating defects in the bulk, and successfully demonstrated particles being attracted to the defects [58]. Another method of creating ‘patterned’ substrates is to use a procedure called ‘photoalignment’. This method involves using polarised light to selectively excite molecules in the alignment material [59]. Advances have been made in this technique in recent methods, allowing the creation of arrays of arbitrary patterns [60,61]. Photoaligned surfaces have already been used in LC colloid experiments in the literature [62-64].

Another way to create defects is to use a substrate that has a structure protruding into the bulk. There are a number of papers beginning to investigate interactions of particles with defects associated with structures. For examples, particles have been found to assemble around defects around micro-posts [65] and assemble along channels [66] have been studied in the lab, and others have been simulated, such as dimples [67].

Photo-patterning, gratings and similar techniques would be required if one wished to control the position of a large number of particles, as would be required in a device. It is not yet known if self-assembly on this scale is possible without the intervention of an additional tool such as laser tweezers.

In all of these cases the interesting feature is that non-standard topological defects can be created. For example the AFM-patterned system produced high-order defects (all of the ones we've considered have been $\pm^{1}/_{2}$); examining the confinement or interaction of particles with higher order defects would certainly be interesting. More speculative, would be the interaction of particles with chiral defects – skyrmions – that have also been produced using sophisticated patterning. There are several levels to the interest here. Again, rather fundamental, is the interaction of isotropic particles with such defects. The next level of interest would be how asymmetric particles, such as the Janus particles, with the asymmetric director field. Finally, it would be interesting to examine the confinement of multiple particles at such sites. Skyrmions are well-known in condensed matter physics and are important topological defects in spintronics. Understanding how particles might interact with skyrmions in a tractable, soft matter system, would be an interesting 'playground' to shed insight into the much less tractable hard condensed matter analogue.

8.4 Particles

8.4.1 Nanoparticles

In chapter 6, we found that particle size affects the surface alignment in a liquid crystal. In parts of chapter 6, we looked at particles in the strong anchoring regime, in this case 2 μm in diameter and larger. In chapter 3, we looked at 'small' particles, assumed to be in the weak anchoring regime, in the size regime of ~500 nm. However, we have not yet considered the 'nano-scale' regime of ~10 nm and smaller. This size regime is of interest both in terms of particle interaction with defects, which may be different to

particles on a larger scale, and because a number of specialised particles such as quantum dots (which may be useful in devices due to their optical properties) are only produced at this small size regime. Despite the challenges encountered in chapter 3, imaging of nanoscale particles is still possible with the use of specialist particles and imaging techniques. For example, dark field microscopy has been used to image particles of 20 nm diameter in a liquid crystal by using dark field microscopy [68].

Some particles in the nano-size regime can be imaged using fluorescence microscopy. In particular interest are the new super-resolution microscopy techniques, a family of fluorescence microscopy methods that surpass the diffraction limit [69-71]. The diffraction limit, $(d = 0.61\lambda/\mathrm{NA})$ in practice restricts most optical microscopy to resolving objects ~250 nm apart or further. We will be considering two super-resolution optical microscopy techniques, stochastic temporal optically resolved microscopy (STORM) [72] and structured illumination microscopy (SIM) [73]. SIM involves illuminating the sample with periodic illumination, usually a grating. The image of the sample superimposed by the grating produces ‘moiré fringes’ (similar to ‘beat frequencies’ in sound). From the moiré patterns, information can be obtained at higher spatial frequencies than is possible with conventional microscopy.

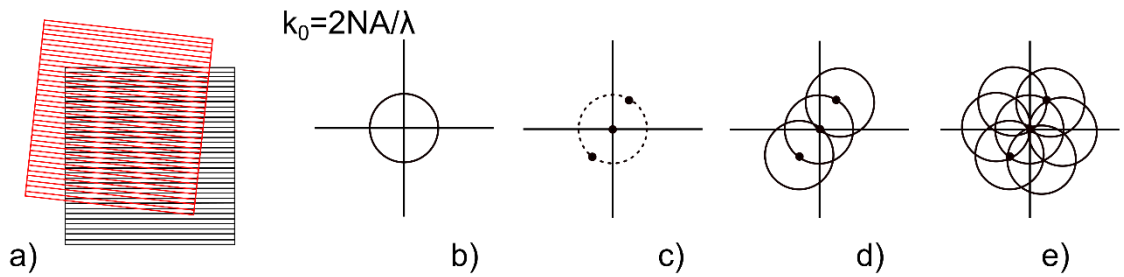

Fig. 8.8. Illustration of SIM, adapted from [73]. Moiré fringes are generated from overlapping structures, such as these two periodic gratings in a): the moiré fringes are the 'vertical stripes' seen at the overlap between the two gratings. In reciprocal (or Fourier transform) space, further from the centre represents higher spatial frequencies. The highest special frequencies resolvable by conventional microscopy are shown in b). The Fourier transform of a sinusoidal pattern can entirely be encoded in three points in c). Superimposing the illumination onto a sample increases, as seen in d). Using other orientations of the illumination pattern can increase the amount of reciprocal space (and therefore spatial frequencies) still further, up to ~2x.

STORM uses fluorescing molecules, taking advantage of certain types where only a random (stochastic) fraction of the fluorophores may be illuminated at any one time. Since finding the centre of a fluorescing probe can be determined much more precisely than the resolution limit (even as small as ~1 nm [74]), using STORM allows very high resolutions.

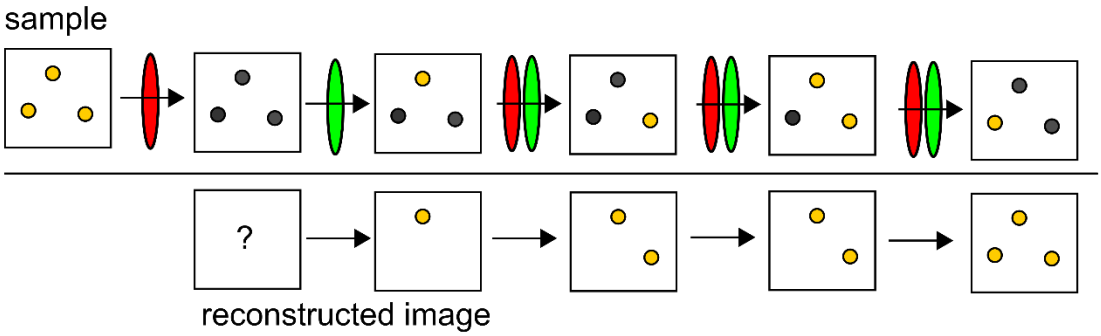

Fig. 8.9. Illustration of STORM, adapted from [72]. Fluorophores are put into a non-fluorescing 'dark' state when illuminated by a laser pulse (e.g. red). When illuminated by a second laser pulse (e.g. green), some proportion of the fluorophores will fluoresce. With repeated cycles of illumination, an image of the fluorophores can be built up. Fluorophores may be much closer together than the resolution limit, even at separations as small as ~20 nm.

Experimental time was won at the Central Laser Facility (CLF) at the STFC Rutherford Appleton Laboratory (RAL) by JC Jones and M Nagaraj to use STORM and SIM to image the structure of liquid crystals. The proposition involved using two fluorescent dyes, BTBP (N,N′-Bis(2,5-di-tert-butylphenyl)-3,4,9,10-perylenedicarboximide), and indium phosphide (InP) nanoparticles (20 nm diameter). We designed and manufactured a number of samples as part of this project, although the final analysis was conducted by Jones and Nagaraj. Samples were constructed to the same method described in chapter 4, using thin cover slips due to the high magnification needed.

One of the samples manufactured was based on the Zenithal bistable device. The ZBD contains a periodic grating, shown Fig. 8.10 and Fig. 8.11. We were interested to discover whether the InP nanoparticles were attracted to the defects in the ZBD's D-State. Potentially, a similar system could be used to build a switchable photonic device.

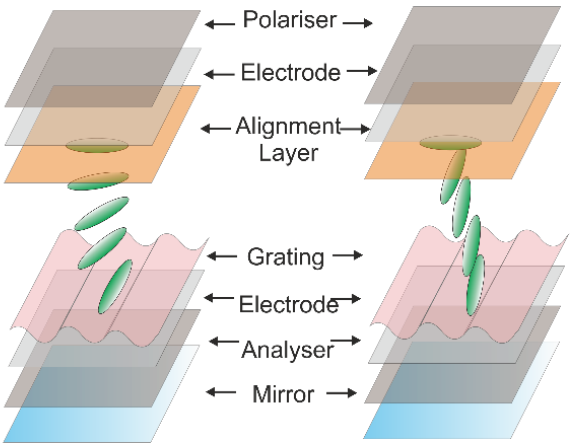

Fig. 8.10. Construction of ZBD. The 'defect state' D-state (left) and 'continuous state' C-state (right).

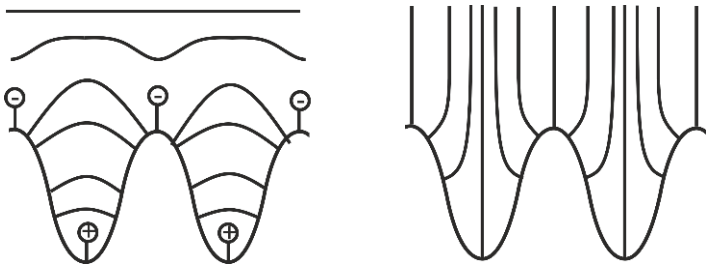

Fig. 8.11.Cross-section of ZBD grating in D-State and C-State. In the D-state negative -1/2 defects (-) are formed at the concave surface at the top of the grating, and positive +1/2 defects are formed at the concave surface at the bottom. Note that the commercial ZBD has a grating with 0.8 μm pitch and 1.0 μm amplitude [75].

When doped with InP quantum dots, and submitting to the same procedure as STORM, we found that the quantum dots assembled along the defects in the D-state. Continuation of this work is ongoing by other members of the group. Note that since performing this experiment, another group found similar results of assembly of particles at defects imaged by STORM [76].

8.4.2 Other Particle Geometries at Micron Scale

Due to developments in manufacturing techniques, especially photolithography [77, 78] and microfluidics [79-81], there is now a large number of particle shapes that can be manufactured on the micron scale. A non-exhaustive list of microparticle shapes which have been added to liquid crystals in the literature include knots [82], spirals [83], and assemblies of cuboids [84]. Each shape gives rise to a unique combination of surface alignment and in some cases, associated satellite defects (for example, radial defects stabilised at the centre of ring-shaped particles [82, 85]).

With such an algorithm in place, we would like to recommend an experiment similar to that in chapter 6, with a non-spherical particle geometry such as an ellipsoid. Note that since the non-spherical particles are no longer spherically symmetric, it would be useful to be able to record the orientation of the particles. We would recommend implementing a more specialised particle tracking algorithm, capable of recording the particle orientation as well as the centre of mass. Tracking software would be able to determine whether there is a preference for particles orienting along an axis perpendicular or parallel to a defect.

8.4.3 Continuation of Janus Particles Work

In chapter 7, we began some investigations into Janus particles and alignment in a liquid crystal. We studied three different size regimes of particle, ~500 nm diameter, ~5 µm diameter, and ~50 µm diameter. In the smallest regime, particles were found to be in the weak anchoring regime. In the largest regime, particles sedimented very quickly. However, in the 5 µm regime we saw evidence of hybrid alignment when treated with DMOAP. We saw some evidence of reorientation in an electric field, though this was not seen consistently, possibly due to sedimentation of some particles. We think this topic is worth continuing study. We did not continue with this in the short term, as improvements are taking place in particle manufacture.

Alignment around particles is highly sensitive to size, especially near to the threshold between strong and weak anchoring. Improvements are being

made to be able to synthesise Janus particles that are more monodisperse. Improvements are also taking place in the control of particle shape: for example, the micron-scale particles in chapter 7 may be made more spherical. With these refinements in particle manufacture, we would like to repeat the experiments in chapter 7.

Another limitation of the experiments in chapter 7, is that it was not possible to distinguish the composition of each half of the particle under the microscope. We did observe some particles in 5CB under a fluorescence microscope, but fluorescence from particles was dominated by fluorescence from the liquid crystal 5CB. It should be possible to synthesise the particles incorporating a fluorescent dye into either the PS or PMMA half of the Janus particle. Then, once under a fluorescent microscope, we would be able to identify which half of the particle had which composition.

Finally, we would like to make some slight modifications in order to confirm the surface alignment reported in chapter 7. With particles synthesised at 10 μm diameter as opposed to 5 μm, it may be easier to identify surface alignment. The alignment could also be tested independently of shape, by making cells with inner substrates of PMMA and PS.

Given these modifications, we would like to investigate how the Janus particles interact with defects, first without an electric field, and then in an electric field. With the addition of the modifications to shape and addition of fluorescent tag to one or both sides, it would be possible to determine whether the particles rotate in an electric field, and via what axis. Comparison of dumbbell-shaped and more spherical particles would also allow us to determine whether the defects associated with the particles depend on shape, as opposed to chemical composition.

If that research was promising, there would be some more work to be done if these particles were to be used in a device similar to the Gyricon. Several criteria would need to be fulfilled:

- Particles must rotate in an electric field, and rotation must be reversible

- Particles must have appropriate/good optical properties (i.e. highly reflective on one hemisphere, highly absorbing on the other hemisphere)

- The particles must be stable at a high enough concentration to give the finished device good optical contrast

The first criterion, rotation in an electric field not yet been confirmed. The second criterion is not fulfilled by the current µm scale polymeric particles. It may be possible to synthesise particles of that description in the future, in line with developments in particle manufacturing techniques. As for the third criterion, as mentioned in section 8.3, we have not yet demonstrated the self-assembly and/or stability of large numbers of particles.

8.5 Possible Device Applications

Returning to the original aim of the research: does this research suggest that a new type of electronic paper can be constructed? The information does not appear conclusive at this stage. Although we have demonstrated more quantitatively findings in the literature that particles can be confined at defects, we have not yet demonstrated control of particle position for large numbers of particles, which would be needed for electronic paper. A Janus-particle based liquid crystal device would require a high density of particles, possibly including a number of layers of particles, in order to achieve high contrast [9,86].

If electronic paper is not a viable application, could the research have uses elsewhere? Self-assembly of colloids is an exciting field of research within liquid crystals and elsewhere [87,88], with the possibility to create many interesting photonic structures. Liquid crystals are an exciting possibility for families of photonic structures which is switchable under an electric field. Greater understanding of particle interactions with defects may help future researchers to design a variety of self-assembled photonic structures.

8.6 Summary

Throughout our project, we identified some parameters that are important to how particles interact with defects:

- Particle size regime

- Liquid crystal choice (particularly the elastic constants)

- Device thickness (especially when it is close to particle diameter)

- Particle geometry

We recommended some experiments to continue the work summarised in this thesis, on the theme of particles confined at defects in liquid crystals. We suggested performing similar experiments to chapter 6, but expanding to other liquid crystals with unusual elastic constants. We summarised some methods of creating defects in liquid crystals in a more controlled manner than in a Schlieren cell. Finally, we suggested some other particle types that may be interesting to investigate.

What about our original aim, building a new type of electronic paper, based on a Janus particle-based electrophoretic device? Nothing in the research in this project would rule out such a possibility, though some potential difficulties have been identified, such as particles becoming attached to substrates. We hope that others will continue the research in this project, and help to work towards this goal, and further the understanding of particles in liquid crystals.

References

1. J. Heikenfeld, P. Drzaic, J.-S. Yeo, and T. Koch, Journal of the Society for Information Display **19**, 129 (2011).

2. P. F. Bai, R. A. Hayes, M. L. Jin, L. L. Shui, Z. Chuan Yi, L. Wang, X. Zhang, and G. F. Zhou, Progress in Electromagnetics Research **147**, 95 (2014).

3. S. Klein, Liquid Crystals Reviews **1**, 52 (2013).

4. R. Eidenschink and W. H. De Jeu, Electronics Letters **27**, 1195 (1991).

5. M. Kreuzer, T. Tschudi, and R. Eidenschink, Molecular Crystals and Liquid Crystals **223**, 219 (1992).

6. S. Lee and C. Park, Molecular Crystals and Liquid Crystals **333**, 123 (1999).

7. D. Sikharulidze, Applied Physics Letters **86**, 1 (2005).

8. M. Ogawa, T. Takahashi, S. Saito, Y. Toko, Y. Iwakura, K. Kobayashi, and T. Akahane, SID Symposium Digest of Technical Papers **34**, 584 (2003).

9. N. K. Sheridon, E. A. Richley, J. C. Mikkelsen, D. Tsuda, J. M. Crowley, K. A. Oraham, M. E. Howard, M. A. Rodin, R. Swidler, and R. Sprague, Journal of the SID **7**, 141 (1999).

10. J. M. Crowley, Patent US 5754332 A (1998).

11. D. Pires, J. B. Fleury, and Y. Galerne, Physical Review Letters **98**, 247801 (2007).

12. A. V. Ryzhkova and I. Muševič, Physical Review E **87**, 032501 (2013).

13. J. L. Sanders, Y. Yang, M. R. Dickinson, and H. F. Gleeson, Philosophical Transactions of the Royal Society A **371**, 20120265 (2013).

14. M. Conradi, M. Ravnik, M. Bele, M. Zorko, S. Žumer, and I. Muševič, Soft Matter **5**, 3905 (2009).

15. M. Conradi, M. Zorko, and I. Muševič, Optics Express **18**, 500 (2010).

16. C. Chiccoli, P. Pasini, L. R. Evangelista, R. T. Teixeira-Souza, and C. Zannoni, Physical Review E **91**, 1 (2015).

17. R. J. Miller, Structural Studies of Chiral Frustrated Liquid Crystals, University of Manchester, 1994.

18. G. A. Oweimreen, Journal of Physical Chemistry B **105**, 8417 (2001).

19. P. J. R. Birtwistle, Dynamic Light Scattering from Liquid Crystalline Systems, University of Manchester, 1995.

20. A. G. Chmielewski, Molecular Crystals and Liquid Crystals **132**, 339 (1986).

21. H. Kneppe, F. Schneider, and N. K. Sharma, Berichte Der Bunsengesellschaft Für Physikalische Chemie **789**, 784 (1981).

22. N. V. Madhusudana and R. Pratibha, Molecular Crystals and Liquid Crystals **89**, 249 (2016).

23. S. Kaur, H. Liu, J. Addis, C. Greco, A. Ferrarini, V. Görtz, J. W. Goodby, and H. F. Gleeson, Journal of Materials Chemistry C **1**, 6667 (2013).

24. M. Hird, Liquid Crystals Today **14**, 9 (2005).

25. H. Takezoe and Y. Takanishi, Japanese Journal of Applied Physics, Part 1: Regular Papers and Short Notes and Review Papers **45**, 597 (2006).

26. P. S. Salter, C. Tschierske, S. J. Elston, and E. P. Raynes, Phys. Rev. E **84**, 31708 (2011).

27. R. Balachandran, V. P. Panov, J. K. Vij, A. Lehmann, and C. Tschierske, Phys. Rev. E **88**, 32503 (2013).

28. M. Majumdar, P. Salamon, A. Jákli, J. T. Gleeson, and S. Sprunt, Phys. Rev. E **83**, 31701 (2011).

29. P. Sathyanarayana, M. Mathew, Q. Li, V. S. S. Sastry, B. Kundu, K. V Le, H. Takezoe, and S. Dhara, Phys. Rev. E **81**, 10702 (2010).

30. K. Szendrei, P. Ganter, O. Sànchez-Sobrado, R. Eger, A. Kuhn, and B. V. Lotsch, Advanced Materials n/a (2015).

31. P. Tadapatri, U. S. Hiremath, C. V Yelamaggad, and K. S. Krishnamurthy, The Journal of Physical Chemistry B **114**, 1745 (2010).

32. S. Srigengan, M. Nagaraj, A. Ferrarini, R. Mandle, S. J. Cowling, M. A. Osipov, G. Pajak, J. W. Goodby, and H. F. Gleeson, Journal of Materials Chemistry C **6**, 980 (2018).

33. M. Nagaraj, Liquid Crystals **43**, 2244 (2016).

34. S. Kaur, J. Addis, C. Greco, A. Ferrarini, V. Görtz, J. W. Goodby, and H. F. Gleeson, Physical Review E - Statistical, Nonlinear, and Soft Matter Physics **86**, 1 (2012).

35. J. Lydon, Current Opinion in Colloid and Interface Science **8**, 480 (2004).

36. N. V. Madhusudana and R. Pratibha, Molecular Crystals and Liquid Crystals **89**, 249 (1982).

37. A. M. Figueiredo Neto and S. R. A. Salinas, *The Physics of Lyotropic Liquid Crystals* (Oxford University Press, 2005).

38. H. Kelker, *History of Liquid Crystals* (1973).

39. R. Virchow, Virchows Archiv **6**, 571 (1854).

40. P. Planer, Justus Liebigs Ann. Chem. **118**, 25 (1861).

41. E. Loebisch, Berichte Der Deutschen Chemischen Gesellschaft **5**, (1872).

42. J. Fang and R. L. Venable, Journal of Colloid And Interface Science **117**, 448 (1987).

43. G. Duplâtre, M. F. Ferreira Marques, and M. da Graça Miguel, The Journal of Physical Chemistry **100**, 16608 (1996).

44. G. N. Waite and L. R. Waite, *Applied Cell and Molecular Biology for Engineers* (McGraw Hill, 2007).

45. D. Anselmetti, editor , *Single Cell Analysis: Technologies and Applications* (Wiley, 2009).

46. Z. Zhang, Research into Order Parameters and Graphene Dispersions in Liquid Crystal Systems Using Raman Spectroscopy, University of Manchester, 2015.

47. T. Coultate, *Food: The Chemistry of Its Components*, 5th ed. (RSC Publishing, 2009).

48. S. C. Smolinske, *CRC Handbook of Food, Drug, and Cosmetic Excipients* (CRC Press, 1991).

49. H. S. Park, S. W. Kang, L. Tortora, Y. Nastishin, D. Finotello, S. Kumar, and O. D. Lavrentovieh, Journal of Physical Chemistry B **112**, 16307 (2008).

50. A. Yamaguchi, G. P. Smith, Y. Yi, C. Xu, S. Biffi, F. Serra, T. Bellini, C. Zhu, and N. A. Clark, Physical Review E **93**, 1 (2016).

51. A. Masters, Liquid Crystals Today **25**, 30 (2016).

52. V. G. Nazarenko, O. P. Boiko, H.-S. Park, O. M. Brodyn, M. M. Omelchenko, L. Tortora, Y. A. Nastishin, and O. D. Lavrentovich, Physical Review Letters **105**, 17801 (2010).

53. C. K. McGinn, L. I. Laderman, N. Zimmermann, H.-S. Kitzerow, and P. J. Collings, Phys. Rev. E **88**, 62513 (2013).

54. N. Zimmermann, G. Jünnemann-Held, P. J. Collings, and H.-S. Kitzerow, Soft Matter **11**, 1547 (2015).

55. A. Martinez, P. J. Collings, and A. G. Yodh, Physical Review Letters **121**, 177801 (2018).

56. S. Zhou, Y. A. Nastishin, M. M. Omelchenko, L. Tortora, V. G. Nazarenko, O. P. Boiko, and T. Ostapenko, Physical Review Letters **109**, 037801 (2012).

57. S. Kaur, Y. Kim, H. Milton, D. Mistry, I. M. Syed, J. Bailey, J. C. Jones, P. B. Morgan, J. Clamp, and H. F. Gleeson, Optics Express **24**, 8782 (2016).

58. X. Li, J. C. Armas-Pérez, J. P. Hernández-Ortiz, C. G. Arges, X. Liu, J. A. Martínez-González, L. E. Ocola, C. Bishop, H. Xie, J. J. De Pablo, and P. F. Nealey, ACS Nano **11**, 6492 (2017).

59. O. Yaroshchuk and Y. Reznikov, Journal of Materials Chemistry **22**, 286 (2012).

60. Y. Guo, M. Jiang, C. Peng, K. Sun, O. Yaroshchuk, O. D. Lavrentovich, and Q.-H. Wei, in (2016).

61. Y. Guo, M. Jiang, C. Peng, K. Sun, O. V Yaroshchuk, O. D. Lavrentovich, and Q.-H. Wei, Advanced Materials **28 12**, 2353 (2016).

62. I. Muševič, M. Škarabot, U. Tkalec, M. Ravnik, and S. Žumer, Science **313**, 954 (2006).

63. C. Peng, T. Turiv, Y. Guo, S. V Shiyanovskii, Q.-H. Wei, and O. D. Lavrentovich, Science Advances **2**, (2016).

64. D. Kasyanyuk, P. Pagliusi, A. Mazzulla, V. Reshetnyak, Y. Reznikov, C. Provenzano, M. Giocondo, M. Vasnetsov, O. Yaroshchuk, and G. Cipparrone, Scientific Reports **6**, 20742 (2016).

65. M. C. Jr, M. A. Gharbi, D. A. Beller, S. Čopar, Z. Shi, T. Baumgart, S. Yang, R. D. Kamien, and K. J. Stebe, Proceedings of the National Academy of Sciences **110**, 18804 (2013).

66. F. R. Hung, B. T. Gettelfinger, G. M. Koenig, N. L. Abbott, and J. J. De Pablo, Journal of Chemical Physics **127**, (2007).

67. Z. Eskandari, N. M. Silvestre, M. M. Telo Da Gama, and M. R. Ejtehadi, Soft Matter 1166 (2014).

68. A. V. Ryzhkova, M. Škarabot, and I. Muševič, Physical Review E **91**, 0(2015).

69. B. Huang, M. Bates, and X. Zhuang, Annual Review of Biochemistry **78**, 993 (2010).

70. B. O. Leung and K. C. Chou, Applied Spectroscopy **65**, 967 (2011).

71. J. Vangindertael, R. Camacho, W. Sempels, H. Mizuno, P. Dedecker, and K. P. F. Janssen, Methods Appl. Fluoresc **6**, 22003 (2018).

72. M. J. Rust, M. Bates, and X. Zhuang, Nature Methods **3**, 793 (2006).

73. M. G. L. Gustafsson, Journal of Microscopy **198**, 82 (2000).

74. R. E. Thompson, D. R. Larson, and W. W. Webb, Biophysical Journal **82**, 2775 (2002).

75. J. C. Jones, Journal of the Society for Information Display **16**, 143 (2008).

76. X. Wang, D. S. Miller, E. Bukusoglu, J. J. De Pablo, and N. L. Abbott, Nature Materials **15**, 1 (2015).

77. M. T. Raimondi, S. M. Eaton, M. M. Nava, M. Laganà, G. Cerullo, and R. Osellame, Journal of Applied Biomaterials & Functional Materials **10**, 56 (2012).

78. L. Li and J. T. Fourkas, Materials Today **10**, 30 (2007).

79. C. A. Serra and Z. Chang, Chemical Engineering and Technology **31**, 1099 (2008).

80. S. Xu, Z. Nie, M. Seo, P. Lewis, E. Kumacheva, H. A. Stone, P. Garstecki, D. B. Weibel, I. Gitlin, and G. M. Whitesides, Angewandte Chemie - International Edition **44**, 724 (2005).

81. S. E. Chung, W. Park, H. Park, K. Yu, N. Park, and S. Kwon, Applied Physics Letters **91**, 23 (2007).

82. B. I. Senyuk, Q. Liu, S. He, R. D. Kamien, R. B. Kusner, T. C. Lubensky, and I. I. Smalyukh, Nature **493**, 200 (2013).

83. B. I. Senyuk, M. B. Pandey, Q. Liu, M. Tasinkevych, and I. I. Smalyukh, Soft Matter 34 (2015).

84. Martinez, T. Lee, T. Asavei, H. Rubinsztein-Dunlop, and I. I. Smalyukh, Soft Matter **8**, 2432 (2012).

85. M. Cavallaro Jr, M. A. Gharbi, D. A. Beller, S. Čopar, Z. Shi, R. D. Kamien, S. Yang, T. Baumgart, and K. J. Stebe, Soft Matter **9**, 9099 (2013).

86. S. H. Kim, S. J. Jeon, W. C. Jeong, H. S. Park, and S. M. Yang,

Advanced Materials **20**, 4129 (2008).

87. S. H. Kim, S. Y. Lee, S. M. Yang, and G. R. Yi, NPG Asia Materials **3**, 25 (2011).

88. Z. Xu, L. Wang, F. Fang, Y. Fu, and Z. Yin, Current Nanoscience **12**, 725 (2016).